Low-dose IL-2 reduces IL-21^{+} T cells and induces a long-lived anti-inflammatory gene expression signature inversely modulated in COVID-19 patients

Jia-Yuan Zhang[1], Fiona Hamey[1], Dominik Trzupek[1], Marius Mickunas[2], Mercede Lee[1], Leila Godfrey[1], Jennie H.M. Yang[2], Marcin L Pekalski[1], Jane Kennet[3,4], Frank Waldron-Lynch[5], Mark L. Evans[3,4], Timothy I. M. Tree[2], Linda S. Wicker[1†], John A. Todd[1†] and Ricardo C. Ferreira[1†]

[1]JDRF/Wellcome Diabetes and Inflammation Laboratory, Wellcome Centre for Human Genetics, Nuffield Department of Medicine, NIHR Oxford Biomedical Research Centre, University of Oxford, Oxford, United Kingdom.

[2]Department of Immunobiology, King's College London, School of Immunology and Microbial Sciences, London, United Kingdom.

[3]Wellcome-MRC Institute of Metabolic Science, Metabolic Research Laboratories, University of Cambridge, Cambridge, United Kingdom.

[4]National Institute for Health Research Cambridge Biomedical Research Centre, Addenbrooke's Biomedical Campus, Cambridge, United Kingdom.

[5]Vertex Pharmaceuticals, Vertex Cell & Gene Therapies, Boston, Massachusetts, United States of America.

[†]Co-senior authors

Correspondence:

Prof. John A. Todd:

Email: john.todd@well.ox.ac.uk

Dr. Ricardo C. Ferreira:

Email: ricardo.ferreira@well.ox.ac.uk

Abstract

Despite early clinical successes, the mechanisms of action of low-dose interleukin-2 (LD-IL-2) immunotherapy remain only partly understood. Here, we examined the effects of interval administration of low-dose recombinant IL-2 (iLD-IL-2) using high-resolution, single-cell multiomics and flow cytometry. We confirmed that iLD-IL-2 selectively expands thymic-derived $FOXP3^{+}HELIOS^{+}$ Tregs and $CD56^{br}$ NK cells, and showed that treatment reduced the frequency of IL-21-producing $CD4^{+}$ T cells and of two subsets of innate-like $CD8^{+}$ T cells, mucosal-associated invariant T cells and $V_{\gamma9}V_{\delta2}$ T cells. The cellular changes induced by LD-IL-2 were associated with an anti-inflammatory gene expression signature, which remains detectable in all T and NK cell subsets analysed one month after treatment. The anti-inflammatory nature of this gene expression signature was supported by the observation that the same genes were also modulated in COVID-19 patients, but in the opposite direction. These findings warrant continued investigations of the potential clinical benefits of iLD-IL-2 in immunotherapy and further understanding of the development of long-term sequelae in convalescent COVID-19 patients.

Introduction

The use of much lower doses of interleukin-2 (IL-2) than employed in cancer therapy has shown clinical efficacy in a number of inflammatory and autoimmune conditions, by stimulating a subset of $CD4^+$ T cells expressing high levels of the high-affinity trimeric IL-2 receptor, designated as regulatory T cells (Tregs)[1–9]. In the autoimmune disease type 1 diabetes (T1D), the genetic association with the IL-2 pathway in mice[10] and in humans[11,12], combined with preclinical studies[13,14], have provided a strong rationale for the development of low-dose (LD)-IL-2 immunotherapy. Safety and dose determination studies in T1D have been informative and underpin future clinical trials in T1D[15–18]. We have previously conducted an adaptive single-dose observational study (DILT1D), which demonstrated the sensitivity and specificity of IL-2 signalling *in vivo* and determined a dosing range of $0.2\text{-}0.47\times10^6$ IU/m^2 of recombinant IL-2 (aldesleukin/proleukin) to achieve Treg increases in blood in the order of 20-50% from baseline[18]. We then performed a second study (DILfrequency)[19] to determine how often to give low-dose aldesleukin to reliably induce a steady-state Treg induction whilst maintaining the selective expansion of Tregs and not effector T cells.

Here, we explored in depth the effects and pharmacodynamics of interval LD-IL-2 dosing (iLD-IL-2) in DILfrequency peripheral blood mononuclear cell (PBMC) samples. We employed a recently developed targeted multiomics approach, which allowed us to simultaneously quantify 565 mRNA transcripts and 65 surface protein targets at the single-cell level[20]. We performed a detailed immunophenotypic characterization of both T and NK cell compartments, with a particular emphasis on the $CD4^+$ $CD127^{low}CD25^{hi}$ T cell and $CD56^{br}$ NK cell subsets, which have been previously shown to be highly sensitive to iLD-IL-2 treatment[18,19]. Aside from the expected expansions of thymic-derived $FOXP3^+HELIOS^+$ Tregs and $CD56^{br}$ NK cells in T1D patients, we show that iLD-IL-2 reduces the frequency of IL-21-producing cells, a subset that has been previously implicated in the pathogenesis of T1D[21–23]. The reduction of IL-21-producing cells by iLD-IL-2 may provide therapeutic benefit in T1D since a recent clinical trial combining anti-IL-21 with liraglutide (to improve beta cell function) slowed the decline of C-peptide[24]. Unexpectedly, we discovered that iLD-IL-2 also induces an anti-inflammatory gene expression signature in both

74 T and NK cell subsets that continues to at least one month after cessation of treatment. Altered
75 expression of the same set of genes, but in the opposite direction, was found to be progressively
76 induced and sustained in COVID-19 patients, highlighting the anti-inflammatory nature of the
77 prolonged iLD-IL-2-induced gene changes. Taken together, our findings indicate that iLD-IL-2
78 can reduce IL-21 during treatment, and induce a suite of cellular alterations that promotes the
79 establishment of a long-lived anti-inflammatory environment.

80

81 # Results

82 **Interval administration of low-dose IL-2 (iLD-IL-2) induces and maintains increased**
83 **frequencies of $CD4^+$ $CD127^{low}CD25^{hi}$ T cells and $CD56^{br}$ NK cells**

84 The DILfrequency[19] study established an optimal three-day aldesleukin dosing interval, with doses
85 ranging from 0.20-0.47 × 10^6 IU/m^2 (**Fig. 1a**). To gain further insight into the mechanism of action
86 of iLD-IL-2, we selected 18 DILfrequency participants (adults with long-standing T1D) treated
87 with this dosing regimen (**Supplementary Table 1**) and characterised the cellular alterations in
88 blood by polychromatic flow-cytometry (FACS). We observed a sustained increase in the
89 frequency of $CD4^+$ $CD127^{low}CD25^{hi}$ T cells (henceforth designated as the $CD4^+$ Treg gate) during
90 the dosing phase, but no alterations in the frequency of the broader $CD4^+$ conventional T (Tconv)
91 or $CD8^+$ T cell populations (**Fig. 1b,c**), including in a subset of $CD45RA^-CD62L^-$ effector memory
92 $CD4^+$ T cells (T_{EM}), known to be enriched for recently activated effector T cells (**Supplementary**
93 **Fig. 1a-c**).

94 Outside the T cell compartment, iLD-IL-2 also caused sustained increased frequencies of a subset
95 of $CD56^{br}$ NK cells (**Fig. 1c**). This effect was more pronounced than the increase in $CD4^+$ Tregs
96 and is consistent with the relatively high affinity of the $CD56^{br}$ NK subset for IL-2, especially
97 when compared to the bulk NK population[25,26]. We observed no alteration in the frequency of the
98 classical $CD56^{dim}$ NK cells, which represent the majority of $CD56^+$ NK cells in circulation. The
99 IL-2-induced increase in $CD4^+$ Tregs and $CD56^{br}$ NK cells was recapitulated when assessing
100 absolute numbers of cells in circulation, although their relative low abundance in blood resulted in
101 no discernible alteration in the numbers of either $CD4^+$ and $CD8^+$ T cells or $CD56^+$ NK cells (**Fig.**
102 **1d,e**). An increase in both frequency and numbers of $CD56^{br}$ (but not $CD56^{dim}$) NK cells in blood
103 was observed in all IL-2 dose groups (**Supplementary Fig. 1d-f**).

104

105 **Investigating IL-2-induced cellular alterations in blood using single-cell multiomics**

106 We next profiled PBMCs from 13 selected participants treated with the three-day interval dosing
107 regimen (**Supplementary Table 1**) using a targeted single-cell multiomics approach, which

108 enables the parallel quantification of specific mRNA and cell-surface proteins (AbSeq) in each
109 cell[27]. To increase the power of this approach to identify small, yet potentially important, changes
110 elicited by iLD-IL-2, we have adopted a cell enrichment strategy to greatly increase the numbers
111 of $CD4^+$ Tregs and $CD56^{br}$ NK cells profiled in this study. In addition, we designed a custom
112 mRNA panel of 565 oligonucleotide probes, assessed in parallel with the expression of 65 cell-
113 surface protein targets (**Supplementary Table 2**)[20]. From each participant, we selected three
114 longitudinal blood samples on Day 0 (baseline), Day 27 (immediately before the last IL-2
115 injection) and Day 55 (four weeks after the last IL-2 dose), respectively. We then isolated five
116 immune populations from each sample following predefined proportions: 30% $CD4^+$ Tregs; 25%
117 $CD4^+$ Tconv and $CD8^+$ T cells 12% $CD56^{br}$ and 8% $CD56^{dim}$ NK cells, which were analysed with
118 or without *in vitro* stimulation (**Fig. 1f**). Unsupervised clustering of the 482,531 unstimulated cells
119 passing quality control (QC) revealed a clear delineation of the sorted T and NK cell populations,
120 identifying 15 distinct functional clusters (**Fig. 1g**). We observed good overlap among cells from
121 each participant, with similar representation in the five sorted immune populations
122 (**Supplementary Fig. 2a-c**). A similar result was observed for the clustering of the 323,839
123 stimulated cells passing QC (**Supplementary Fig. 2d-f**), indicating minimal batch effects that are
124 usually prevalent in scRNA-seq data.

125 In the unstimulated cells, we also identified two clusters characterised by the distinct co-expression
126 of a set of canonical cell cycle genes (see Methods), including *MKI67* (encoding for Ki-67), which
127 corresponded to cycling T and NK cells (**Supplementary Fig. 3a**). Overall, we found no evidence
128 that iLD-IL-2 was increasing the frequency of proliferating cells. Conversely, we found a reduction
129 in the frequency of proliferating $CD56^{br}$ NK cells and $CD4^+$ Tregs at Day 27 (**Supplementary**
130 **Fig. 3b**). Given the previously reported increased frequency of Ki-67^+ Tregs and $CD56^{br}$ NK cells
131 following LD-IL-2 treatment, we next investigated the frequency of proliferating cells by assessing
132 the intracellular expression of Ki-67 in patients treated with either single or multiple doses of LD-
133 IL2. In agreement with previous observations[4,28,29], we found a marked increased frequency of Ki-
134 67^+ cells in both $CD4^+$ Tregs and $CD56^{br}$ NK cells following the first dose of IL-2
135 (**Supplementary Fig. 3c,d**). In the multiple dosing cohort, we noted that this increased frequency
136 of Ki-67^+ cells persisted up to Day 27 only in $CD56^{br}$ NK, but not in the $CD4^+$ Treg cells
137 (**Supplementary Fig. 3d**). This discrepancy between the multiomics and FACS assessment of
138 proliferating $CD56^{br}$ NK cells may reflect a difference in the use of protein or mRNA markers to

139 assess cell cycle progression. Both *MKI67* (mRNA) and Ki-67 protein are synthesised and
140 accumulate during the S and G2/M phases of the cell cycle and show very good correlation in
141 synchronised cells[30]. However, in contrast to *MKI67*, Ki-67 protein is more long-lived, and can
142 still be detected in G1 after cell division[31]. The levels of Ki-67 protein in G1 depend on the rate of
143 protein accumulation during the S and G2/M phases, leading to the much higher rate of detection
144 of Ki-67^{+} cells compared to the frequency of cells in the S-G/M phase (eg. 37% vs 1% in Fraction
145 II Tregs)[32]. Consistently, we found that 20% of total CD4^{+} Tregs are Ki-67^{+} at baseline, but only
146 ~1% were identified as proliferating by multiomics analysis. These data indicate that in contrast
147 to Ki-67^{+} protein levels, mRNA quantification allows a more specific identification of actively
148 dividing cells (in the S-G/M phases). Therefore, an explanation for the discrepancy between the
149 FACS and multiomics assessment of proliferating CD56^{br} NK cells at Day 27, is that the increased
150 levels of Ki-67^{+} cells reflect protein accumulation in recently divided G1 cells. In contrast, the
151 decrease in proliferating cells from the multiomics analysis reflects a reduction of actively dividing
152 cells in blood, possibly due to an increased likelihood for cells to enter the cell cycle in tissues as
153 IL-2 accumulates on the extracellular matrix during dosing[33–36].

154 **Interval administration of low-dose IL-2 selectively expands FOXP3^{+}HELIOS^{+} Tregs**

155 Next, we sought to investigate whether our iLD-IL-2 regimen altered the relative composition of
156 the cells sorted from the CD127^{low}CD25^{hi} Treg gate (**Supplementary Fig. 4**). Analysis of the
157 expression of the canonical Treg transcription factors *FOXP3* and *IKZF2* (encoding HELIOS)
158 allowed the stratification of CD127^{low}CD25^{hi} Treg clusters into three functional groups according
159 to their origin (**Supplementary Fig. 5** and **Methods**). Differential abundance analysis revealed an
160 enrichment in the frequency of naïve FOXP3^{+}HELIOS^{+} Tregs and a concomitant reduction of
161 CD25^{+} FOXP3$^{–}$HELIOS$^{–}$ Teffs on Day 27, after the conclusion of the four-week IL-2 dosing
162 phase, immediately before the last of the ten aldesleukin injections (**Fig. 2a,b**), which was
163 replicated in stimulated cells (**Fig. 2c,d**). Given the observed increase in CD127^{low}CD25^{hi} T cells
164 by FACS following LD-IL-2, we next investigated whether these changes were also reflected in
165 the absolute numbers in circulation, which were inferred from the relative frequencies identified
166 by single-cell analysis, scaled by the whole-blood CD127^{low}CD25^{hi} Treg counts. We found that
167 the IL-2 induced expansion on Day 27 was restricted to the thymic-derived FOXP3^{+}HELIOS^{+}
168 Treg subsets (**Fig. 2e**). We observed very good concordance between unstimulated and stimulated

169 conditions, with naïve Tregs showing >2-fold increase and memory FOXP3^{+}HELIOS^{+} Tregs
170 displaying approximately a 70% increase in cell numbers compared to baseline pre-treatment
171 levels (**Fig. 2e**). In contrast, despite the expansion of CD127^{low}CD25^{hi} T cells, we obtained no
172 evidence of alterations in the number of activated CD25^{+} FOXP3^{-}HELIOS^{-} Teffs contained in this
173 population, even though they express the high affinity trimeric IL-2 receptor (**Fig. 2e**).
174 Furthermore, we observed no changes in the *in vitro* suppressive capacity of CD4^{+}
175 CD127^{low}CD25^{hi} T cells after IL-2 treatment on a per cell basis compared to the pre-treatment cells
176 (**Fig. 2f**). The alterations in the relative composition of CD127^{low}CD25^{hi} T cells were found to be
177 transient and reverted to baseline one month after the last dose of IL-2 (Day 55; **Supplementary**
178 **Fig. 6a-d**). In contrast, we observed no notable changes in the relative abundance of CD4^{+}CD25^{-}
179 $^{/low}$ Tconv subsets during or after IL-2 treatment (**Supplementary Fig. 7**).

180 Using pseudo-time analysis, we identified a single trajectory of FOXP3^{+} Treg differentiation
181 among CD4^{+} T cells, stemming from the conventional naïve Tregs towards the classical HLA-II^{+}
182 effector Treg subset (**Supplementary Fig. 8a-c**). In agreement with our compositional analysis,
183 we found a significantly increased ratio of naïve to HLA-II^{+} Tregs at Day 27 (**Supplementary**
184 **Fig. 8d**). Notably, there was no alteration in the differentiation status of Tregs in response to iLD-
185 IL-2, as illustrated by the overlapping pseudo-time distribution within the Treg differentiation
186 trajectory between Days 0, 27 and 55 (**Supplementary Fig. 8d**). These data indicate that iLD-IL-
187 2 treatment is affecting only the output and/or survival of thymic-derived naïve Tregs but not their
188 differentiation towards HLA-II^{+} effector Tregs. Furthermore, we also replicated the transient IL-
189 2-induced increase in the frequency of naïve Tregs by measuring the naïve:memory Treg ratio at
190 Day 27 by FACS in all 18 DILfrequency participants treated with the 3-day interval dosing
191 schedule (**Supplementary Fig. 9a-c**). We found good concordance between FACS and single-cell
192 data on the frequency of naïve and memory Tregs as well as their ratios (**Supplementary Fig.**
193 **9d,e**). To confirm the characterisation of Treg subsets obtained through the single-cell multiomics
194 analysis, we next assessed the protein expression of FOXP3 and HELIOS by FACS in our single
195 and multiple dosing replication cohorts. In agreement with the multiomics analysis, we found a
196 selective decrease in the relative proportion of CD45RA^{-} FOXP3^{-}HELIOS^{-} cells within
197 CD127^{low}CD25^{hi} T cells in both cohorts in response to iLD-IL-2 (**Supplementary Fig. 10a-c**).
198 These results translated into a consistent increase in the frequency of both CD4^{+}CD25^{hi} FOXP3^{+}

199 Treg subsets and a concomitant reduction in $CD4^{+}CD25^{hi}$ $FOXP3^{-}HELIOS^{-}$ Teffs
200 (**Supplementary Fig. 10d,e**).

201 In addition to the conventional $CD25^{hi}$ $FOXP3^{+}$ Treg subsets, we have recently shown that a subset
202 of $CD25^{-/low}$ $FOXP3^{+}$ T cells are increased in patients with autoimmune diseases[37]. We found no
203 substantial change in the frequency of $CD25^{-/low}$ $FOXP3^{+}$ T cells (defined as cells with >=1 copy
204 of FOXP3 within the $CD4^{+}CD25^{-/low}$ Tconv gate; **Supplementary Fig. 11a,b**). We replicated
205 these results using a FACS approach to vastly increase the number of characterised $CD25^{-/low}$
206 $FOXP3^{+}$ T cells. In agreement with the multiomics analysis we found no change in the frequency
207 of this rare subset in either the single or multiple dosing cohorts (**Supplementary Fig.11c-g**).
208 However, we noted a small reduction in the frequency of $CD25^{-/low}$ $FOXP3^{+}$ T cells at Day 27 by
209 both methods, suggesting that iLD-IL-2 may restore the CD25 expression in these cells.

210

211 **IL-21-producing T cells are reduced by iLD-IL-2 treatment**

212 Among the identified $CD25^{+}$ $FOXP3^{-}HELIOS^{-}$ Teff clusters within the sorted $CD127^{low}CD25^{hi}$
213 Treg cells, we noted an IL-2-induced reduction of a subset with a marked T follicular helper (T_{FH})
214 cell profile, including the expression of canonical T_{FH} receptors CXCR5, PD-1 and ICOS, and the
215 transcription factor *MAF* ($CD25^{hi}$ T_{FH}, cluster 8; **Supplementary Figs. 4a** and **6a)**. Although
216 differentiated T_{FH} cells are rare in blood, within cells sorted from the $CD25^{-/low}$ Tconv gate, we
217 were able to characterise an analogous heterogeneous cluster of central memory (T_{CM}) $CXCR5^{+}$
218 cells (cluster 1; **Supplementary Fig. 7a-c**), which is known to be enriched with circulating
219 precursors of T_{FH} cells. Upon *in vitro* stimulation, which elicited the expression of the classical
220 T_{FH} cytokine IL-21, we obtained a better discrimination of the T_{FH} clusters. This led to improved
221 differentiation of a cluster of $CXCR5^{+}$ T_{CM} cells (cluster 2) and a cluster of $CXCR5^{low}$ IL-21^{+} T
222 cells (cluster 6) that was reduced with IL-2 dosing (**Supplementary Fig. 7d-f**). In addition, within
223 the $CD127^{low}CD25^{hi}$ Treg gate, *in vitro* stimulation allowed the stratification of the activated
224 $CD25^{+}$ T_{FH} cells into two separate clusters (cluster 10 and 11) based on their expression of IL-21
225 that were both reduced by iLD-IL-2 treatment (**Supplementary Fig. 6b**). We note that a related
226 cluster of $FOXP3^{+}$ T follicular regulatory cells (T_{FR}, cluster 11 in unstimulated cells) which, in
227 addition to the T_{FH} signature, also featured a distinct Treg transcriptional profile as well as the

228 upregulation of *POU2AF1* and *CCR9*, was not altered by iLD-IL-2 treatment (**Supplementary**
229 **Fig. 6a**).

230 Next, we compared the transcriptional profile of the four identified T_{FH}-like clusters marked by
231 the specific upregulation of IL-21 expression. We identified a continuum of T_{FH} cell differentiation
232 among these clusters, with the $CD25^{+}$IL-21^{+} T_{FH} subset representing the terminal stage of
233 maturation in blood, as illustrated by their classical T_{FH} profile and increased IL-21 production
234 (**Fig. 3a**). Analysis of the co-expression of CXCR5 and IL-21 revealed that IL-21 was
235 preferentially expressed within the $CXCR5^{+}$ cells (**Fig. 3b**). The exception was in the $CXCR5^{low}$
236 IL-21^{+} cluster, where approximately 50% of the IL-21^{+} cells were also $CXCR5^{low}$. These data
237 suggest that our single-cell multiomics approach allows us to specifically identify the more
238 differentiated IL-21-producing T cells in this cluster, with a phenotype resembling the $CXCR5^{low}$
239 PD-1^{hi} circulating T peripheral helper (T_{PH}) cells that have been previously shown to be increased
240 in T1D patients[23]. Furthermore, we found similar profiles between the $CXCR5^{+}$ T_{CM} and the
241 $CD25^{+}$ T_{FH} clusters sorted from the $CD25^{-/low}$ Tconv and $CD25^{+}$ Treg gates, respectively, with the
242 latter likely representing an earlier stage of T_{FH}-cell differentiation. In agreement with this shared
243 identity and developmental stage, the $CXCR5^{+}$ T_{CM} and $CD25^{+}$ T_{FH} subsets displayed largely
244 overlapping embeddings among all stimulated $CD4^{+}$ T cells (**Fig. 3c,d**). In contrast to these three
245 conventional T_{FH}-like subsets, which seem to share a similar differentiation pathway, the
246 $CXCR5^{low}$IL-21^{+} $CD25^{-/low}$ Teff cluster represented a much more heterogeneous cluster with a
247 scattered clustering profile and increased IL-21 production (**Fig. 3c,d**).

248 To better discriminate the effect of IL-2 on the differentiation of IL-21-producing cells, we then
249 stratified the cells in these four T clusters according to their expression of IL-21 to define activated
250 T_{FH} profiles (**Fig. 3e**). Consistent with the results from the differential abundance analysis
251 (**Supplementary Figs. 6b** and **7e**), we found evidence for a reduction in the relative proportion of
252 IL-21^{+} cells at Day 27 in the two subsets with higher frequencies of IL-21^{+} cells (**Fig. 3f**).
253 Furthermore, pseudo-time analysis in total stimulated $CD4^{+}$ T cells revealed a similar trajectory of
254 T_{FH} cell differentiation characterised by the acquisition of an activated T_{FH} phenotype and
255 production of IL-21 (**Supplementary Fig. 8e-g**). In contrast with the $FOXP3^{+}$ Treg trajectory,
256 iLD-IL-2 was found to impair this differentiation trajectory, as illustrated by the reduced pseudo-
257 time distribution at Day 27 among cells from the more differentiated $CD25^{+}$IL-21^{+} T_{FH} subset

258 (**Supplementary Fig. 8h**). These results further support a broader, previously uncharacterized,
259 effect of iLD-IL-2 immunotherapy in potentially inhibiting the differentiation of IL-21-producing
260 cells. In addition to the reduction of IL-21-producing cells, we also obtained some evidence (FDR-
261 adjusted $P = 0.096$) for the reduction of another subset marked by the expression of many pro-
262 inflammatory cytokines, including GM-CSF, IL-21 and IL-2, as well as the classical type-2
263 inflammatory cytokines IL-4 and IL-13 ($CD25^+$ T_{H2} T_{EM}, cluster 6; **Supplementary Figs. 4b** and
264 **6b**).

265 **Effects of iLD-IL-2 on $CD8^+$ T and $CD56^+$ NK cells**

266 In the $CD8^+$ T cell compartment, differential abundance analysis revealed no discernible
267 differences in the relative composition of the conventional αβ $CD8^+$ T cell subsets after IL-2
268 treatment. However, we identified a previously uncharacterised reduction of two subsets of innate-
269 like $CD8^+$ T cells, including mucosal-associated invariant T cells (MAIT; cluster 4) and $V_{\gamma9}V_{\delta2}$ T
270 cells (cluster 9; **Fig. 4a,b** and **Supplementary Fig. 12**). In contrast to the IL-2 induced alterations
271 in the $CD4^+$ T cell compartment, the reduction of circulating MAIT and $V_{\gamma9}V_{\delta2}$ T cells was more
272 long-lived and there was still evidence of a reduced frequency in blood one month after the last
273 dose of IL-2 (**Fig. 4c**).

274 Finally, in the $CD56^+$ NK cell compartment, despite the lower level of functional heterogeneity
275 and differentiation (**Fig. 4d,e**), we found that the increased frequency of $CD56^{br}$ NK cells after IL-
276 2 treatment, was driven particularly by an increased relative proportion of an activated HLA-II^+
277 subset (**Fig. 4f**). By contrast we found no alterations in the relative composition of $CD56^{dim}$ subsets
278 (**Fig. 4g** and **Supplementary Fig. 13**). Consistent with activation phenotype and increased
279 expression of CD56 on $CD56^{br}$ NK cells after treatment, we observed a reduced frequency of
280 contaminating $CD56^{dim}$ and $CD56^{br}$ NK cells sorted from the $CD56^{br}$ and $CD56^{dim}$ NK cell gates,
281 respectively at Day 27 (**Fig. 4f,g**). The alterations in the $CD56^{br}$ NK cells were also transient and
282 were not maintained one month after treatment (**Supplementary Fig. 13b,c**).

283 **Interval low-dose IL-2 immunotherapy induces a systemic and long-lasting anti-**
284 **inflammatory gene expression signature**

285 We next investigated whether, in addition to cellular composition alterations, we could detect IL-
286 2-induced gene expression changes. On Day 27, we identified 40 genes that are differentially
287 expressed in one or more subsets of unstimulated and stimulated cells (**Fig. 5a-c**). Consistent with
288 previous flow cytometry analyses[19], CD25 was strongly upregulated on Tregs on Day 27. The
289 differential expressed genes were mostly restricted to the more IL-2-sensitive $CD127^{low}CD25^{hi}$
290 Treg and $CD56^{br}$ NK cell subsets and could be broadly categorised into $CD4^{+}$ Treg and $CD56^{br}$
291 NK cell signature genes, reflecting the relative increased proportion of both subsets after iLD-IL-
292 2 treatment, as well as the identified reduction in actively dividing $CD56^{br}$ NK cells
293 (**Supplementary Fig. 3b**). Cycling cells were not present in the stimulated cell populations,
294 potentially due to the preferential sensitivity of cycling cells to apoptosis following activation.

295 Contrary to the differential expression on Day 27, which was observed exclusively in the IL-2-
296 sensitive Treg and $CD56^{br}$ subsets, differential expression on Day 55, one month after the last IL-
297 2 injection, was widespread and displayed a consistent pattern in all five assessed immune subsets
298 (**Fig. 6a** and **Supplementary Fig. 14a,b**). These findings indicate that our iLD-IL-2 dosing
299 regimen induces a shared Day 55 gene expression signature in different cell types, which featured
300 most prominently the upregulation of Cytokine Inducible SH2 Containing Protein (*CISH*), a gene
301 encoding a well-characterised negative regulator of cytokine signalling, and the downregulation
302 of Amphiregulin (*AREG*), a secreted TNF-inducible protein with pleiotropic roles in
303 inflammation[38]. We also noted an enrichment of genes associated with cytokine signalling, most
304 notably in the tumour necrosis factor (TNF) signalling pathway, which in addition to *CISH* and
305 *AREG*, also included *TNFSF14*, *TNFSF10*, *STAT1*, *SGK1*, *NFKBIZ*, *NFKBIA*, *DUSP2*, *DUSP4*,
306 *DUSP5*, *RGS1* and *TNFAIP3* (**Fig. 6a**). Furthermore, we observed a downregulation of several
307 TNF-induced genes that play a central role in curtailing TNF signalling, including the inhibitors
308 of NFκB, *NFKBIZ* and *NFKBIA*, *RGS1*, *TNFAIP3* and *AREG*. Consistent with this observation,
309 Oncostatin M (*OSM*), a pro-inflammatory cytokine shown to be increased in inflammatory bowel
310 disease patients with poor response to anti-TNF therapy[39], was also downregulated by iLD-IL-2.
311 Increased expression of *TNFSF14*, which encodes LIGHT, is notable since decreased expression
312 is associated with higher susceptibility to multiple sclerosis[40] and in a mouse model of multiple

313 sclerosis, LIGHT expression in the brain limits disease severity[41]. The widespread detection of this
314 signature in all five T and NK cell populations assessed in this study suggests that this effect is not
315 driven by IL-2 signalling directly but is likely the result of the sustained cellular changes induced
316 by iLD-IL-2 immunotherapy.

317 Although this Day 55 expression signature was detected in 11 of the 12 participants with Day 55
318 data, we observed heterogeneity among participants for the expression levels of the same genes on
319 Day 27 (**Fig. 6b**). Some participants exhibited concordant expression changes on Day 27 and Day
320 5, compared to Day 0, while others showed discordant expression profiles, with *CISH* being
321 downregulated and *AREG* upregulated on Day 27. Moreover, by principal component analysis
322 (PCA), we found that this concordant-discordant axis, captured by the first principal component
323 (PC1), was able to largely explain the inter-individual heterogeneity of Day 55 signature genes on
324 Day 27 and appeared to be associated with IL-2 dose (**Supplementary Fig. 14c**). Considering this,
325 we derived a linear score to quantify the changes in the Day 55 signature for each participant,
326 referred to as the Day 55 signature score, with higher scores reflecting higher expression of
327 signature genes upregulated on Day 55 (e.g. *CISH*), and lower expression of signature genes
328 downregulated on Day 55 (e.g. *AREG*). As expected, the Day 55 signature score showed
329 considerable inter-individual variation (**Fig. 6c**) that was consistent across different cell types
330 (**Supplementary Fig. 14d**). This enabled us to correlate changes in signature score, which
331 indicated the direction and amplitude of the modulation of Day 55 genes, with IL-2 dose level. We
332 confirmed that participants receiving higher doses of IL-2 were more likely to have increased
333 signature scores on Day 27 and Day 55 compared the baseline, indicating concordant expression
334 changes, whilst participants receiving lower doses tended to show discordant changes (**Fig. 6d,e**).
335 The dose-dependence of the Day 55 signature reached statistical significance only when
336 comparing to the participant-specific baseline, but not when inspecting the cross-sectional data at
337 each time point (**Supplementary Fig. 14e**). This underscores the importance of our longitudinal
338 study design that enhanced our statistical power to identify differential expression patterns.

339

340 **Long-lived iLD-IL-2 gene expression alteration is inversely modulated in COVID-19 patients**
341 **and is progressively induced after the onset of symptoms**

342 To extend the support for the existence of the Day 55 gene expression signature, we sought
343 independent evidence of a similar transcriptional response with another immune challenge.
344 Recently, the Oxford COVID-19 Multi-omics Blood Atlas (COMBAT) study[42] has generated a
345 large single-cell dataset illustrating the changes in blood induced by COVID-19 infection. We
346 found a reverse regulation in all immune populations of the 41 identified IL-2 regulated Day 55
347 signature genes, including a marked downregulation of *CISH* and upregulation of *AREG* in
348 COVID-19 patients (**Fig. 7A**). This finding was replicated in an independent cohort of
349 convalescent COVID-19 patients (INCOV)[43]. In both cohorts, we observed a progressive reduction
350 of the Day 55 gene expression signature, which was particularly pronounced for the first 2-3 weeks
351 after the onset of symptoms (**Fig. 7b,c**). In the INCOV cohort, follow-up samples taken several
352 months after initial symptoms revealed signs of a slow recovery towards the pre-COVID-19
353 baseline. (**Fig. 7c**). This progressive induction of the Day 55 signature genes was observed in all
354 COVID-19 disease severity groups and was consistent in all immune populations (**Supplementary**
355 **Fig. 15**).

356 In the COMBAT study[36], a multiparametric COVID-19-induced gene expression signature,
357 designated as Component 187, featured the differential expression of several Day 55 iLD-IL-2
358 signature genes, including *CISH* and *AREG*. Of the 1,419 genes contributing to the COVID-19
359 Component 187, 77 were present in our transcriptional panel. We found that virtually all signature
360 genes upregulated on Day 55 had negative loading scores in the COVID-19 Component 187, and
361 vice versa (**Fig. 7d**), indicating a strong inverse correlation between the differential gene
362 expression induced by IL-2 treatment and COVID-19. In the COMBAT study, Component 187
363 belonged to Cluster 3, a cluster of similar gene expression signatures associated with all severity
364 groups of COVID-19 patients. We found that Cluster 3 showed the strongest enrichment of the
365 Day 55 Signature genes, compared to all other reported clusters (**Fig. 7e**). Furthermore, the
366 dynamics of Component 187 over time were similar to that of the Day 55 Signature, though in the
367 opposite direction (**Fig. 7f**), implying that the set point of a homeostatic cellular network is altered
368 in opposing directions by LD-IL-2 immunotherapy and COVID-19.

369 **Discussion**

370 Our findings not only extend previous studies[15–17,28] but also provide new insight into the
371 mechanism of action of LD-IL-2 that has practical implications for its clinical use: firstly, we show
372 that LD-IL-2 administered every three days for a period of one month is able to selectively increase
373 the frequency and number of thymic-derived FOXP3^{+}HELIOS^{+} Tregs in all 18 study participants
374 analysed, while showing no detectable impact on the expansion or activation of conventional
375 effector T or CD56^{dim} NK cells. We observed a particularly pronounced increase in the frequency
376 of naïve FOXP3^{+}HELIOS^{+} Tregs after iLD-IL-2 therapy, indicating that the Treg increases are
377 caused by an increased representation of thymic-derived Tregs, and not the proliferation of
378 peripherally-induced Tregs. These findings are consistent with the increased clonal diversity in T
379 cells following an escalating LD-IL-2 regimen in graft-versus-host disease patients[44,45]. Secondly,
380 we also noted that our iLD-IL-2 schedule did not induce a detectable cytotoxic gene expression
381 signature in any T cell subset, indicating that among T cells iLD-IL-2 has a Treg-specific effect
382 and does not lead to the activation of a pro-inflammatory response. In addition to Tregs, the CD56^{br}
383 NK cell population is also probably contributing to the overall anti-inflammatory effects of iLD-
384 IL-2, in an immunoregulatory role, as previously described[46,47]. Thirdly, iLD-IL-2 was able to
385 reduce IL-21-producing T cells, possibly by antagonizing their differentiation. IL-2 signalling has
386 been shown to inhibit the differentiation of T_{FH} cells *in vivo* in mice[48], and in an *in vitro* model in
387 humans[49]. Consistent with these findings, LD-IL-2 has been shown to decrease the frequency of
388 T_{FH} cells, as defined by cell surface markers[50], as well as the frequency of marginal zone B cells[29]
389 in SLE patients, supporting a role in the regulation of germinal centre reactions. Our results extend
390 these findings to T1D and demonstrate a specific effect of iLD-IL-2 treatment in reducing
391 pathogenic IL-21-producing CXCR5^{+} T_{FH} cells as well as IL-21-producing CXCR5^{low} T cells.
392 Previously, we have shown that a two-fold increase in IL-2, but not IL-21, was responsible for the
393 protective effect conferred by the *Idd3* locus (containing *IL2* and *IL21*) in the nonobese diabetic
394 (NOD) mouse model of T1D[13], and independently that a reduction in IL-21 correlated with
395 increased IL-2[51]. In humans, IL-21 has been implicated in the pathogenesis of several autoimmune
396 diseases[52,53], particularly T1D[21–23]. Together, these observations lend further support for the use of
397 iLD-IL-2 in T1D as well as in other diseases associated with increased IL-21 production, such as
398 systemic lupus erythematosus, rheumatoid arthritis, and psoriasis. In support of this therapeutic

399 strategy, an anti-IL-21 monoclonal antibody in combination with liraglutide showed promising
400 results in preserving beta-cell function[24]. Of note, we observed no evidence for the alteration of
401 the frequency of FOXP3$^+$ T_{FR} cells, which has been previously shown to play a role in the
402 regulation of T_{FH} cells and the germinal centre reaction[54,55].

403 We also observed a decrease in circulating innate-like CD8$^+$ MAIT and $V_{\gamma9}V_{\delta2}$ T cell subsets
404 during treatment and one month after. Since these cells function in anti-viral and anti-bacterial
405 defence[56], our findings suggest a role of IL-2 immunotherapy in the recruitment of MAIT and
406 $V_{\gamma9}V_{\delta2}$ T cells to tissues following treatment, thereby increasing defence against viral and bacterial
407 infections[57]. This could provide a mechanism for the observed decreased incidence of viral
408 infections in SLE patients undergoing LD-IL-2 immunotherapy[58].

409 The cellular alterations induced by iLD-IL-2 treatment led to the establishment of a long-lived
410 gene expression signature in all assessed immune populations, which suggest a novel
411 immunoregulatory mechanism of iLD-IL-2. Although the effects of this signature are not yet
412 understood, it is marked by the distinct upregulation of *CISH*, a well-characterised negative
413 regulator of cytokine signalling whose expression is known to be induced by IL-2, as well as other
414 cytokines, signalling through the activation of STAT5[59]. In contrast, among the downregulated
415 genes, we observed several negative regulators of an inflammatory response at Day 55, including
416 key TNF-induced genes such as *TNFAIP3*, *RGS1* and *AREG*, suggesting that iLD-IL-2 can
417 decrease the homeostatic levels of TNF for at least one month after the cessation of dosing. Support
418 for the existence of the iLD-IL2-induced long-lived gene expression signature was obtained from
419 analysis of the Oxford COMBAT dataset[42], where we detected the modulation of the same genes,
420 but showing consistent opposite direction of expression following the onset of COVID-19
421 symptoms. We replicated this signature in a large longitudinal cohort of convalescent COVID-19
422 patients[43], which demonstrated a progressive induction of these genes that was particularly
423 pronounced in the first two weeks after onset of symptoms. This altered expression profile was
424 consistently sustained for up to 5 months, evidencing the longevity of this immune dysregulation
425 in COVID-19 patients. One possible explanation for the longevity of the signature is that TNF and
426 IL-2 are among the cytokines known to bind to the extracellular matrix[33–36] and that the retention
427 of the cytokines within tissues extends far beyond their initial increases[60]. The establishment of
428 the Day 55 IL-2 signature is dose-dependent at Day 27, likely reflecting a dose-dependent

429 accumulation of injected IL-2 on the extracellular matrix within the interstitial space following
430 subcutaneous dosing. A long-lasting immune alteration that also possibly reflects a continuing
431 inflammatory stimulus or long-lived pro-inflammatory cytokines on the extracellular matrix has
432 been reported in mild COVID-19 patients, with infection inducing a pro-inflammatory response in
433 monocyte-derived macrophages that continues to be detected 3-5 months following SARS-CoV-2
434 infection[61]. In a separate study, pro-inflammatory markers such as IL-8 and sTIM-3 were still
435 elevated four months after the cessation of COVID-19 symptoms in patients having had mild or
436 moderate disease, but the increases resolved eight months post-infection except in patients with
437 long COVID[62].

438 We hypothesise that the balance between pro- and anti-inflammatory cytokines bound to the
439 extracellular matrix provides a regulatory mechanism to control immune responses. Circulating
440 immune cells can constantly integrate this information through a combination of cell-type specific
441 receptors. Under homeostatic conditions this provides a dynamic buffer system preventing
442 excessive (or potentially chronic) immune activation. A perturbation of this balance via either
443 sustained regulatory (e.g. iLD-IL-2 immunotherapy) or inflammatory (e.g. SARS-CoV-2
444 infection) environment can alter the composition of the soluble mediators contained in the
445 extracellular matrix, and consequently affect the interaction between the immune system and the
446 local environment, leading to the remodelling of their transcriptional profile and an alteration of
447 their threshold for further stimulation. Such a complex system is likely critical not only to prolong
448 the biological activity of key immune mediators such as TNF and IL-2, but also to control site
449 specificity to prevent improper signalling in the wrong physiological context. These findings are
450 also consistent with our observation that pro-inflammatory gene expression is progressively
451 induced after infection, and that it could contribute to the long-lasting systemic alterations
452 associated with the persistence of clinical manifestations in long COVID patients.

453 A limitation of this study is that we were not able to elucidate the exact mechanism underpinning
454 the induction of the identified long-lived gene expression signature and how this is regulated by
455 iLD-IL-2 or COVID-19. Although we show that iLD-IL-2 can induce this signature, it is certainly
456 not the only responsible factor, as a reversed expression can also be induced in a completely
457 different pathophysiological context such as COVID-19. Furthermore, markers of disease activity
458 and progression are limited in T1D and were not collected for the DILfrequency patients, which

459 precludes the analysis of how they are associated with these gene expression alterations. A more
460 comprehensive investigation of these questions will need to be performed in an appropriate follow
461 up cohort such as the recently completed Interleukin-2 Therapy of Autoimmunity in Diabetes
462 (ITAD) trial[63]. The findings from this study will inform the design of suitable follow up
463 experiments in this and other studies of iLD-IL-2 in multiple diseases and will be critical to better
464 understand both the longevity of the signature and how it is associated with clinical outcomes.
465 Another limitation is that the interpretation of the results may be dependent on our specific iLD-
466 IL-2 dosing regimen. Although it is likely that most regimens will induce very similar results, it
467 will be important to validate these findings in different dosing schedules. Given the diverse range
468 of conditions where LD-IL-2 immunotherapy is being trialled, it is critical to better understand
469 how dosing regimen affects the drug's mechanism of action, and to tailor it to the disease-specific
470 applications, including when best to administer IL-2 during the course of standard care or as a way
471 of maintaining the clinical benefits of ongoing treatments[64], for example, in the use of anti-CD3
472 (teplizumab) to treat and prevent T1D[65].

473 Taken together, our findings provide a better understanding of the mechanism of action of LD-IL-
474 2 immunotherapy. In the past there have been concerns over the very short half-life of recombinant
475 IL-2 *in vivo* and that NK cell expansion might be detrimental, which have led to the development
476 of genetically-modified IL-2 muteins with increased half-life and preferential binding to the high-
477 affinity trimeric IL-2 receptor in order to reduce $CD56^{br}$ NK cell stimulation. Our results
478 demonstrating a long-lived gene expression signature associated with potential anti-inflammatory
479 effects, detectable one month after the end of aldesleukin treatment, alleviate some of these
480 concerns and support the therapeutic potential of IL-2 that is not engineered for longer *in vivo* half-
481 life or preferential binding to the high affinity IL-2 receptor, given intermittently and at low doses.
482 Our study adds to the good track record of using low-dose recombinant IL-2 and confirms its very
483 strong safety profile, which is critical for the potential long-term use of LD-IL-2 immunotherapy
484 for diseases such as T1D in which the target patient population will consist mainly of children,
485 including the possible future use of iLD-IL-2 treatment in the prevention of T1D diagnosis, as
486 demonstrated in recent teplizumab trials[65] and for T1D treatment with other monoclonal antibodies
487 such as golimumab (anti-TNF)[66,67]. Additionally, iLD-IL-2 treatment could be trialled in
488 recovering COVID-19 patients, after acute inflammation has been resolved, to determine if such

489 treatment hastens the restoration of normal immune homeostasis and perhaps reduce the
490 occurrence of long COVID complications.

491 # Methods

492 The study was performed in accordance with the guidelines for good clinical practice and the
493 Declaration of Helsinki. Study participants included T1D patients enrolled in two single centre
494 mechanistic studies of low-dose recombinant IL-2 (aldesleukin) immunotherapy: (i) the Adaptive
495 study of IL-2 dose on regulatory T cells in type 1 diabetes (DILT1D), a non-randomised single
496 IL-2 dosing study20; and (ii) the Adaptive study of IL-2 dose frequency on regulatory T cells in
497 type 1 diabetes (DILfrequency), a response-adaptive trial of repeated doses of IL-2 administered
498 using an interval dosing approach21. Approval was obtained from the Health Research
499 Authority, National Research Ethics Service (13/EE/0020 and 14/EE/1057, for the DILT1D and
500 DILfrequency studies, respectively), London, United Kingdom. The trials were registered at the
501 International Standard Randomised Controlled Trial Number Register (ISRCTN27852285 and
502 ISRCTN40319192) and ClinicalTrials.gov (NCT01827735 and NCT02265809). The study
503 protocols were published in advance of the completion and final analysis of the trials[68,69]. All
504 participants provided written informed consent prior to their participation in the studies.

505 **Study design and participants**

506 Study participants comprised 18 T1D patients enrolled in the DILfrequency study[19]. All 18 study
507 participants, who were all adult patients diagnosed with T1D over 60 months before recruitment
508 into the study, were selected from the 3-day interval group and were treated with IL-2 with doses
509 ranging from 0.2 to 0.47 × 10^6 IU/m^2.

510 FACS-based replication of the single-cell multiomics findings was performed in two follow-up
511 cohorts: (i) a single-dosing cohort, comprising 6 DILT1D patients[18] treated with a single dose of
512 IL-2 ranging from 0.6 to 1.5 x 10^6 IU/m^2; and (ii) a multiple dosing cohort, comprising 5
513 DILfrequency patients from the three-day dosing regimen, treated with IL-2 doses ranging from
514 0.2 to 0.32 × 10^6 IU/m^2. Study participants' characteristics and immune profiling at baseline are
515 summarised in **Supplementary Table 1**.

516

517 **Flow cytometry**

518 Flow cytometric characterisation of fresh whole-blood samples from the DILfrequency study
519 participants was performed at each visit within 4 h of phlebotomy, as previously described[20].
520 Briefly, 150 µl whole blood were incubated for 45 min at room temperature with fluorochrome-
521 conjugated antibodies (**Supplementary Table 2, 2nd panel**). Red blood cells were then lysed (BD
522 FACS Lysing solution). The absolute number of the main lymphocyte populations, including
523 $CD4^+$ T, $CD8^+$ T and $CD56^+$ NK cells, was assessed using a whole-blood BD Multitest 6-Color
524 TBNK assay using BD Trucount Tubes according to the manufacturers' instructions (BD
525 Biosciences) at each visit. Absolute numbers of $CD4^+$ Tregs and Tconvs, and $CD56^{br}$ and $CD56^{dim}$
526 NK cells were derived by multiplying the absolute number of $CD4^+$T cells and $CD56^+$ NK cells
527 by the appropriate percentages derived from the panel described above.

528 For the intracellular immunostainings, cryopreserved PBMCs were thawed at 37°C and
529 resuspended drop-by-drop in X-VIVO 15 (Lonza) with 1% heat-inactivated, filtered human AB
530 serum (Sigma). PBMC samples were selected from 10 visits (Days 0, 1, 2, 3, 4, 5, 6, 9, 14 and 28)
531 from each patient from the single-dosing and 4 visits (Days 0, 3, 27 and 55) for the multiple dosing
532 cohort. PBMCs were then washed in PBS, incubated with Fixable Viability Dye eFluor 780
533 (eBioscience) for 15 min at 4°C and stained with fluorochrome-conjugated antibodies against
534 surface-expressed markers (**Supplementary Table 2)** for 45 min at 4ºC. Fixation and
535 permeabilisation was performed using the FOXP3 Fix/Perm Buffer Set (eBioscience) according
536 to the manufacturer's instructions, and cells were then stained with fluorochrome-conjugated
537 antibodies against intracellular markers (**Supplementary Table 2)** for 1 h at room temperature.

538 Immunostained samples were acquired on a BD Fortessa (BD Biosciences) flow cytometer with
539 FACSDiva software (BD Biosciences) and analysed using FlowJo (Tree Star, Inc.). Information
540 for all fluorochrome-conjugated antibody panels used in this study is provided in Supplementary
541 Table 2.

542 ***In vitro* Treg suppression assay**

543 A total of 12 DILfrequency participants were selected for this analysis, including nine participants
544 that were also included in the single-cell analyses. For each participant, cells sampled from three
545 time points were used: Day 0, Day 24 and Day 55. Cryopreserved PBMCs were thawed as

546 described above and stained with a cocktail of monoclonal antibodies (**Supplementary Table 2**)
547 for cell sorting. Suppression assays were established in V-bottom 96-well plates by sorting 500
548 $CD4^{+}CD25^{-/lo}CD127^{+}$ effector T cells (Teffs) in the presence or absence of
549 $CD4^{+}CD25^{high}CD127^{low}$ Tregs at various ratios (Treg:Teff 0:1, 1:4, 1:2 and 1:1) with 1×10^{3}
550 $CD19^{+}$ B cells, using the BD FACSAria III flow cytometer automated cell deposition unit (BD
551 Biosciences). Cells were sorted into in 150 µl X-VIVO 15 supplemented with Penicillin-
552 Streptomycin-Fungizone (Gibco) and 10% heat-inactivated, filtered human AB sera, stimulated
553 with PHA (4 µg/ml; Alere) and incubated at 37°C, 5% CO_2, for 5 days. Proliferation was assessed
554 by the addition of 0.5 µCi/well [3H] thymidine (PerkinElmer) for the final 20 h of co-culture.
555 Conditions were run in 5 replicates, and proliferation readings (counts per minute [CPM])
556 averaged. Two samples with averaged proliferation less than 1,000 CPM from the Teff wells alone
557 were excluded from the analysis. The percentage suppression in each culture was calculated using
558 the following formula: percent suppression = 100 − [(CPM in the presence of Tregs ÷ CPM in the
559 absence of Tregs) × 100]. All time points from a participant were analysed concurrently.

560

561 **Single-cell multiomics: cell preparation and capture**

562 Single-cell multiomics profiling was performed using the BD Rhapsody system on PBMC aliquots
563 from 13 of the DILfrequency participants treated with the 3-day interval dosing schedule
564 (**Supplementary Table 1**) collected at the baseline visit (Day 0), 3 days after the last dose of IL-
565 2, immediately prior to the last IL-2 infusion of the dosing phase (Day 27) and one month after the
566 last dose of IL-2 (Day 55). Cryopreserved PBMCs were thawed at 37°C and resuspended drop-
567 by-drop in X-VIVO 15 with 1% heat-inactivated, filtered human AB serum. After washing in PBS,
568 cells were incubated with Fixable Viability Dye eFluor 780 (eBioscience) for 10 min at room
569 temperature, washed with cold PBS + 2% FBS and incubated for 30 min at 4ºC with fluorochrome-
570 conjugated antibodies for sorting (**Supplementary Table 2**). Cells were then washed two times
571 and resuspended in cold PBS + 1% FBS for cell sorting at 4ºC in a BD FACSAria Fusion sorter
572 (BD Biosciences). The following T and NK cell subsets were sorted from each participant at each
573 visit: (i) $CD3^{-}CD56^{hi}$ ($CD56^{br}$ NK; (ii) $CD3^{-}CD56^{+}$ ($CD56^{dim}$ NK; (iii) $CD3^{+}CD8^{+}$ ($CD8^{+}$ T); (iv)
574 $CD3^{+}CD4^{+}$ $CD25^{-/low}$ ($CD4^{+}$ Tconv); and (v) $CD3^{+}CD4^{+}$ $CD127^{low}CD25^{hi}$ ($CD4^{+}$ Treg). We

575 aimed to sort a total of 130,000 cells for the Day 0 and Day 55 visits and 160,000 for the Day 27
576 visit, with the following proportion of each of the sorted cell populations: 30% $CD4^+$ Treg; 25%
577 $CD4^+$ Tconv and $CD8^+$ T; 12% $CD56^{br}$ NK and 8% $CD56^{dim}$ NK cells.

578 Following cell sorting, each sorted subset was labelled with the respective sample barcoding
579 antibody (sample multiplexing kit; BD Biosciences) for 20 min at 4ºC to allow for the
580 identification of the sorting gate and visit of each captured single cell. To minimise day-to-day
581 variation, we processed the three PBMC samples corresponding to the three visits from each
582 participant on the same day. As the number of barcoded oligo-conjugated antibodies available in
583 the kit was less than the total number of sorted subsets, we combined the $CD4^+$ Treg and $CD56^{dim}$
584 NK cells as well as the $CD4^+$ Tconv and $CD56^{br}$ NK cells from each visit and labelled the pooled
585 cells with the same barcode. These combined subsets were chosen for their highly differentiated
586 transcriptional and proteomics profile, which allowed robust separation of the respective original
587 subsets at the analysis stage. Cells were then washed three times with BD Sample Buffer (BD
588 Biosciences) at 4ºC to remove any residual unbound barcoding antibody and then pooled together
589 for downstream processing.

590 To profile unstimulated cells, half of the pooled cells volume (corresponding to ~210,000 cells)
591 were initially incubated at 4ºC for 5 min with human Fc block (BD Biosciences) and then for a
592 further 45 min with a master mix of 65 oligo-conjugated AbSeq antibodies (BD Bioscience;
593 **Supplementary Table 2**). Cells were then washed three times with BD Sample Buffer at 4ºC to
594 remove residual unbound oligo-conjugated AbSeq antibodies, resuspended in 500 ul cold BD
595 Sample buffer and filtered through a sterile 50 µm Filcon cup-type filter (BD Biosciences) for cell
596 counting. Samples were then resuspended in 620 µl of cold BD sample buffer at a concentration
597 of 40 cells/µl - for an estimated capture rate of ~20,000 single-cells / cartridge - and immediately
598 loaded on two BD Rhapsody cartridges (BD Biosciences) for single-cell capture.

599 For *in vitro* stimulation, the remaining volume from the pooled cells was washed at 4ºC and
600 resuspended in X-VIVO 15 + 10% heat-inactivated, filtered human AB serum at a final
601 concentration of 2×10^6 cells/ml. A volume of 100 µl (~200,000 cells) was then incubated in one
602 well of a round-bottom 96-well plate at 37ºC for 90 minutes with a PMA and ionomycin cell
603 stimulation cocktail (eBioscience), in the absence of protein transport inhibitors. Cells were

604 harvested into a FACS tube, washed with PBS + 2% FBS and processed for cell capture, as detailed
605 above for the unstimulated cells.

606

607 **Single-cell multiomics: cDNA library preparation and sequencing**

608 Single-cell capture, and cDNA library preparation was performed using the BD Rhapsody Express
609 single-cell analysis system (BD Biosciences), according to the manufacturer's instructions. cDNA
610 was initially amplified for 11 cycles (PCR1) using the pre-designed Human T-cell Expression
611 primer panel (BD Biosciences) containing 259 primer pairs, together with a custom designed
612 primer panel containing 306 primer pairs (BD Biosciences), described previously[20]. A total of 565
613 primer pairs targeting 534 different genes were targeted for amplification with this targeted panel
614 (**Supplementary Table 2**).

615 The resulting PCR1 products were purified using AMPure XP magnetic beads (Beckman Coulter)
616 and the respective mRNA and AbSeq/sample tag products were separated based on size selection,
617 using different bead ratios (0.7× and 1.2×, respectively). The purified mRNA and sample tag PCR1
618 products were further amplified (10 cycles) using a nested PCR approach and the resulting PCR2
619 products purified by size selection (0.8× and 1.2× for the mRNA and sample tag libraries,
620 respectively). The concentration, size and integrity of the resulting PCR products was assessed
621 using both Qubit (High Sensitivity dsDNA kit; Thermo Fisher) and the Agilent 4200 Tapestation
622 system (Agilent). The final products were normalised to 2.5 ng/µl (mRNA), 1.1 ng/µl (sample tag)
623 and 0.35 ng/µl (AbSeq) and underwent a final round of amplification (six cycles for mRNA and
624 sample tag and 7 cycles for AbSeq) using indexes for Illumina sequencing to prepare the final
625 libraries. Final libraries were quantified using Qubit and Agilent Tapestation and pooled
626 (~29/67/4% mRNA/AbSeq/sample tag ratio) to achieve a final concentration of 5 nM. Final pooled
627 libraries were spiked with 15% PhiX control DNA to increase sequence complexity and sequenced
628 (150 bp paired-end) on a NovaSeq 6000 sequencer (Illumina).

629

630 **Pre-processing of single-cell sequencing data**

631 The single-cell sequencing reads were processed following instructions from BD Biosciences
632 described earlier[27], with slight modifications. First, low-quality read pairs were removed based on
633 read length, mean base quality score and highest single-nucleotide frequency. High-quality R1
634 reads were analysed to extract cell labels and unique molecular identifier (UMI) sequences. High-
635 quality R2 reads were aligned to the reference panel sequences using Bowtie2[70]. Reads having the
636 identical cell labels and UMI sequences and aligned to the same gene were collapsed into a single
637 molecule. To correct sequencing and PCR errors, the obtained counts were adjusted by a recursive
638 substitution error correction (RSEC) algorithm developed by BD Biosciences. The sampling time
639 point and sorting gate of origin of each cell were labelled using information from barcoded oligo-
640 conjugated antibodies. Cells without barcoding information were labelled as "tag N/A", and cells
641 with two or more barcodes were labelled as "multiplet". We note that sample barcoding and AbSeq
642 staining efficiency was compromised in $CD56^{br}$ NK cells. As the quality of the main mRNA library
643 was not affected by this technical issue, $CD56^{br}$ NK cells without barcoding information were
644 included in the quality control and clustering step, but excluded from subsequent analyses
645 dependent on sampling time point (see below). This led to a significant reduction in the number of
646 $CD56^{br}$ NK cells analysed and a concomitant reduction in statistical power to identify IL-2-induced
647 alterations. Nevertheless, we also note that our cell-enrichment strategy compensated for this cell
648 loss due to technical reasons and provided sufficient resolution to dissect the heterogeneity of the
649 rare population of $CD56^{+}$ NK cells.

650

651 **Doublet scoring**

652 Doublet scoring was performed on each sample separately using Scrublet[71]. Briefly, this method
653 simulates synthetic doublets by sampling pairs of cells and then scores each cell by its similarity
654 to the simulated doublets. For each sample, count matrices for RNA and AbSeq data were
655 concatenated and used as the input. The method was modified to exclude known multiplet-tagged
656 cells from the doublet simulation while retaining them for scoring. The doublet score was used to
657 help identify clusters of doublets in subsequent quality control stages.

658

659 **Normalisation, integration, dimensionality reduction and clustering**

660 Data normalisation was performed using Seurat[72]. The RNA count matrices were normalised by
661 log normalisation. Specifically, the RNA counts for each cell were (i) divided by the total counts
662 for that cell, (ii) multiplied by a scale factor of 10,000, and (iii) natural-log transformed after
663 adding one pseudo count. The AbSeq counts for each cell were considered compositional and
664 normalised by a centred log ratio transformation[73]. Normalised RNA and AbSeq expression
665 matrices were then centred and scaled. Specifically, each feature was linearly regressed against
666 selected latent variables including the number of RNA and AbSeq features, and the donor of origin,
667 where appliable. The resulting residuals were mean-centred and divided by their standard
668 deviations.

669 Integration of the scaled AbSeq expression matrices from different participants were performed
670 using a combination of canonical correlation analysis (CCA) and identification of mutual nearest
671 neighbours (MNNs), implemented in Seurat[72]. After integration was performed, the updated
672 AbSeq expression matrices produced by the integration algorithm were used in subsequent
673 dimensionality reduction and clustering.

674 Dimensionality reduction and clustering were performed using Seurat[72]. Specifically, principal
675 components (PCs) were calculated separately for each assay using the top variable features of the
676 scaled or integrated expression matrices, and a weighted nearest neighbour (WNN) graph as well
677 as a weighted shared nearest neighbour (WSNN) graph were generated on the ten top PCs from
678 each assay, unless otherwise specified. We used $k = 30$ nearest neighbours for each cell. Uniform
679 Manifold Approximation and Projection (UMAP)[74] embeddings were then calculated based on the
680 WNN graph. The Louvain algorithm[75] was applied to identify clusters of cells based on a WSNN
681 graph, at the selected resolution level. Clusters with fewer than ten cells were removed. The
682 resulting clusters were manually annotated based on marker genes and sorting gate information to
683 elucidate cell types and label suspicious clusters.

684

685 **Data quality control**

686 The BD Rhapsody single-cell sequencing data generated in this study was processed through a
687 pipeline consisting of multiple quality control steps as described below. Methodological details of
688 each step are specified in previous sections. The single-cell sequencing data of each sample (i.e.
689 the collection of stimulated and unstimulated cells for a single participant) were pre-processed to
690 obtain two annotated count matrices (RNA and AbSeq). We performed data normalisation,
691 dimensionality reduction and clustering for each sample. Specifically, 30 RNA principal
692 components (PCs) and 30 AbSeq PCs were used to generate the WNN and WSNN graphs, and
693 clustering was performed at resolution 0.5.

694 Within each sample, cells meeting one of the following criteria were removed: (1) cells that are
695 labelled as "multiplet" or in clusters with high doublet scores; (2) cells labelled as "tag N/A",
696 except those in clusters annotated as $CD56^{br}$; (3) cells in clusters with very low RNA counts and
697 very low or very high AbSeq counts; (4) cells in clusters annotated as monocyte or B cell
698 contamination; (5) cells labelled as DN T cells.

699 The filtered cells from each participant were merged according to the stimulation status into two
700 datasets (unstimulated cells and *in vitro* stimulated cells). Both stimulated and unstimulated cells
701 were then processed in the same way unless otherwise specified. We performed data normalisation,
702 dimensionality reduction and clustering for each merged dataset. Specifically, clustering was
703 performed at resolution 0.7 (unstimulated cells) or 1.5 (stimulated cells). Doublet clusters were
704 manually annotated and removed. Data normalisation, dimensionality reduction and clustering
705 were performed again. Specifically, clustering was performed at resolution 0.5.

706 Cells in each filtered dataset were subsequently partitioned into four major groups ($CD4^+$ Treg,
707 $CD4^+$ Tconv, CD8+ T and $CD56^+$ NK cells) based on cluster annotations and sorting gates of
708 origin. In addition, unstimulated cells in clusters marked by genes related to cell cycle were
709 grouped as cycling cells. We chose to partition cycling cells into one separate group based on the
710 following considerations: (i) cycling cells were relatively rare in numbers (0.72% of total
711 unstimulated cells); (ii) cycling cells clusters had well-defined mRNA markers; (iii) The
712 phenotypical differences between cycling cells and their non-cycling counterparts were potentially
713 larger than the heterogeneity within each major cell populations.

714 After partitioning, doublet clusters were manually annotated and removed. Data normalisation,
715 dimensionality reduction, integration and clustering were performed in each group of partitioned
716 cells. Specifically, clustering was performed at resolution 0.5. Finally, data normalisation,
717 dimensionality reduction, and clustering were performed again.

718 Owing to the aforementioned technical limitations with AbSeq staining in $CD56^{br}$ NK cells, AbSeq
719 data was not used in dimensionality reduction and clustering of NK cells. The following
720 resolutions were used for the final clustering: unstimulated Tregs, 0.6; unstimulated Tconvs, 0.5;
721 unstimulated CD8, 0.5; unstimulated NK, 0.3; unstimulated cycling cells, 0.5; stimulated Tregs,
722 0.5; stimulated Tconvs, 0.4; stimulated CD8: 0.5; stimulated NK: 0.5. The resulting partitioned
723 datasets were used for subsequent analyses. We note that one PBMC aliquot (corresponding to the
724 Day 55 visit of Participant 8) yielded very low cell numbers (N = 603 unstimulated and N = 67
725 stimulated cells) and displayed a compromised FACS staining profile. These cells were included
726 in quality control and clustering procedures but excluded from downstream analyses. All other 38
727 samples corresponding to 38 visits yielded the expected cell frequencies and numbers.

728

729 **Single-cell proliferation scores**

730 Single-cell proliferation scores were calculated using a previously described approach[76], which is
731 based on the average normalised expression levels of a pre-selected set of 11 mRNA features
732 related to cell cycle (*AURKB*, *HMGB2*, *HMMR*, *MCM4*, *MKI67*, *PCLAF*, *PCNA*, *TK1*, *TOP2A*,
733 *TYMS*, and *UBE2C*), subtracted by the aggregated expression of a control set of 50 randomly
734 selected mRNA features. The proliferation scores were used to identify two cycling clusters from
735 the 15 functional T and NK cell subsets identified in blood from the initial clustering
736 (**Supplementary Fig. 3a**). We noted that the distinct co-expression of these cell-cycle genes
737 present in our targeted transcriptional panel superseded more subtle functional differences and
738 aggregated all cycling T and NK cells into two respective clusters, regardless of their original
739 sorting gate. Given this lack of functional differentiation and to avoid the potential overwhelming
740 effect of these cell-cycle genes on the resulting clustering visualisation, we opted to separate these
741 cycling T and NK cells from the rest of the cells included in subsequent clustering steps to assess
742 IL-2-induced changes in their relative frequency in blood.

743

744 **Cluster annotation**

745 Functional annotation of the resulting clusters was performed manually based on the cluster-
746 specific differential expression of the mRNA and protein markers (summarised in **Supplementary**
747 **Data 1**). Sample tagging information, corresponding to sorting gate information, was used to sub-
748 cluster the five main immune populations ($CD4^+$ $CD127^{low}CD25^{hi}$ Treg; $CD4^+$ $CD25^{-/low}$ Tconv;
749 $CD8^+$ T; $CD56^{br}$ NK and $CD56^{dim}$ NK cells). The use of a bespoke targeted single-cell approach
750 combined with a cell-subset enrichment strategy provided a high-resolution map of the
751 heterogeneity of these cell populations – and particularly of the rare circulating $CD4^+$ Treg and
752 $CD56^{br}$ NK cell subsets.

753 We note that a consequence of the cell-subset enrichment strategy used in this study is that the
754 frequency of the T and NK cell subsets described in this dataset do not directly represent their
755 frequency in whole blood. The aim of this study was not to identify changes in the global
756 composition of PBMCs, but to specifically focus on the T and NK cell subsets. The pre-purification
757 of the Treg and $CD56^{br}$ NK subsets was central to the resolution of this approach and provided
758 greater power to dissect their functional heterogeneity and investigate how their relative
759 composition was modified by LD-IL-2 immunotherapy

760

761 **Functional annotation of $CD4^+$ $CD127^{low}CD25^{hi}$ T cell clusters**

762 Owing to our cell-subset enrichment strategy, we obtained a high-resolution map depicting the
763 heterogeneity of $CD127^{low}CD25^{hi}$ T cells in blood, with 13 distinct clusters identified in
764 unstimulated cells (**Supplementary Fig. 4a**) and 12 in *in vitro* stimulated cells (**Supplementary**
765 **Fig. 4b**). Overall, we found consistency in the functional annotation of the identified subsets in
766 stimulated and unstimulated cells, with a clear demarcation of the naïve and memory subsets.

767 Expression of the canonical Treg transcription factors *FOXP3* and *IKZF2* (encoding HELIOS) was
768 used to identify three distinct groups of clusters, corresponding to different populations of
769 $CD127^{low}CD25^{hi}$ T cells: (i) $CD45RA^+$ $FOXP3^+HELIOS^+$ clusters (depicted in green)

770 corresponding to thymic-derived naïve Tregs; (ii) CD45RA^{-} FOXP3^{+}HELIOS^{+} clusters (depicted
771 in blue) corresponding to memory Tregs with suppressive function; and (iii) CD45RA^{-} CD25^{+}
772 FOXP3^{-}HELIOS^{-} clusters (depicted in red) corresponding to a small subset of Teffs expressing
773 CD25 likely due to recent activation (**Supplementary Fig. 5**). Additional clusters showing
774 variable expression of FOXP3 but lack of HELIOS expression (FOXP3^{+}HELIOS^{-} clusters) were
775 depicted in black, and represent a more heterogeneous group of Treg subsets, containing a mix of
776 thymic-derived and induced Treg subsets.

777 As expected, most of the cells within the CD127^{low}CD25^{hi} Treg gate showed concomitant
778 expression of FOXP3 and HELIOS, which is consistent with their largely demethylated *FOXP3*
779 Treg-specific demethylated region (TSDR)[37], the hallmark of *bona fide* thymic Tregs.
780 Furthermore, we were able to identify a trajectory of thymic Treg differentiation, originating from
781 the naïve FOXP3^{+}HELIOS^{+} Tregs (cluster 0). Memory FOXP3^{+}HELIOS^{+} Tregs displayed more
782 heterogeneity and included four distinct subsets in unstimulated cells, including a cluster of CD80^{+}
783 Tregs characterised by elevated expression of tissue-homing receptors (cluster 7) and a cluster of
784 effector Tregs (cluster 1) typically marked by the expression of HLA class II and other effector
785 Treg markers such as CD39 and GITR (**Supplementary Fig. 4a**). We have also identified a subset
786 of CD45RA^{+} naïve cells (cluster 2) showing much lower expression of FOXP3 and HELIOS
787 compared to the classical naïve Treg cluster. This likely corresponds to a subset of
788 homeostatically-expanded CD45RA^{+} T cells upregulating CD25 that we have previously
789 characterised[77]. Consistent with this non-Treg profile, these CD25^{+} naïve T cells upregulated the
790 expression of IL-2 upon *in vitro* stimulation (**Supplementary Fig. 5f**). The expression of IL-2 in
791 stimulated cells was also a hallmark of the CD25^{+} FOXP3^{-}HELIOS^{-} Teff clusters and allowed us
792 to further refine their functional heterogeneity. Moreover, the relative frequency of CD45RA^{-}
793 FOXP3^{-}HELIOS^{-} cells identified in this single-cell dataset is consistent with the frequency of cells
794 identified by FACS as cytokine-producing FOXP3^{-}HELIOS^{-} cells in the CD127^{low}CD25^{hi} Treg
795 gate that we have previously shown to contain a methylated TSDR[37], further indicating that they
796 correspond to a small proportion of activated CD25^{+} FOXP3^{-}HELIOS^{-} Teffs captured in the
797 CD127^{low}CD25^{hi} Treg gate.

798

799 **Functional annotation of CD56$^+$ NK cell clusters**

800 In contrast to T cells, we found much lower heterogeneity in NK cells (**Fig. 4d** and **Supplementary**
801 **Fig. 13**). In addition, the technical issue affecting the efficiency of the AbSeq staining on CD56^{br}
802 NK cells, precluded the use of protein data for the clustering and annotation of the CD56$^+$ NK
803 cells, which also contributed to a lower resolution of the clusters. Nevertheless, our cell-
804 enrichment strategy allowed us to generate a comprehensive single-cell map of NK cell
805 heterogeneity, most notably of the rare, IL-2-sensitive CD56^{br} NK population. We observed
806 differentiation of CD56^{br} NK cells from a rare progenitor subset marked by the expression of genes
807 associated with haematopoiesis such as SOX4 and KIT, and characterization of two functional
808 subsets associated with a trajectory of CD56^{br} NK cell maturation, which was marked by HLA
809 class II gene expression in the more differentiated cells. In contrast, CD56^{dim} NK cells showed a
810 distinct transcriptional profile of two distinct subsets, reflecting a gradient of NK cell activation
811 associated with the acquisition of a cytotoxic profile (**Fig. 4d** and **Supplementary Fig. 13**). These
812 findings support a distinct functional differentiation between the CD56^{dim} and CD56^{br} subsets,
813 which allowed clear identification a fraction of CD56^{dim} NK cells sorted in the CD56^{br} gate, as
814 well as a fraction of CD56^{br} NK cells sorted within the CD56^{dim} gate (**Fig. 4e**).

815

816 **Differential abundance analysis**

817 To identify specific cell frequency changes across different sampling time points, we calculated
818 the frequency of each cell type annotated. A cell type was defined as a group of cells from the
819 same cluster or several similar clusters, after removing cells not sorted from the corresponding
820 gate. The frequency of each cell type for each participant and each time point was calculated as
821 the proportion of that cell type within all cells from the same participant, time point and sorting
822 gate of origin. For each cell type, a two-sided Wilcoxon signed-rank test was performed to compare
823 the frequencies at Day 0 with the frequencies at Day 27 or Day 55 in the 13 participants selected
824 for single-cell analysis. Benjamini-Hochberg FDR correction was applied after pooling all
825 resulting *P* values. For each cell type and each participant, the $\log_2$ fold change values between
826 corresponding frequency values were calculated and visualised. We note that cells were compared

827 only if they were from the same sorting gate, as cells from different sorting gates were pooled in
828 designated proportions that are not biologically relevant.

829

830 **Generation and normalisation of pseudo-bulk expression data**

831 For the DILfreq dataset, unstimulated and stimulated cells were separately partitioned into five
832 groups (Treg, Tconv, CD8, $CD56^{br}$ and $CD56^{dim}$), after removing cells not sorted from the
833 corresponding gate. In each group, cells from the same participant, time point and stimulation
834 status were aggregated into one pseudo-bulk sample by summarising raw counts of each mRNA
835 or AbSeq feature. For the COMBAT and INCOV datasets, the pseudo-bulk expression data for
836 each participant and each cell type were obtained from the authors, and samples with less than
837 2,000 total RNA counts were removed. For the INCOV dataset, samples from non-COVID-19,
838 immunocompromised or immunosuppressed participants were additionally removed.

839

840 **Differential expression analysis**

841 Differential expression analysis was performed separately for RNA and AbSeq data from raw
842 pseudo-bulk counts using DESeq2[78]. Specifically, the likelihood ratio test was used, with a full
843 model including time points and the participants as independent variables, and a reduced model
844 including only participants as the independent variable. The apeglm method[79] was applied to
845 shrink the resulting fold change values, and the Benjamini-Hochberg FDR correction was applied
846 after pooling all resulting *P* values (**Supplementary Data 2**). Genes with either (i) absolute log2
847 fold change values equal to or greater than 0.4 and FDR-adjusted *P* values less than 0.01, or (ii)
848 FDR-adjusted *P* values less than 1×10^{-10}, were selected as significantly differentially expressed
849 genes, unless otherwise noted. Participant-specific $\log_2$ fold change values were calculated directly
850 from the normalised pseudo-bulk expression data.

851

852 **Day 55 signature scores**

853 Forty-one genes that were significantly upregulated or downregulated in at least one unstimulated
854 cell population comparing Day 55 with Day 0 were defined as Day 55 signature genes, from which
855 the Day 55 signature scores were calculated. Within each dataset, the Day 55 signature score was
856 defined for each pseudo-bulk sample as the sum of z-scores of normalised expression levels of
857 upregulated signature genes, subtracted by that of downregulated signature genes. For each
858 participant and cell type in the DILfrequency dataset, the Δ signature scores were defined as the
859 signature score differences between Day 27 or Day 55 and Day 0, as indicated.

860

861 **Pseudo-time trajectory analysis**

862 Pseudo-time trajectory analysis was performed using Slingshot[80] and tradeSeq[81]. First, 10-
863 dimensional UMAP embeddings were generated for stimulated $CD4^+$ T cells based on RNA and
864 AbSeq data, as described above. Second, the Slingshot algorithm was applied to UMAP data and
865 the manually annotated cluster labels, with naïve cells selected as the starting point, and other
866 parameters set to default. Finally, the resulting pseudo-time data were used as the input for the
867 tradeSeq algorithm to model the expression levels of each gene along each trajectory.

868

869 ## Data availability

870 The single-cell sequencing data generated in this study have been deposited in Gene Expression
871 Omnibus (GEO) under accession code GSE201197
872 (https://www.ncbi.nlm.nih.gov/geo/query/acc.cgi?acc=GSE201197).

873

874 ## Code availability

875 The custom code used in the study for data analyses and visualisation has been deposited in
876 Zenodo (https://doi.org/10.5281/zenodo.7116340).

Acknowledgements

We thank all participants in DILT1D and DILfrequency for their generous contribution to this study. The authors also acknowledge the support of the NIHR Cambridge Biomedical Research Centre and the Cambridge Clinical Trial Unit for trial coordination; the NIHR/Wellcome Trust Clinical Research Facility and Addenbrooke's Centre for Clinical Investigation for clinical facilities; the Department of Clinical Immunology, Addenbrooke's Hospital; the JDRF/Wellcome Diabetes and Inflammation laboratory sample processing team (led by Helen Stevens) and information technology and administration team (led by Judy Brown) and data teams at the Cambridge Institute for Medical Research. We thank Shannah Donhou, Sarune Kacinskaite and Heather McMurray, University of Oxford for sample collection and preparation, and members of the Diabetes and Inflammation Laboratory for critical discussion. We thank Justin Whalley, Georgina Kerr, Brian Marsden and Julian Knight, University of Oxford, for providing access to clinical data collected from the COMBAT cohort. We also thank Yapeng Su, and Dan Yuan from Institute for Systems Biology, and Jason D. Goldman from Swedish Medical Center, for providing access to the annotated single-cell data collected from the INCOV cohort.

Funding

This work was supported by the Sir Jules Thorn Trust (13/JTA (OCT2013/DR/1044)), the JDRF (1-SRA-2019-657-A-N), and the NIHR Cambridge Biomedical Research Centre. The Diabetes and Inflammation Laboratory was supported by a strategic award from the Wellcome (107212/A/15/Z) and the JDRF (4-SRA-2017-473-A-A). JYZ was supported by the China Scholarship Council-University of Oxford Scholarship. The research was supported by the Wellcome Trust Core Award Grant Number 203141/Z/16/Z with additional support from the NIHR Oxford BRC. The University of Cambridge has received salary support for M.L.E. through the National Health Service in the East of England through the Clinical Academic Reserve. The views expressed are those of the author(s) and not necessarily those of the NHS, the NIHR or the Department of Health.

Author contributions

L.S.W., J.A.T. and R.C.F. conceptualised this work and designed the experiments. M.L., L.G. and R.C.F. performed the scRNA-seq experiments. J-Y.Z. led the analysis of the scRNA-seq data with help from F.H. and D.T. M.M. and J.H.M.Y. performed the in vitro suppression experiments and analysed the data under the supervision of T.I.M.T. M.L.P. and R.C.F. performed FACS experiments and analysed the data. J.K., F.W-L. and M.L.E. supervised the DILfrequency study. T.I.M.T. provided conceptual advice on the experiments. J-Y.Z., L.S.W, J.A.T. and R.C.F. wrote the manuscript with input from all authors.

Competing interests

F.W-L. is employed by Vertex Pharmaceuticals; J.A.T. is a member of the GSK Human Genetics Advisory Board. The remaining authors declare no competing interests.

915 **References**

916 1. Koreth, J. *et al.* Interleukin-2 and Regulatory T Cells in Graft-versus-Host Disease. *New*
917 *Engl J Med* **365**, 2055–2066 (2011).
918 2. Saadoun, D. *et al.* Regulatory T-Cell Responses to Low-Dose Interleukin-2 in HCV-
919 Induced Vasculitis. *New Engl J Med* **365**, 2067–2077 (2011).
920 3. Castela, E. *et al.* Effects of Low-Dose Recombinant Interleukin 2 to Promote T-
921 Regulatory Cells in Alopecia Areata. *JAMA Dermatol* **150**, 748–751 (2014).
922 4. von Spee-Mayer, C. *et al.* Low-dose interleukin-2 selectively corrects regulatory T cell
923 defects in patients with systemic lupus erythematosus. *Ann Rheum Dis* **75**, 1407–1415
924 (2016).
925 5. Zhao, T. X. *et al.* Low-dose interleukin-2 in patients with stable ischaemic heart disease
926 and acute coronary syndromes (LILACS): protocol and study rationale for a randomised,
927 double-blind, placebo-controlled, phase I/II clinical trial. *BMJ Open* **8**, e022452 (2018).
928 6. He, J. *et al.* Efficacy and safety of low-dose IL-2 in the treatment of systemic lupus
929 erythematosus: a randomised, double-blind, placebo-controlled trial. *Ann Rheum Dis* **79**,
930 141–149 (2020).
931 7. Klatzmann, D. & Abbas, A. K. The promise of low-dose interleukin-2 therapy for
932 autoimmune and inflammatory diseases. *Nat Rev Immunol* **15**, 283–294 (2015).
933 8. Graßhoff, H. *et al. Low-Dose IL-2 Therapy in Autoimmune and Rheumatic Diseases*.
934 *Front Immunol* **12**, e648408 (2021).
935 9. Kolios, A. G. A., Tsokos, G. C. & Klatzmann, D. Interleukin-2 and regulatory T cells in
936 rheumatic diseases. *Nat Rev Rheumatol* **17**, 749–766 (2021).
937 10. Ghosh, S. *et al.* Polygenic control of autoimmune diabetes in nonobese diabetic mice. *Nat*
938 *Genet* **4**, 404–409 (1993).
939 11. Todd, J. A. Etiology of Type 1 Diabetes. *Immunity* **32**, 457–467 (2010).
940 12. Hulme, M. A., Wasserfall, C. H., Atkinson, M. A. & Brusko, T. M. Central Role for
941 Interleukin-2 in Type 1 Diabetes. *Diabetes* **61**, 14–22 (2011).
942 13. Yamanouchi, J. *et al.* Interleukin-2 gene variation impairs regulatory T cell function and
943 causes autoimmunity. *Nat Genet* **39**, 329–337 (2007).
944 14. Tang, Q. *et al.* Central Role of Defective Interleukin-2 Production in the Triggering of
945 Islet Autoimmune Destruction. *Immunity* **28**, 687–697 (2008).
946 15. Hartemann, A. *et al.* Low-dose interleukin 2 in patients with type 1 diabetes: a phase 1/2
947 randomised, double-blind, placebo-controlled trial. *Lancet Diabetes Endocrinol* **1**, 295–
948 305 (2013).
949 16. Rosenzwajg, M. *et al.* Low-dose interleukin-2 fosters a dose-dependent regulatory T cell
950 tuned milieu in T1D patients. *J Autoimmun* **58**, 48–58 (2015).
951 17. Rosenzwajg, M. *et al.* Low-dose IL-2 in children with recently diagnosed type 1 diabetes:
952 a Phase I/II randomised, double-blind, placebo-controlled, dose-finding study.
953 *Diabetologia* **63**, 1808–1821 (2020).
954 18. Todd, J. A. J. *et al.* Regulatory T cell responses in participants with type 1 diabetes after a
955 single dose of interleukin-2: a non-randomised, open label, adaptive dose-finding trial.
956 *PLoS Med* **13**, e1002139 (2016).

957 19. Seelig, E. *et al.* The DILfrequency study is an adaptive trial to identify optimal IL-2
958 dosing in patients with type 1 diabetes. *JCI Insight* **3**, (2018).
959 20. Trzupek, D. *et al.* Single-cell multi-omics analysis reveals IFN-driven alterations in T
960 lymphocytes and natural killer cells in systemic lupus erythematosus. *Wellcome Open Res*
961 **6**, (2021).
962 21. Kenefeck, R. *et al.* Follicular helper T cell signature in type 1 diabetes. *J Clin Invest* **125**,
963 292–303 (2015).
964 22. Ferreira, R. C. *et al.* IL-21 production by CD4+ effector T cells and frequency of
965 circulating follicular helper T cells are increased in type 1 diabetes patients. *Diabetologia*
966 **58**, 781–790 (2015).
967 23. Ekman, I. *et al.* Circulating CXCR5−PD-1hi peripheral T helper cells are associated with
968 progression to type 1 diabetes. *Diabetologia* **62**, 1681–1688 (2019).
969 24. von Herrath, M. *et al.* Anti-interleukin-21 antibody and liraglutide for the preservation of
970 β-cell function in adults with recent-onset type 1 diabetes: a randomised, double-blind,
971 placebo-controlled, phase 2 trial. *Lancet Diabetes Endocrinol* **9**, 212–224 (2021).
972 25. Bell, C. J. M. *et al.* Sustained in vivo signaling by long-lived IL-2 induces prolonged
973 increases of regulatory T cells. *J Autoimmun* **56**, 66–80 (2015).
974 26. Yu, A. *et al.* Selective IL-2 Responsiveness of Regulatory T Cells Through Multiple
975 Intrinsic Mechanisms Supports the Use of Low-Dose IL-2 Therapy in Type 1 Diabetes.
976 *Diabetes* **64**, 2172–2183 (2015).
977 27. Trzupek, D. *et al.* Discovery of CD80 and CD86 as recent activation markers on
978 regulatory T cells by protein-RNA single-cell analysis. *Genome Med* **12**, 55 (2020).
979 28. Ito, S. *et al.* Ultra-low Dose Interleukin-2 Promotes Immune-modulating Function of
980 Regulatory T Cells and Natural Killer Cells in Healthy Volunteers. *Mol Ther* **22**, 1388–
981 1395 (2014).
982 29. Humrich, J. Y. *et al.* Low-dose interleukin-2 therapy in refractory systemic lupus
983 erythematosus: an investigator-initiated, single-centre phase 1 and 2a clinical trial. *Lancet*
984 *Rheumatol* **1**, e44–e54 (2019).
985 30. Uxa, S. *et al.* Ki-67 gene expression. *Cell Death Differ* **28**, 3357–3370 (2021).
986 31. di Rosa, F., Cossarizza, A. & Hayday, A. C. To Ki or Not to Ki: Re-Evaluating the Use
987 and Potentials of Ki-67 for T Cell Analysis. *Front Immunol* **12**, (2021).
988 32. Muñoz-Ruiz, M. *et al.* Tracking immunodynamics by identification of S-G2/M-phase T
989 cells in human peripheral blood. *J Autoimmun* **112**, 102466 (2020).
990 33. Ariel, A. *et al.* IL-2 Induces T Cell Adherence to Extracellular Matrix: Inhibition of
991 Adherence and Migration by IL-2 Peptides Generated by Leukocyte Elastase. *J Immunol*
992 **161**, 2465 (1998).
993 34. Franitza, S. *et al.* TNF-α Associated with Extracellular Matrix Fibronectin Provides a Stop
994 Signal for Chemotactically Migrating T Cells. *The Journal of Immunology* **165**, 2738–
995 2747 (2000).
996 35. Wrenshall, L. E., Platt, J. L., Stevens, E. T., Wight, T. N. & Miller, J. D. Propagation and
997 Control of T Cell Responses by Heparan Sulfate-Bound IL-2. *J Immunol* **170**, 5470
998 (2003).
999 36. Miller, J. D., Clabaugh, S. E., Smith, D. R., Stevens, R. B. & Wrenshall, L. E. Interleukin-
1000 2 is present in human blood vessels and released in biologically active form by
1001 heparanase. *Immunol Cell Biol* **90**, 159–167 (2012).

1002 37. Ferreira, R. C. *et al.* Cells with Treg-specific FOXP3 demethylation but low CD25 are
1003 prevalent in autoimmunity. *J Autoimmun* **84**, 75–86 (2017).
1004 38. Singh, S. S. *et al.* Amphiregulin in cellular physiology, health, and disease: Potential use
1005 as a biomarker and therapeutic target. *J Cell Physiol* **237**, 1143–1156 (2022).
1006 39. West, N. R. *et al.* Oncostatin M drives intestinal inflammation and predicts response to
1007 tumor necrosis factor–neutralizing therapy in patients with inflammatory bowel disease.
1008 *Nat Med* **23**, 579–589 (2017).
1009 40. Richard, A. C. *et al.* Targeted genomic analysis reveals widespread autoimmune disease
1010 association with regulatory variants in the TNF superfamily cytokine signalling network.
1011 *Genome Med* **8**, 76 (2016).
1012 41. Maña, P. *et al.* LIGHT (TNFSF14/CD258) Is a Decisive Factor for Recovery from
1013 Experimental Autoimmune Encephalomyelitis. *J Immunol* **191**, 154–163 (2013).
1014 42. Ahern, D. J. *et al.* A blood atlas of COVID-19 defines hallmarks of disease severity and
1015 specificity. *Cell* **185**, 916-938 (2022).
1016 43. Su, Y. *et al.* Multiple early factors anticipate post-acute COVID-19 sequelae. *Cell* **185**,
1017 881-895.e20 (2022).
1018 44. Whangbo, J. S. *et al.* Functional analysis of clinical response to low-dose IL-2 in patients
1019 with refractory chronic graft-versus-host disease. *Blood Adv* **3**, 984–994 (2019).
1020 45. Whangbo, J. S. *et al.* Dose-escalated interleukin-2 therapy for refractory chronic graft-
1021 versus-host disease in adults and children. *Blood Adv* **3**, 2550–2561 (2019).
1022 46. Bielekova, B. *et al.* Regulatory CD56bright natural killer cells mediate
1023 immunomodulatory effects of IL-2Rα-targeted therapy (daclizumab) in multiple sclerosis.
1024 *Proc Natl Acad Sci USA* **103**, 5941–5946 (2006).
1025 47. Melsen, J. E., Lugthart, G., Lankester, A. C. & Schilham, M. W. Human Circulating and
1026 Tissue-Resident CD56bright Natural Killer Cell Populations. *Front Immunol* **7**, 262
1027 (2016).
1028 48. Ballesteros-Tato, A. *et al.* Interleukin-2 Inhibits Germinal Center Formation by Limiting T
1029 Follicular Helper Cell Differentiation. *Immunity* **36**, 847–856 (2012).
1030 49. Locci, M. *et al.* Activin A programs the differentiation of human TFH cells. *Nat Immunol*
1031 **17**, 976–984 (2016).
1032 50. He, J. *et al.* Low-dose interleukin-2 treatment selectively modulates CD4+ T cell subsets
1033 in patients with systemic lupus erythematosus. *Nat Med* **22**, 991–993 (2016).
1034 51. Liu, S. M. *et al.* Differential IL-21 signaling in APCs leads to disparate Th17
1035 differentiation in diabetes-susceptible NOD and diabetes-resistant NOD.Idd3 mice. *J Clin*
1036 *Invest* **121**, 4303–4310 (2011).
1037 52. Crotty, S. T Follicular Helper Cell Biology: A Decade of Discovery and Diseases.
1038 *Immunity* **50**, 1132–1148 (2019).
1039 53. Ren, H. M., Lukacher, A. E., Rahman, Z. S. M. & Olsen, N. J. New developments
1040 implicating IL-21 in autoimmune disease. *J Autoimmun* **122**, 102689 (2021).
1041 54. Sage, P. T. & Sharpe, A. H. T follicular regulatory cells. *Immunol Rev* **271**, 246–259
1042 (2016).
1043 55. Jacobsen, J. *et al.* Expression of Foxp3 by T follicular helper cells in end-stage germinal
1044 centers. *Science* **373**, eabe5146 (2021).
1045 56. Provine, N. M. & Klenerman, P. MAIT Cells in Health and Disease. *Annu Rev Immunol*
1046 **38**, 203–228 (2020).

1047 57. Tao, H. *et al.* Differential controls of MAIT cell effector polarization by
1048 mTORC1/mTORC2 via integrating cytokine and costimulatory signals. *Nat Commun* **12**,
1049 2029 (2021).
1050 58. Zhou, P. *et al.* Low-dose IL-2 therapy invigorates CD8+ T cells for viral control in
1051 systemic lupus erythematosus. *PLoS Pathog* **17**, e1009858 (2021).
1052 59. Matsumoto, A. *et al.* CIS, a Cytokine Inducible SH2 Protein, is a Target of the JAK-
1053 STAT5 Pathway and Modulates STAT5 Activation. *Blood* **89**, 3148–3154 (1997).
1054 60. Gill, K. L., Gardner, I., Li, L. & Jamei, M. A Bottom-Up Whole-Body Physiologically
1055 Based Pharmacokinetic Model to Mechanistically Predict Tissue Distribution and the Rate
1056 of Subcutaneous Absorption of Therapeutic Proteins. *AAPS J* **18**, 156–170 (2016).
1057 61. Bohnacker, S. *et al.* Mild COVID-19 imprints a long-term inflammatory eicosanoid- and
1058 chemokine memory in monocyte-derived macrophages. *Mucosal Immunol* (2022)
1059 doi:10.1038/s41385-021-00482-8.
1060 62. Phetsouphanh, C. *et al.* Immunological dysfunction persists for 8 months following initial
1061 mild-to-moderate SARS-CoV-2 infection. *Nat Immunol* **23**, 210–216 (2022).
1062 63. Marcovecchio, M. L. *et al.* Interleukin-2 Therapy of Autoimmunity in Diabetes (ITAD): a
1063 phase 2, multicentre, double-blind, randomized, placebo-controlled trial. *Wellcome Open*
1064 *Res* **5**, (2020).
1065 64. Ferreira, R. C. *et al.* Chronic Immune Activation in Systemic Lupus Erythematosus and
1066 the Autoimmune PTPN22 Trp620 Risk Allele Drive the Expansion of FOXP3+
1067 Regulatory T Cells and PD-1 Expression. *Front Immunol* **10,** 2606 (2019).
1068 65. Sims, E. K. *et al.* Teplizumab improves and stabilizes beta cell function in antibody-
1069 positive high-risk individuals. *Sci Transl Med* **13**, eabc8980 (2021).
1070 66. Quattrin, T. *et al.* Golimumab and Beta-Cell Function in Youth with New-Onset Type 1
1071 Diabetes. *New Engl J Med* **383**, 2007–2017 (2020).
1072 67. Dayan, C. M. *et al.* Preventing type 1 diabetes in childhood. *Science* **373**, 506–510 (2021).
1073 68. Waldron-Lynch, F. *et al.* Rationale and study design of the Adaptive study of IL-2 dose on
1074 regulatory T cells in type 1 diabetes (DILT1D): a non-randomised, open label, adaptive
1075 dose finding trial. *BMJ Open* **4**, (2014).
1076 69. Truman, L. A. *et al.* Protocol of the adaptive study of IL-2 dose frequency on regulatory T
1077 cells in type 1 diabetes (DILfrequency): a mechanistic, non-randomised, repeat dose,
1078 open-label, response-adaptive study. *BMJ Open* **5**, (2015).
1079 70. Langmead, B. & Salzberg, S. L. Fast gapped-read alignment with Bowtie 2. *Nat Methods*
1080 **9**, 357–359 (2012).
1081 71. Wolock, S. L., Lopez, R. & Klein, A. M. Scrublet: Computational Identification of Cell
1082 Doublets in Single-Cell Transcriptomic Data. *Cell Syst* **8**, 281-291.e9 (2019).
1083 72. Hao, Y. *et al.* Integrated analysis of multimodal single-cell data. *Cell* **184**, 3573-3587.e29
1084 (2021).
1085 73. Aitchison, J. *The Statistical Analysis of Compositional Data*. (Chapman & Hall, Ltd.,
1086 1986).
1087 74. McInnes, L., Healy, J. & Melville, J. UMAP: Uniform Manifold Approximation and
1088 Projection for Dimension Reduction. *ArXiv* **arXiv:1802**, (2018).
1089 75. Blondel, V. D., Guillaume, J.-L., Lambiotte, R. & Lefebvre, E. Fast unfolding of
1090 communities in large networks. *Journal of statistical mechanics: theory and experiment*
1091 **2008**, P10008 (2008).

1092 76. Itay, T. *et al.* Dissecting the multicellular ecosystem of metastatic melanoma by single-
1093 cell RNA-seq. *Science* **352**, 189–196 (2016).
1094 77. Pekalski, M. L. *et al.* Postthymic expansion in human CD4 naive T cells defined by
1095 expression of functional high-affinity IL-2 receptors. *J Immunol* **190**, 2554–2566 (2013).
1096 78. Love, M. I., Huber, W. & Anders, S. Moderated estimation of fold change and dispersion
1097 for RNA-seq data with DESeq2. *Genome Biol* **15**, 1–21 (2014).
1098 79. Zhu, A., Ibrahim, J. G. & Love, M. I. Heavy-tailed prior distributions for sequence count
1099 data: removing the noise and preserving large differences. *Bioinformatics* **35**, 2084–2092
1100 (2019).
1101 80. Street, K. *et al.* Slingshot: cell lineage and pseudotime inference for single-cell
1102 transcriptomics. *BMC Genomics* **19**, 477 (2018).
1103 81. van den Berge, K. *et al.* Trajectory-based differential expression analysis for single-cell
1104 sequencing data. *Nat Commun* **11**, 1201 (2020).
1105

1106 **Figures**

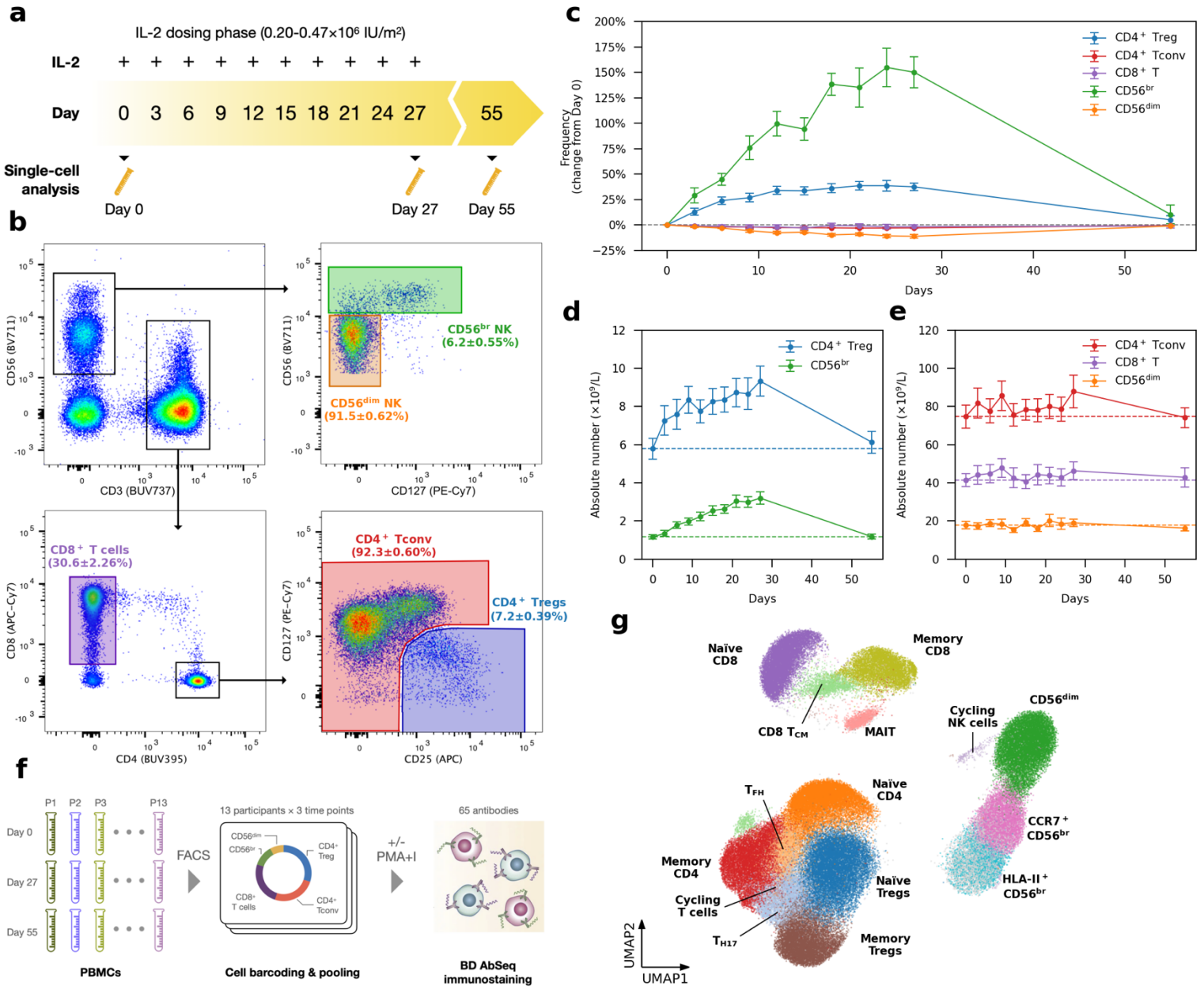

1108

1109 **Figure 1. Interval low-dose IL-2 administered every three days sustained an increased frequency**
1110 **of CD4^{+} regulatory T cells and CD56^{br} NK cells in blood.**

1111 **a**, Schematic representation of the interval low-dose IL-2 (iLD-IL-2) dosing regimen used in this study.
1112 **b**, Gating strategy for the delineation of the five T and NK cell populations assessed by flow cytometry.
1113 Values shown represent the average frequency of the respective immune cell population at baseline (Day
1114 0; ± standard error of mean, SEM) of the 18 DILfrequency participants. **c**, Variation (depicted as the %

1115 change from baseline pre-treatment levels) in the frequency of the five assessed immune subsets in blood
1116 (denominator is total T cells for T cell subsets, CD 4^+ T cells for the CD 4^+ Treg subset and total $CD56^+$
1117 NK cells for NK subsets). Data shown depict the average (± SEM) variation at each visit in the 18
1118 DILfrequency participants treated with the 3-day interval dosing schedule. **d-e**, Absolute numbers of the
1119 assessed $CD4^+$ $CD127^{low}CD25^{hi}$ (Tregs) and $CD56^{br}$ NK cell (**d**), as well as the broader $CD4^+$and $CD8^+$
1120 T and $CD56^+$ NK cell (**e**) subsets in blood. Data shown depict the average (± SEM) numbers at each visit
1121 in the 18 selected participants - treated with either 0.2 (N = 4), 0.32 (N = 12) or 0.47 (N = 2) × 10^6 IU/m^2
1122 IL-2. Dotted lines indicate the average baseline pre-treatment numbers of each immune subset. Plots
1123 depicting the changes of the immune populations shown in **c-e** in each of the individual study participants
1124 are shown in ref. [19]. **f**, Overview of the experimental design employed in this study. Simultaneous
1125 quantification of mRNA (N = 565 probes) and surface-expressed proteins (N = 65 AbSeq antibodies)
1126 was performed at the single-cell level using the BD Rhapsody system and employing a cell-enrichment
1127 strategy. Equal proportions of flow-sorted cells subsets (30% $CD4^+$ Tregs; 25% $CD4^+$ Tconv and $CD8^+$
1128 T; 12% $CD56^{br}$ NK and 8% $CD56^{dim}$ NK cells) from 13 selected DILfrequency participants treated with
1129 the 3-day dosing interval were profiled at three distinct time points: (i) prior to IL-2 treatment (Day 0),
1130 (ii) three days after the penultimate dose of IL-2 (Day 27), and (iii) one month after the last dose of IL-
1131 2 (Day 55). **g**, Uniform Manifold Approximation and Projection (UMAP) plot depicting the 15 clusters
1132 identified from the clustering of the 482,531 unstimulated cells profiled in this study. Clusters were
1133 manually annotated based on the expression of key differentially expressed mRNA and protein markers.
1134 Light grey cells correspond to $CD56^{br}$ NK cells without sorting gate information.

1135

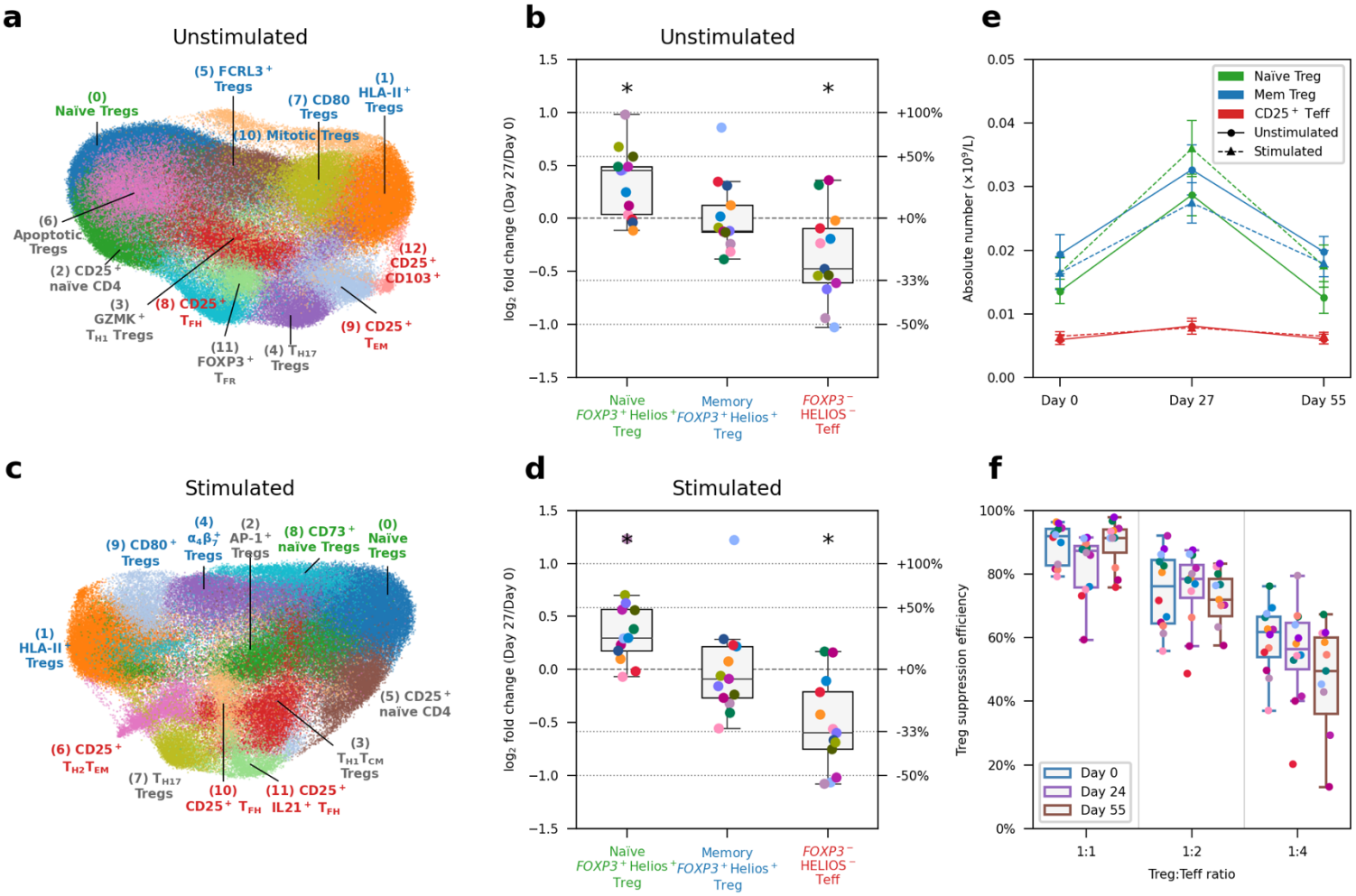

1137

1138 **Figure 2. Interval low-dose IL-2 immunotherapy selectively expands FOXP3^{+}HELIOS^{+} Tregs.**

1139 **a**, UMAP plot depicting the 13 clusters identified from the clustering of the 149,202 unstimulated cells
1140 sorted from the CD127^{low}CD25^{hi} Treg gate profiled in this study. Clusters were manually annotated
1141 based on the expression of key differentially expressed mRNA and protein markers. Clusters
1142 corresponding to: (i) naïve Tregs (defined as CD45RA^{+} FOXP3^{+}HELIOS^{+}); (ii) memory Tregs (defined
1143 as CD45RA^{-} FOXP3^{+}HELIOS^{+}); or (iii) CD25^{+} FOXP3^{-}HELIOS^{-} Teffs (defined as CD45RA^{-} FOXP3^{-}
1144 HELIOS^{-}) are annotated in green, blue and red, respectively. All other miscellaneous clusters not
1145 conforming to this definition are annotated in black. **b**, Relative frequency changes of naïve
1146 FOXP3^{+}HELIOS^{+} Tregs, memory FOXP3^{+}HELIOS^{+} Tregs, and CD25^{+} FOXP3^{-}HELIOS^{-} Teffs
1147 clusters on Day 27 compared to the baseline pre-treatment (Day 0) levels, for unstimulated cells. Relative
1148 frequency of a certain cluster was calculated as the number of cells in that cluster divided by the total

1149 number of cells sorted from the Treg gate. **c**,**d** Corresponding UMAP plot (**c**) and relative frequency for
1150 the identified subsets (**d**) for the 115,153 *in vitro* stimulated $CD4^{+}$ T cells sorted from the
1151 $CD127^{low}CD25^{hi}$ Treg gate. **e**, Absolute cell numbers of naïve $FOXP3^{+}HELIOS^{+}$ Tregs, memory
1152 $FOXP3^{+}HELIOS^{+}$ Tregs, and $CD25^{+}$ $FOXP3^{-}HELIOS^{-}$ Teffs on Day 0, Day 27 and Day 35, for
1153 unstimulated (circles connected by solid lines) and stimulated (triangles connected by dashed lines) cells.
1154 Absolute cell numbers were calculated as the total absolute number of Tregs measured by FACS
1155 multiplied by the relative frequency of a certain cluster. **f**, Per-cell Treg suppression efficiency for each
1156 time point. Treg suppression efficiency was assessed *in vitro* by culturing $CD4^{+}CD25^{hi}CD127^{low}$ Tregs
1157 with autologous $CD4^{+}CD25^{-/low}CD127^{+}$ Teffs at various ratios (x axis) and represented as the decrease
1158 in Teff proliferation compared with the control condition (y axis). PBMCs from 12 participants sampled
1159 on Day 0, Day 24 and Day 55 were used for this assay. *FDR-adjusted $P < 0.05$; two-sided Wilcoxon
1160 signed-rank test comparing the relative frequency of the subsets between Day 27 and Day 0. In **b**, **d** and
1161 **f**, each dot represents cells from a single participant. Dots with the same colour represent the same
1162 participant.

1163

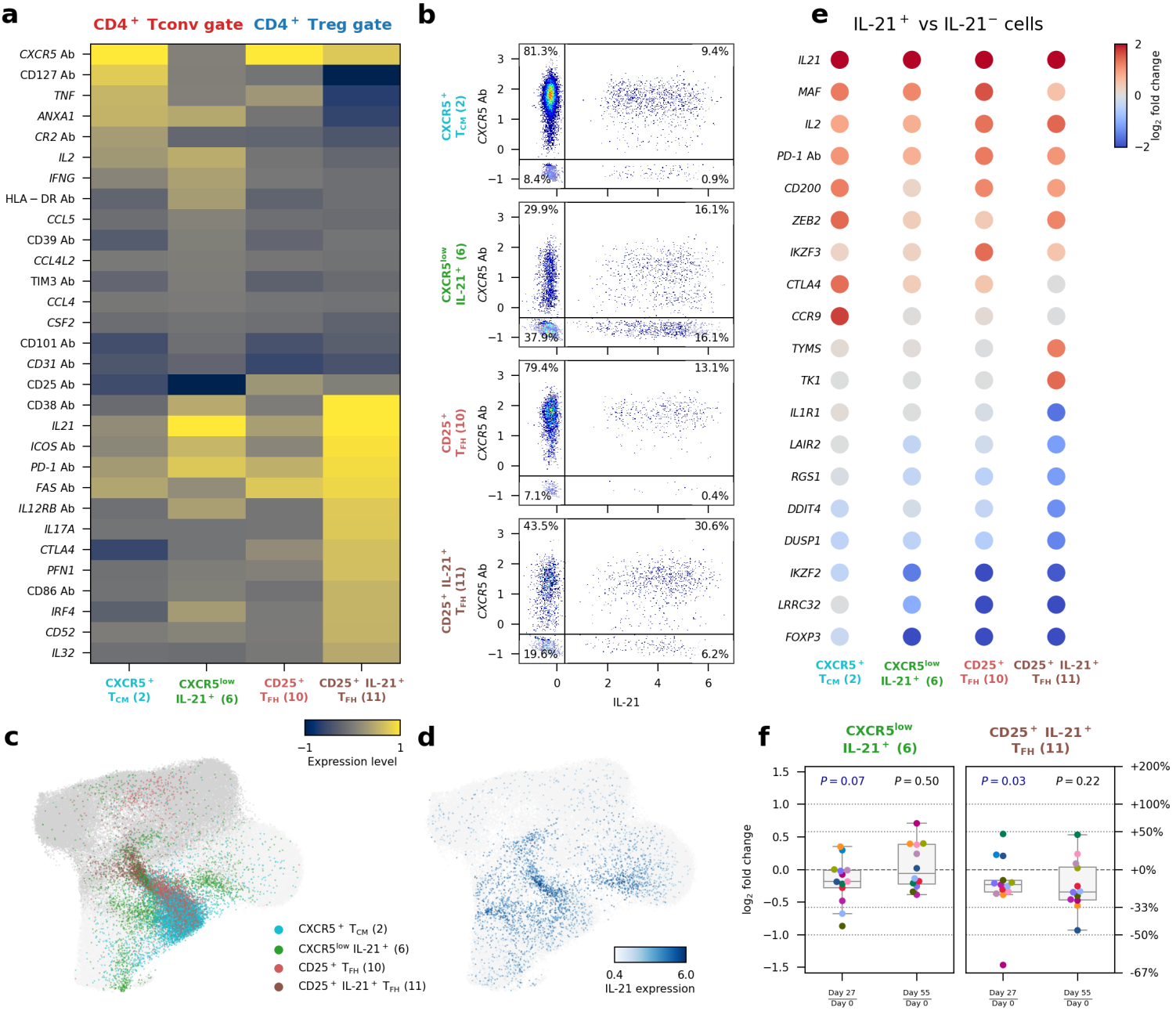

1165

1166 **Figure 3. Low-dose IL-2 treatment inhibits the differentiation of IL-21-producing CD4$^+$ T cells**

1167 **a,** Expression levels of 30 differentially expressed markers in the four assessed IL-21-producing CD4$^+$
1168 T cell subsets from *in vitro* stimulated CD4$^+$ T cells: CXCR5$^+$ T_{CM} and CXCR5^{low}IL-21$^+$ sorted from
1169 the CD25$^{-/low}$ Tconv gate; and CD25$^+$ T_{FH} and CD25$^+$IL-21$^+$ T_{FH} sorted from the CD127^{low}CD25^{hi} Treg
1170 gate. Expression levels are based on normalised and scaled single-cell expression data. Gene markers

1171 were selected based on pairwise differential expression analysis among the four assessed clusters. **b**,
1172 Expression of CXCR5 (AbSeq) and *IL21* in the four assessed IL-21^{+} CD4^{+} T cell subsets from *in vitro*
1173 stimulated cells. **c**, UMAP plot depicting the clustering of *in vitro* stimulated CD4^{+} T cells (N = 209,543
1174 cells). Cells are coloured according to the respective IL-21^{+} cluster assignment. Dark grey and light grey
1175 denote cells sorted from the CD127^{low}CD25^{hi} Treg gate and CD25$^{-/low}$ Tconv gate, respectively, that are
1176 not in IL-21^{+} clusters (**c**); or by normalised and scaled IL-21 expression levels (**d**). **e**, Gene expression
1177 changes between IL-21^{+} and IL-21^{-} cells within each of the four assessed IL-21^{+} CD4^{+} T cell clusters.
1178 Fold change values were calculated from pseudo-bulk expression data. Genes with absolute $\log_2$ fold
1179 change values equal to or greater than 1.2 and FDR-adjusted *P* values less than 0.01 in at least one cluster
1180 were selected. **f**, Relative frequency changes of IL-21^{+} cells within the two CD4^{+} T cell subsets
1181 displaying higher expression levels of IL-21: the CXCR5^{low}IL-21^{+} subset (left panel) and the CD25^{+}IL-
1182 21^{+} T_{FH} subset (right panel), comparing Day 27 and Day 55 with Day 0, respectively. Each dot represents
1183 cells from a single participant. Dots with the same colour represent the same participant. *P* values were
1184 calculated by comparing the relative frequency values between the two time points using a two-sided
1185 Wilcoxon signed-rank test.

1186

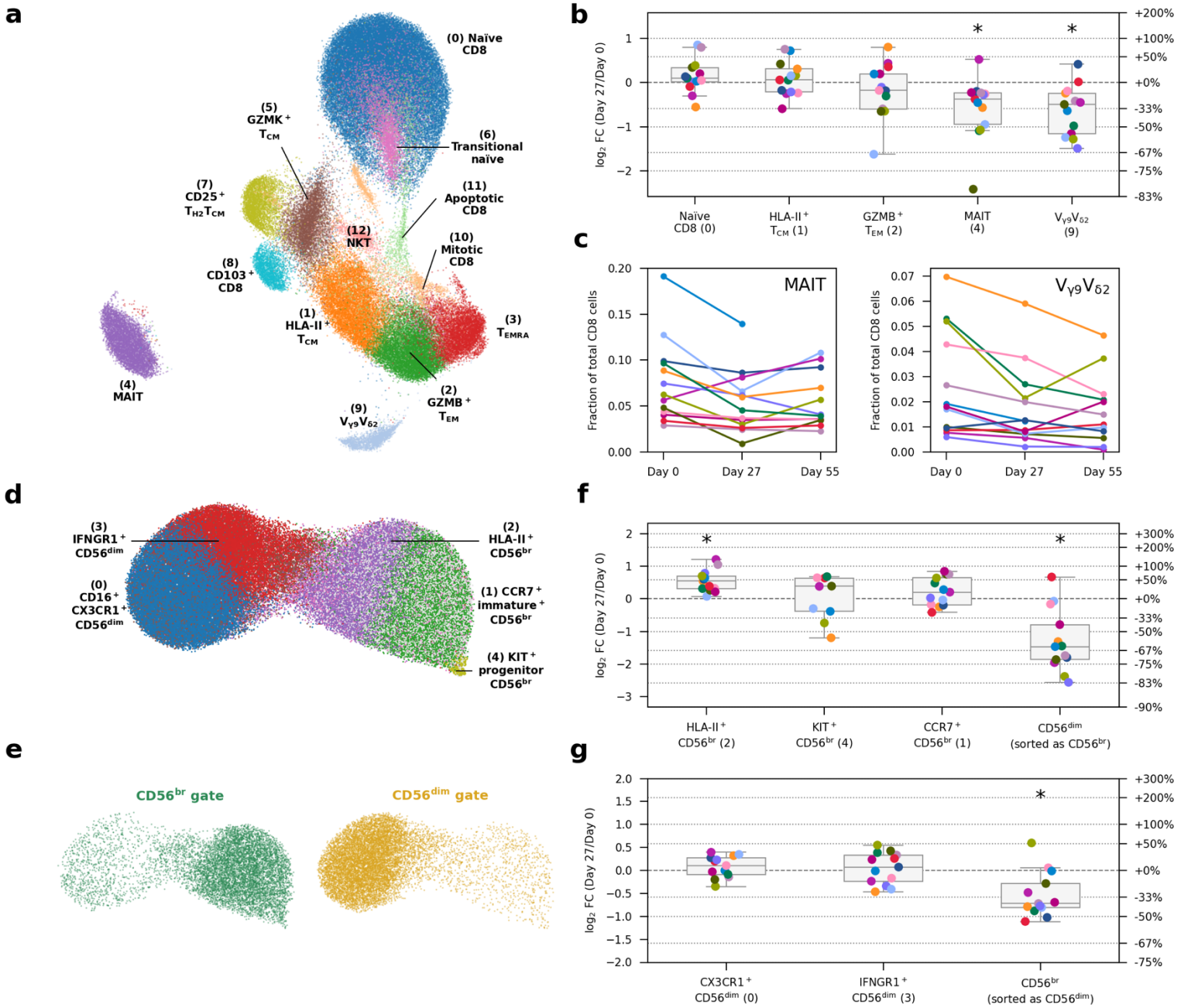

Figure 4. IL-2 treatment reduces the frequency of innate-like CD8$^+$ MAIT and V$_{\gamma9}$V$_{\delta2}$ T cells in circulation and selectively expands the IL-2 sensitive CD56^{br} NK cell subset.

a, UMAP plot depicting the clustering of the 93,379 unstimulated CD8$^+$ T cells profiled in this study. Clusters were manually annotated based on the expression of key differentially expressed mRNA and protein markers. **b**, Relative frequency changes of five selected CD8$^+$ T cell clusters on Day 27 compared

1194 to the baseline pre-treatment (Day 0) levels, for unstimulated cells. **c**, Relative frequency of the innate-
1195 like mucosal-associated invariant T cell (MAIT; left panel) and $V_{\gamma 9}V_{\delta 2}$ T cell (right panel) clusters on
1196 Day 0, Day 27, and Day 55. Each line represents cells from a participant. Lines with the same colour
1197 represent the same participant. **d**, UMAP plot depicting the clustering of the 118,625 unstimulated NK
1198 cells profiled in this study. Clusters were manually annotated based on the expression of key
1199 differentially expressed mRNA and protein markers. **e**, UMAP plot as in **d**, split and coloured by FACS
1200 sorting gates of origin. **f-g**, Relative frequency changes of five selected $CD56^{br}$ (**f**) or $CD56^{dim}$ (**g**) NK
1201 cell clusters on Day 27 compared to the baseline pre-treatment (Day 0) levels, for unstimulated cells.
1202 "$CD56^{dim}$ cells sorted as $CD56^{br}$" represents the fraction of cells sorted from the $CD56^{br}$ NK cell gate
1203 that are found in clusters that predominantly consists of $CD56^{dim}$ NK cells (ie. Clusters 0 and 3).
1204 Conversely, "$CD56^{br}$ cells sorted as $CD56^{dim}$" represents the fraction of cells sorted from the $CD56^{dim}$
1205 NK cell gate that are found in clusters that predominantly consists of $CD56^{br}$ NK cells (ie. Clusters 1, 2
1206 and 4). In **b**, **f**, and **g**, the relative frequency of a certain cluster is calculated as the number of cells in
1207 that cluster divided by the total number of cells sorted from the CD8 (**b**), $CD56^{br}$ (**f**) or $CD56^{dim}$ (**g**) NK
1208 cell gate. Each dot represents cells from a single participant. Dots with the same colour represent the
1209 same participant. Asterisks denote statistically significant differences (FDR-adjusted $P < 0.05$; two-sided
1210 Wilcoxon signed-rank test) in cell population frequencies between Day 27 and Day 0.

1211

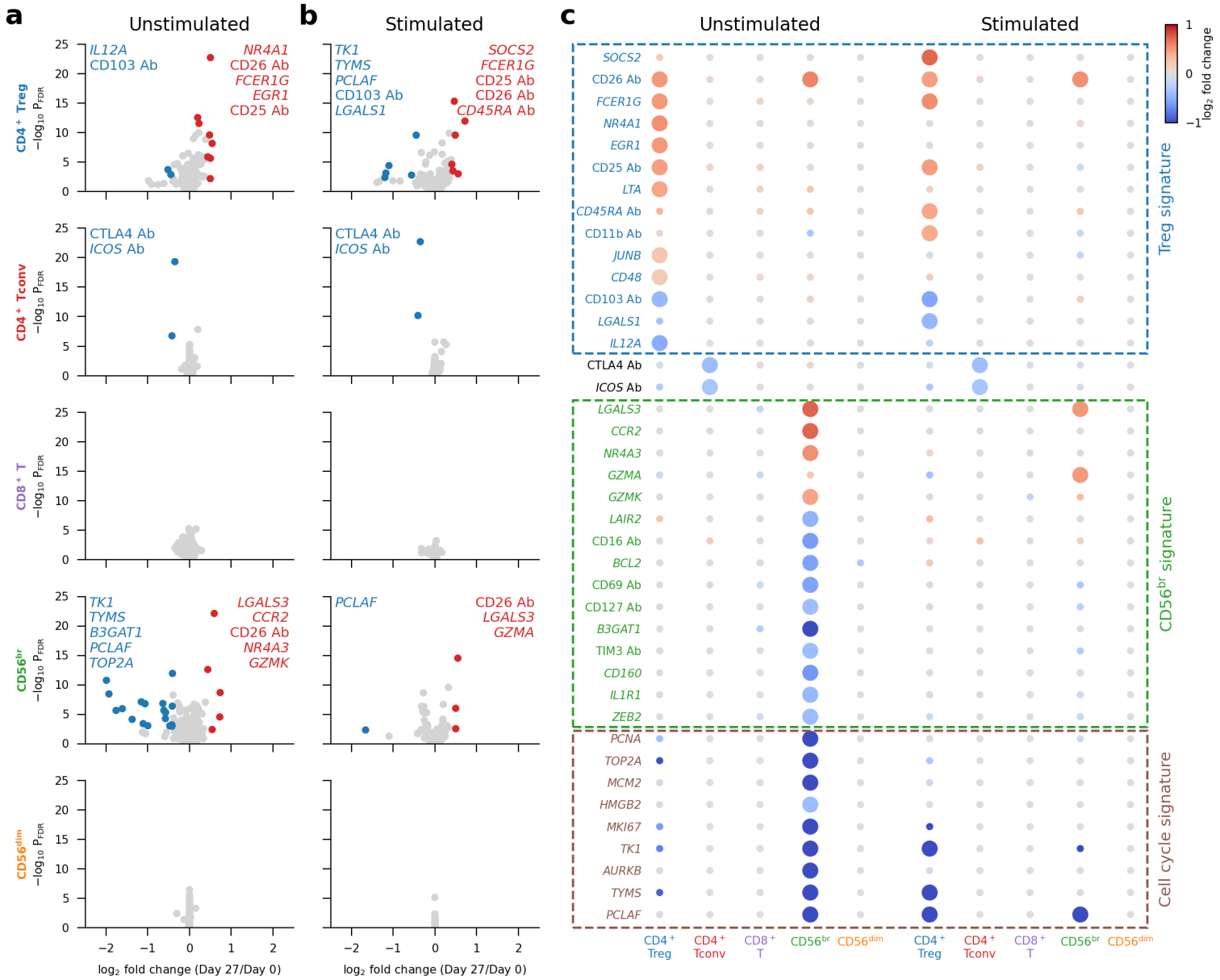

1213

1214 **Figure 5. IL-2 treatment selectively modulates gene expression of CD25^{hi} Tregs and CD56^{br} NK cells**
1215 **at Day 27.**

1216 **a-b**, Volcano plots depicting gene expression changes between Day 0 and Day 27 for the five assessed
1217 immune populations, for unstimulated (**a**) and stimulated (**b**) cells. Significantly differentially expressed
1218 genes are coloured in red (upregulated genes) or blue (downregulated genes). Names of the top five up- and
1219 downregulated genes as defined by fold change are labelled on each panel. **c**, Differential expression of
1220 Day 27 signature genes. Day 27 signature genes are defined as the 40 genes that are significantly

1221 differentially expressed in at least one cell population comparing Day 27 with Day 0. Dot colours represent
1222 $\log_2$ fold change between Day 0 and Day 27. Larger dots represent genes that are significantly differentially
1223 expressed in a certain cell population. Manually annotated signature gene subsets are labelled with dashed
1224 boxes.

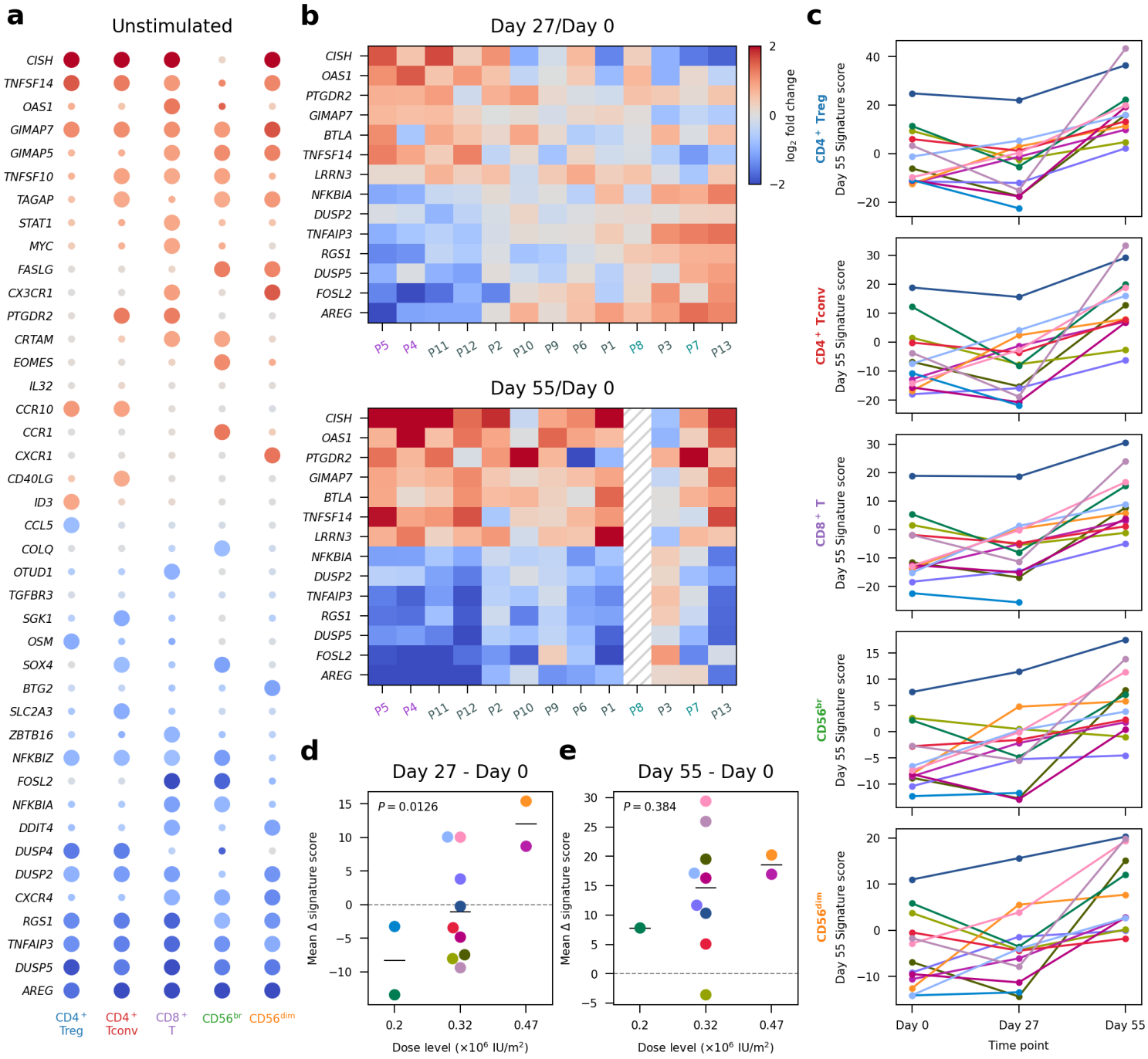

Figure 6. Interval low-dose IL-2 immunotherapy induces a long-lasting anti-inflammatory gene expression signature

a, Differential expression of Day 55 signature genes. Day 55 signature genes were defined as the 41 genes significantly differentially expressed in at least one cell population comparing Day 55 with Day

1231 0. Dot colours represent $\log_2$ fold-change between Day 0 and Day 55. Larger dots represent significantly
1232 differentially expressed genes. **b**, Participant-specific differential expression in $CD8^+$ T cells comparing
1233 Day 27 (top panel) or Day 55 (bottom panel) with Day 0. Top 5 up- and downregulated genes as defined
1234 by Day 55/Day 0 fold-change in $CD8^+$ T cells. Participant labels are coloured by their respective IL-2
1235 dose ($\times 10^6$ IU/m^2): 0.2 (cyan), 0.32 (gray), 0.47 (purple). **c**, Day 55 signature scores by participant for
1236 each time point and cell type. Each participant is represented by a different colour. *P* values were
1237 calculated using a two-tailed paired t test comparing Day 27 or Day 55 with Day 0, respectively. **d-e**,
1238 Variation in the mean expression scores of Day 55 signature genes across the five major cell types (mean
1239 Δ signature score) between Day 27 and Day 0 (**d**) and between Day 55 and Day 0 (**e**) for each participant.
1240 Participants were stratified by IL-2 dose. *P* values were calculated using linear regression. In d**-e**, average
1241 values of the Day 55 signature in all five cell types are shown for each participant.

1242

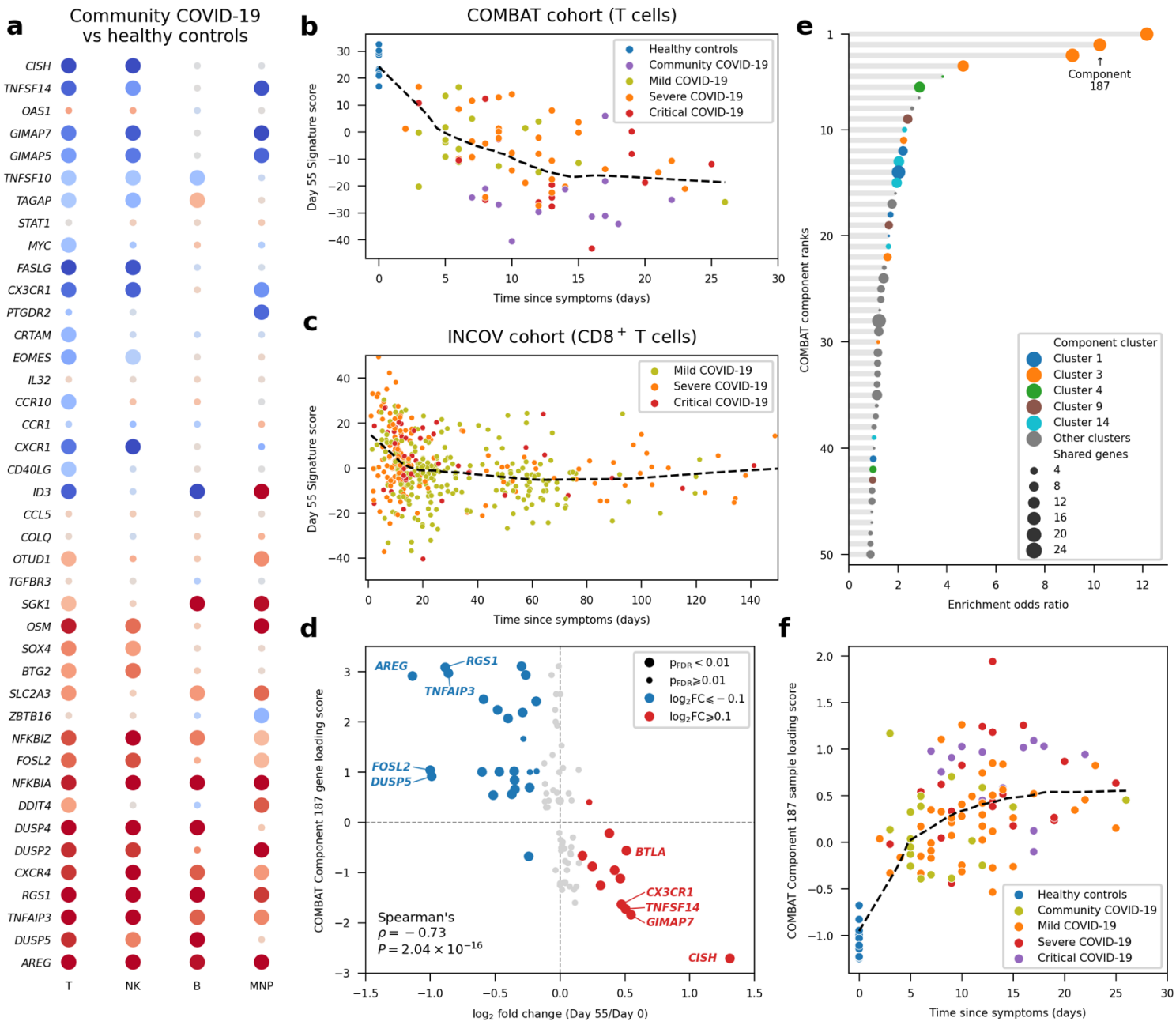

1244

1245 **Figure 7. The IL-2-induced Day 55 anti-inflammatory gene expression signature is reversed in**
1246 **COVID-19 patients**

1247 **a,** Differential expression of the 41 identified Day 55 signature genes in COVID-19 patients. Dot
1248 colours represent $\log_2$ fold-change between healthy controls and community COVID-19 patients
1249 from the COMBAT study[42]. Larger dots represent significantly differentially expressed genes in a

1250 certain cell population. **b-c** Day 55 gene signature scores plotted against the time since COVID-19
1251 symptoms in the COMBAT (**b**) and INCOV[43] (**c**) cohorts. The Day 55 gene signature score was
1252 based on expression levels of the 41 identified Day 55 signature genes. Each dot represents a pseudo-
1253 bulk sample from a certain participant and time point. Up to three longitudinal samples may
1254 originate from the same participant. COVID-19 patients were stratified according to their maximum
1255 disease severity. Dashed black lines represent smooth curves fitted by locally weighted scatterplot
1256 smoothing (LOWESS). **d**, Correlation between the differential expression of the Day 55 signature
1257 genes and Component 187 from the COMBAT study. Of the 1,419 genes included in Component
1258 187, a gene expression signature induced by COVID-19, 77 are also present in the target
1259 transcriptional panel used in this study. The effects of IL-2 immunotherapy and COVID-19 infection
1260 on the induction of these genes are compared by correlating Component loading score (y axis) with
1261 log2 fold change (Day 55/Day 0) in the CD8 population after IL-2 treatment (x axis). The positive
1262 and negative values in Component 187 loading scores represent the up- and downregulation of the
1263 corresponding gene, respectively, after COVID-19 infection. Larger dots represent genes with FDR-
1264 adjusted P values < 0.01, comparing Day 55 and Day 0 expression levels. **e**, Enrichment of Day 55
1265 signature genes in each gene expression component reported in the COMBAT study. Each dot
1266 represents a disease-associated gene expression component in the COMBAT study. Dot sizes
1267 represent the number of shared genes between a certain component and the 41 Day 55 signature
1268 genes. Only top 50 components ranked by their odds ratios of enrichment (x axis) are shown.
1269 Colours represent cluster membership as reported in the COMBAT study. Components in the same
1270 cluster are associated with diseases in a similar way. Cluster 3 is associated with all severity groups
1271 of COVID-19. **f**, Component 187 sample loading scores plotted against time since symptoms for
1272 COVID-19 patients. Each dot represents a patient. Patients are stratified by their maximum COVID-
1273 19 severity.

1274

1275 **Supplementary Figures**

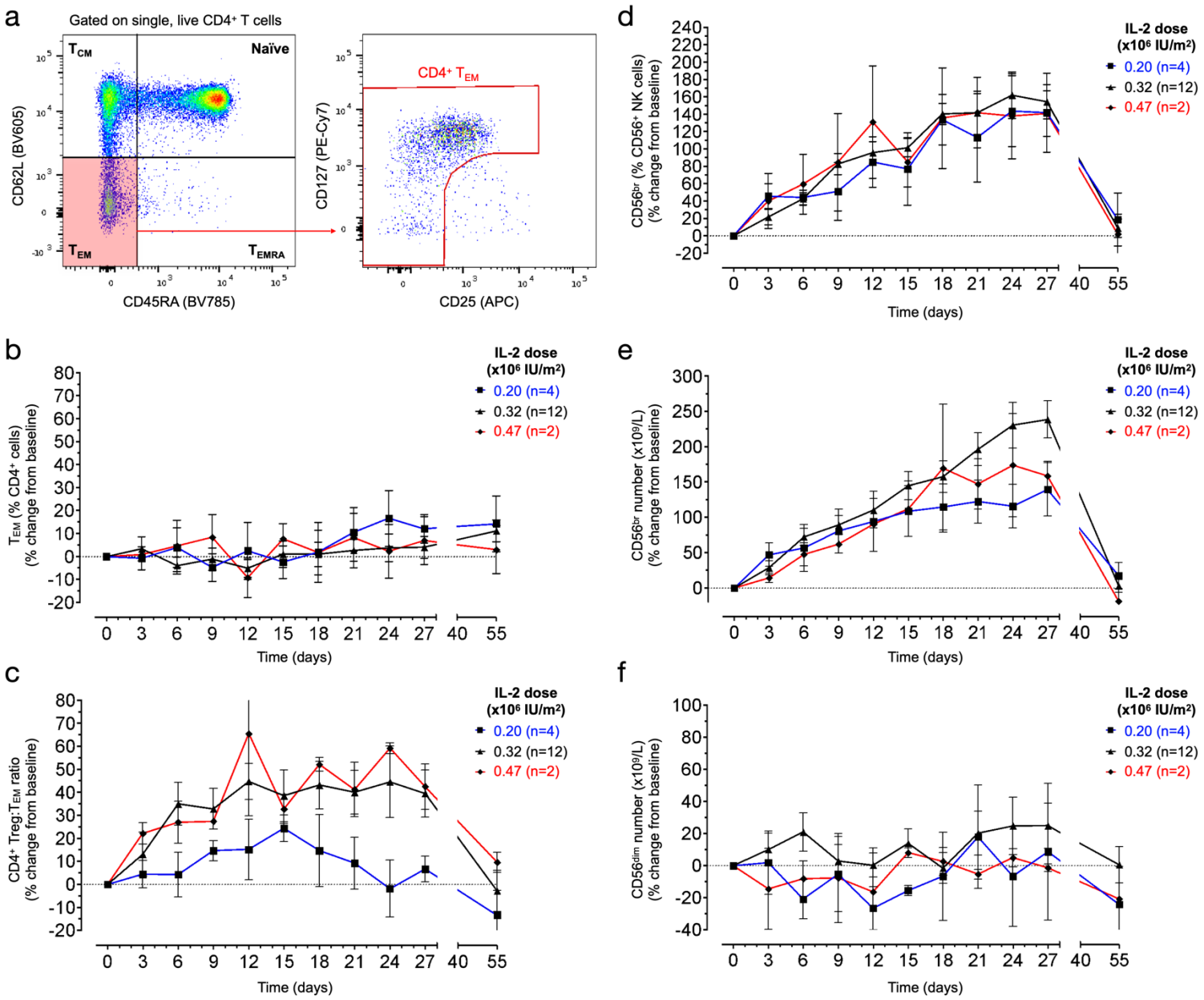

1277

1278 **Supplementary Figure 1. Flow cytometric characterisation of the effector memory CD4$^+$ T and**
1279 **CD56$^+$ NK cell populations.**

1280 **a,** Gating strategy for the delineation of CD4$^+$ effector memory T cells (T_{EM}). **b-c**, Variation (depicted as
1281 the % change from pre-treatment baseline levels) in the frequency of CD4$^+$ T_{EM} (**b**), or the ratio between
1282 CD4$^+$ Tregs and T_{EM} cells (**c**) during the course of the study. Baseline levels (mean +/- SEM): CD4$^+$ T_{EM}

1283 = 10.4% +/- 1.39; $CD4^+$ Treg:T_{EM} ratio = 0.76 +/- 0.07. **d-f,** Variation (depicted as the % change from
1284 pre-treatment baseline levels) in the relative frequency of $CD56^{br}$ NK cells within the total $CD3^-CD56^+$
1285 NK cell gate (**d**), and in the absolute number of $CD56^{br}$ (**e**) and $CD56^{dim}$ (**f**) NK cells in blood during the
1286 course of the study. Baseline levels (mean +/- SEM): $CD56^{br}$ = 6.2% +/- 0.55; $CD56^{br}$ Number ($x10^9$/L)
1287 = 0.011 +/- 0.001; $CD56^{dim}$ Number ($x10^9$/L) = 0.18 +/- 0.02. Frequencies of the assessed immune subsets
1288 were determined by flow cytometry in the 18 DILfrequency participants treated with the 3-day interval
1289 dosing schedule. Data shown depict the average (± SEM) variation of the assessed immune subsets at
1290 each visit and were stratified according to the IL-2 dose.

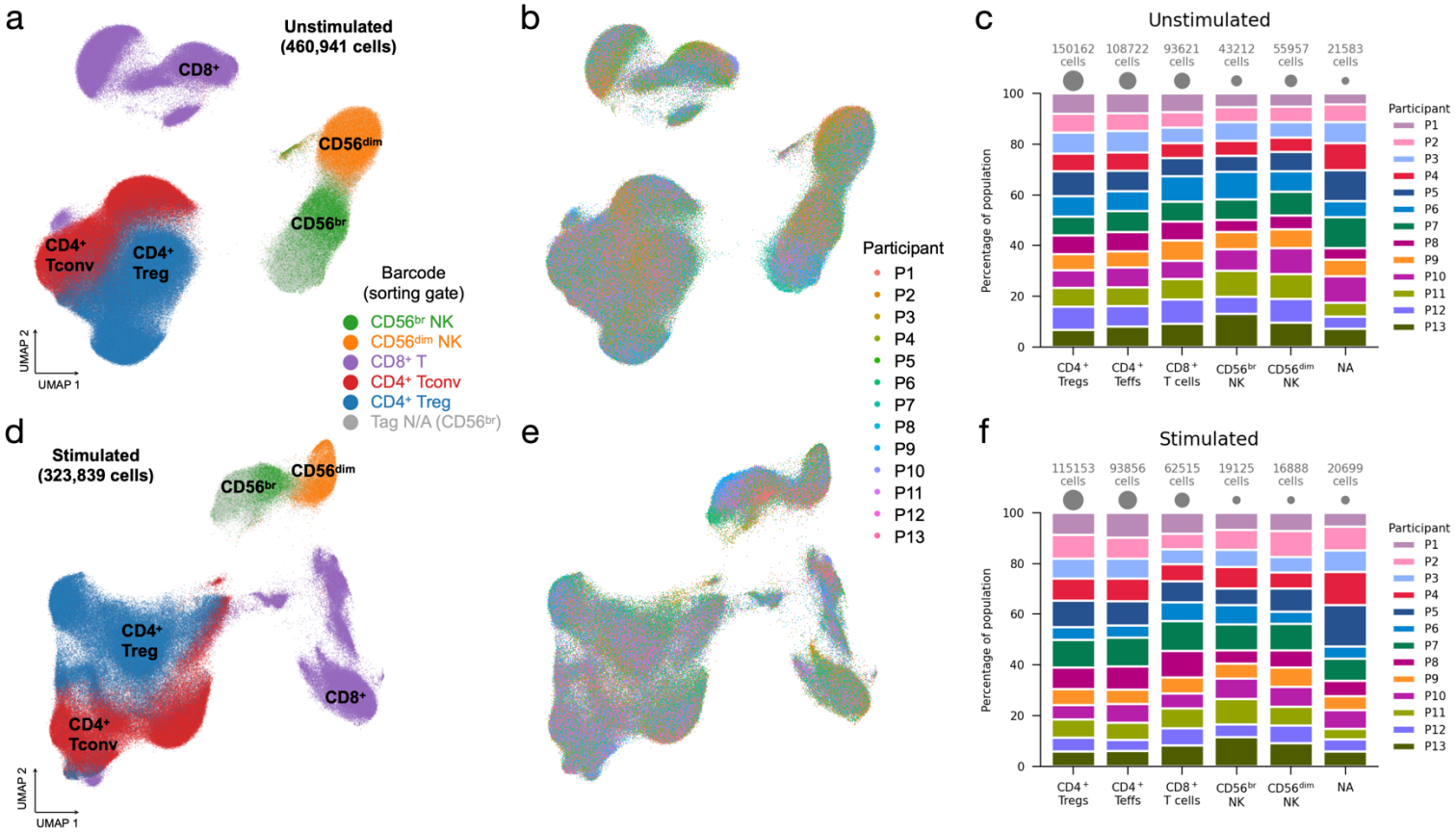

Supplementary Figure 2. Integration of the single-cell multiomics data.

a-b, Uniform Manifold Approximation and Projection (UMAP) plot depicting the clustering of the 460,941 unstimulated cells profiled in this study. Cells were coloured according to the corresponding oligo-conjugated barcode indicative of the respective FACS sorting gate (**a**), or according to the participant of origin (**b**). Untagged cells in **b** (labelled as 'Tag N/A') correspond to CD56^{br} NK cells, where we observed a suboptimal sample tagging efficiency, resulting in a significant fraction (37.2% in unstimulated cells) of CD56^{br} NK cells with missing sample barcode information. **c**, Relative proportion of cells from each individual participant in each of the flow-sorted unstimulated immune cell populations. Areas of grey circles represent total cell numbers in each immune cell population. **d-e**, UMAP plots depicting the clustering of the 323,839 cells profiled in this study following a short (90 min) *in vitro* stimulation with PMA + ionomycin. Cells were coloured according to the corresponding oligo-conjugated barcode indicative of the respective FACS sorting gate (**d**), or to the donor information (**e**). Untagged cells in panel a (labelled as 'Tag N/A') correspond to CD56^{br} NK cells, where we observed a suboptimal sample

1306 tagging efficiency resulting in a significant fraction (44.3% in the *in vitro* stimulated cells) of CD56^{br} NK
1307 cells with missing sample barcode information. **f**, Relative proportion of cells from each individual
1308 participant in each of the flow-sorted stimulated immune cell populations. Areas of grey circles represent
1309 total cell numbers in each immune cell population.

1310

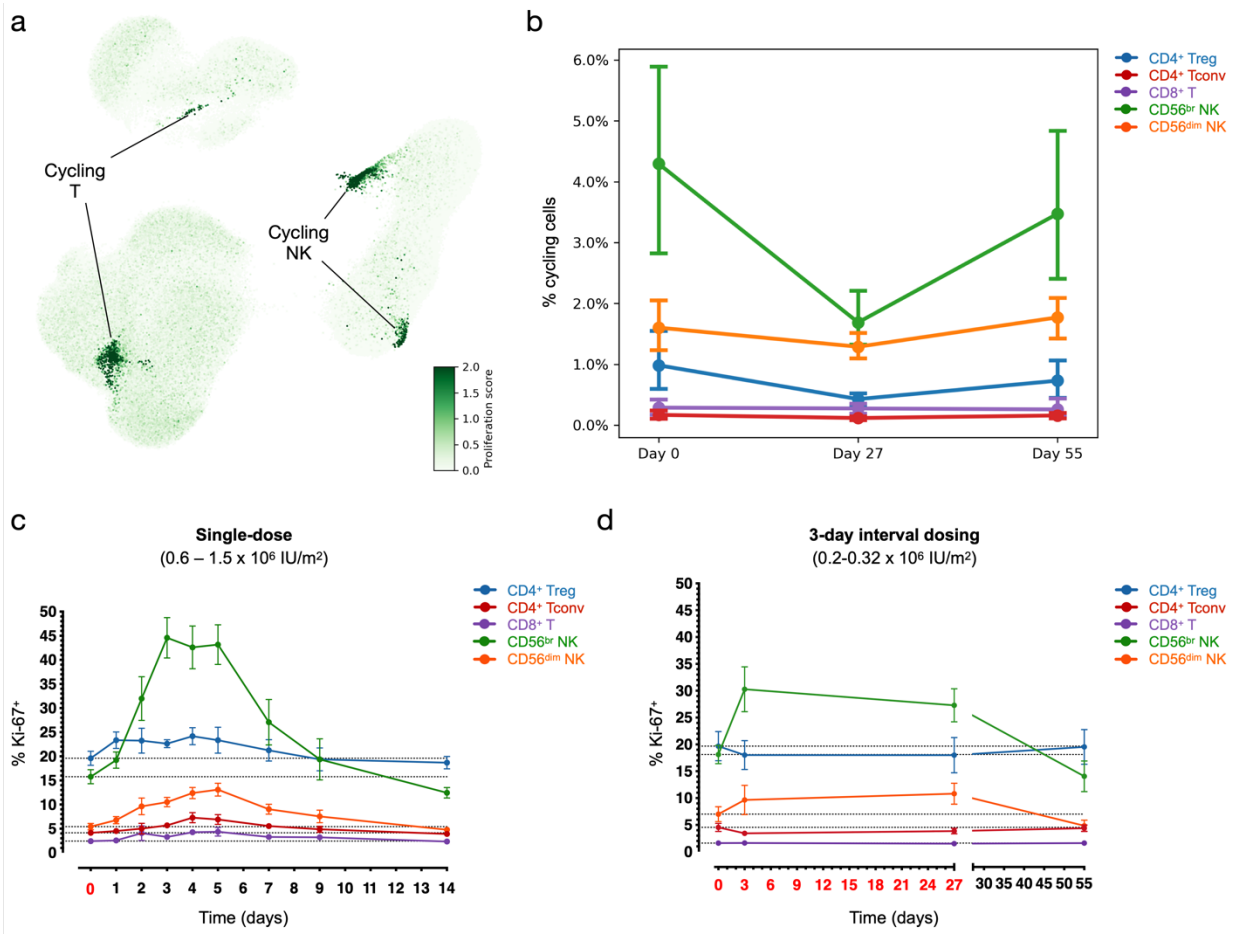

Supplementary Figure 3. Identification of proliferating cells.

a, UMAP plot depicting the expression of the cell-cycle signature score in each unstimulated single-cell, calculated by summarising the expression levels of 11 pre-selected genes related to cell cycle. **b**, Frequency of proliferating cells in each immune subset identified by the single-cell multiomics analysis. Proliferating cells were defined as the proportion of cells in the identified cycling clusters from each of the 5 sorted immune populations at Days 0, 27 and 55. **c-d**, Frequency of Ki-67^{+} cells within each of the 5 assessed immune populations in T1D patients treated with a single (DILT1D; **c**) or with the 3-day interval dosing schedule (DILfrequency; **d**). Ki-67 protein levels were assessed by intracellular flow cytometry in 6 patients from the DILT1D (treated with doses ranging from 0.6-1.5 x 10^6 IU/m^2) and five patients from the DILfrequency (treated with interval doses ranging from 0.2-0.32 x 10^6 IU/m^2). IL-2 dosing days are depicted in red in the x axis.

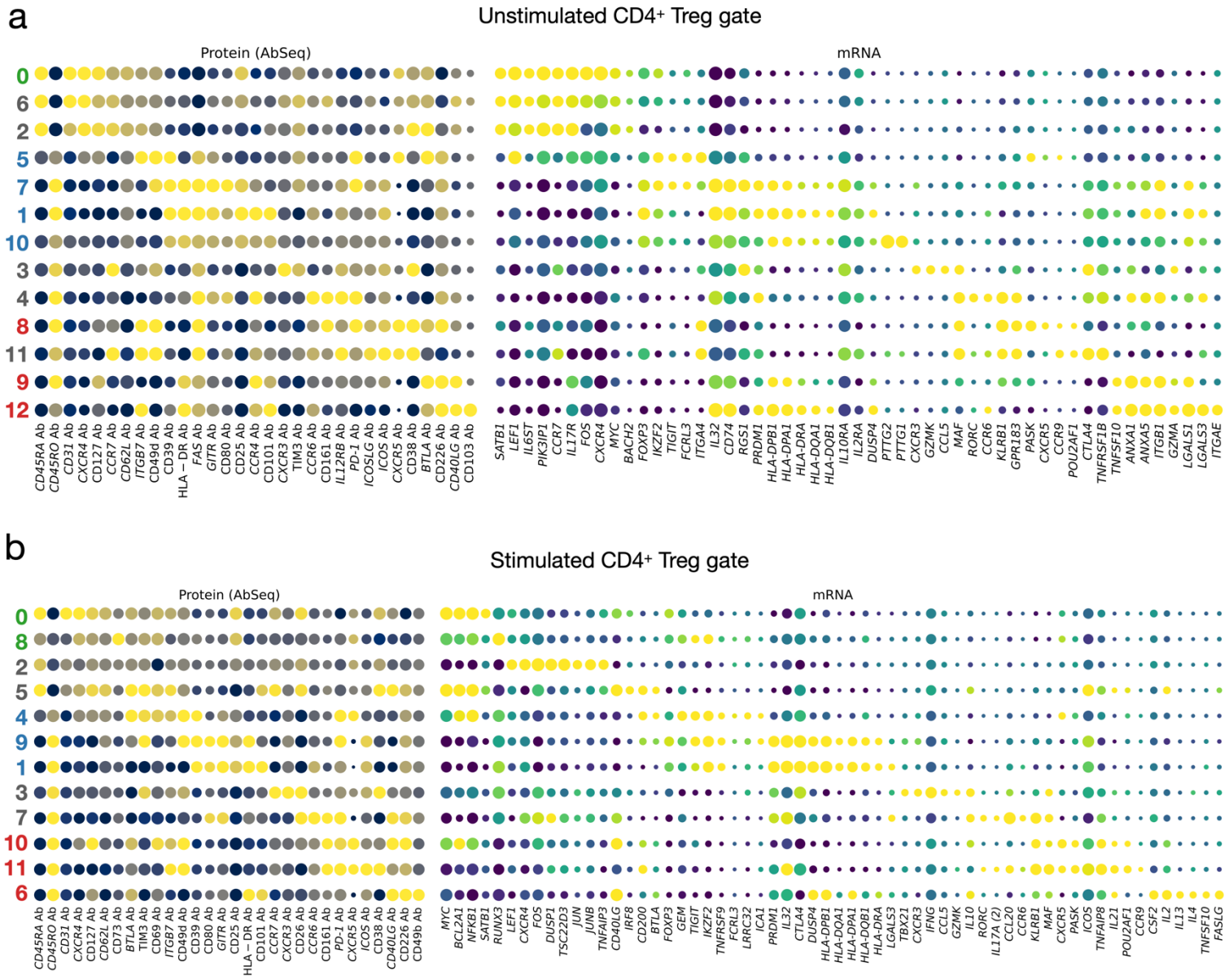

1325

1326 **Supplementary Figure 4. Functional annotation of the CD4^{+} CD127^{low}CD25^{hi} T cell subsets.**

1327 **a-b, E**xpression levels of selected differentially expressed markers delineating the functional subsets in
1328 the unstimulated (**a**) and *in vitro* stimulated (**b**) CD4^{+} T cells sorted from the CD127^{low}CD25^{hi} Treg gate.
1329 The size of the dots represents the frequency of the marker in the respective cluster and the colour
1330 brightness represents the relative expression level. Protein markers (AbSeq) are shown on the left section
1331 of the plots and mRNA markers on the right section. Clusters corresponding to: (i) naïve Tregs (defined
1332 as CD45RA^{+} FOXP3^{+}HELIOS^{+}); (ii) memory Tregs (defined as CD45RA^{-} FOXP3^{+}HELIOS^{+}); or (iii)

1333 $CD25^{+}$ $FOXP3^{-}HELIOS^{-}$Teffs (defined as $CD45RA^{-}$ $FOXP3^{-}HELIOS^{-}$) are annotated in green, blue
1334 and red, respectively. All other miscellaneous clusters not conforming to this definition are annotated in
1335 black.

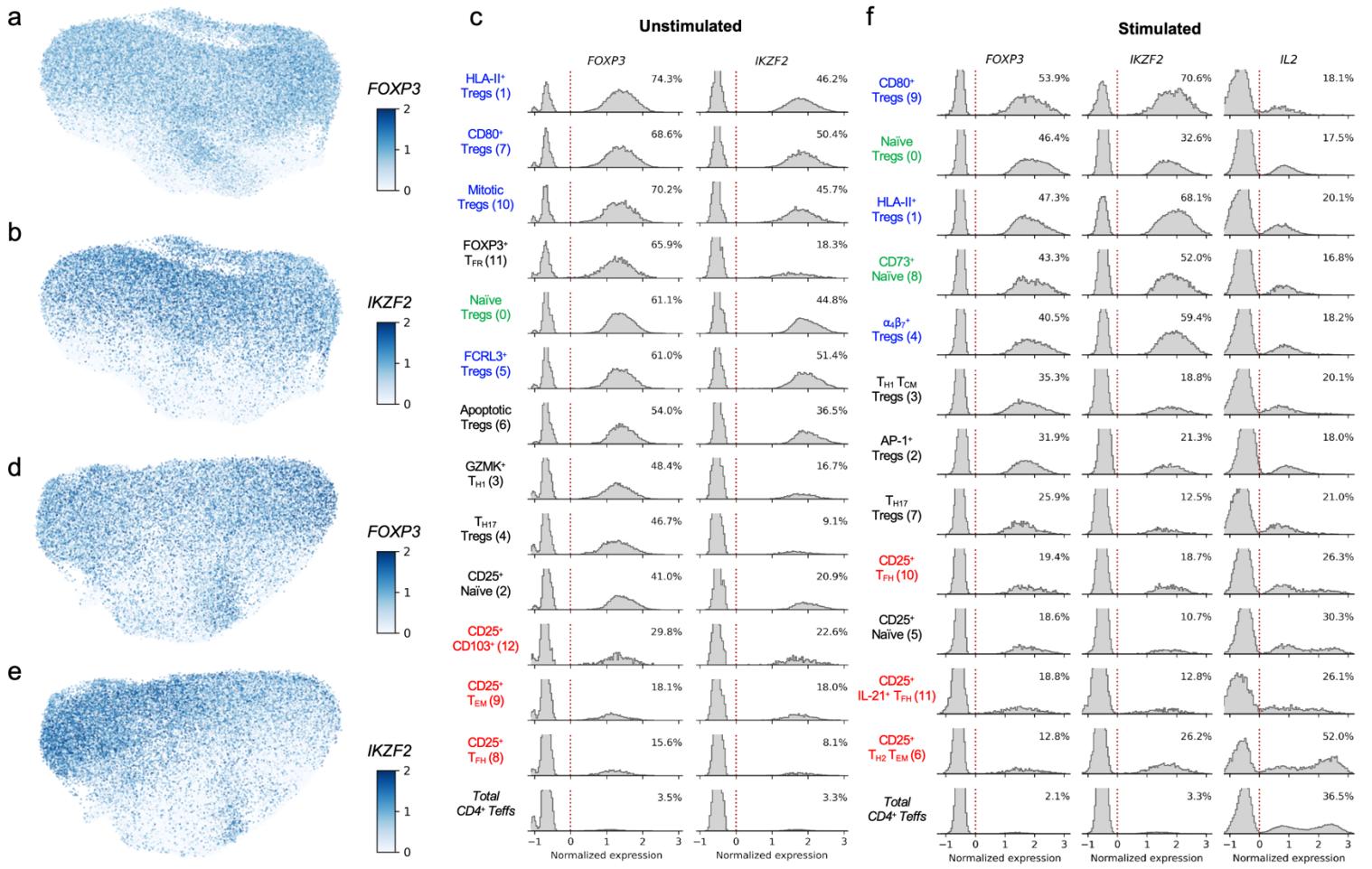

Supplementary Figure 5. Expression of *FOXP3*, *IKZF2* (HELIOS) and *IL2* differentiate functional CD4$^+$ Treg and CD4$^+$ Tconv subsets.

a-b, UMAP plots depicting the expression of the canonical Treg transcription factors *FOXP3* (**a**) and *IKZF2* (encoding HELIOS; **b**) in the unstimulated cells sorted from the CD4$^+$ CD127^{low}CD25^{hi} Treg gate. **c**, Distribution of expression levels of *FOXP3* and *IKZF2* in the identified unstimulated CD127^{low}CD25^{hi} CD4$^+$ T cell clusters. **d-e**, UMAP plots depicting the expression of the canonical Treg transcription factors *FOXP3* (**d**) and *IKZF2* (**e**) in the *in vitro* stimulated cells. **f**, Histograms depicting the expression of *FOXP3*, *IKZF2* and *IL2* in the identified *in vitro* stimulated clusters. Clusters corresponding to: (i) naïve Tregs (defined as CD45RA$^+$ FOXP3$^+$HELIOS$^+$); (ii) memory Tregs (defined as CD45RA$^-$ FOXP3$^+$HELIOS$^+$); or (iii) CD25$^+$ FOXP3$^-$HELIOS$^-$Teffs (defined as CD45RA$^-$ FOXP3$^-$ HELIOS$^-$) are annotated in green, blue and red, respectively. All other miscellaneous clusters not conforming to this definition are annotated in black.

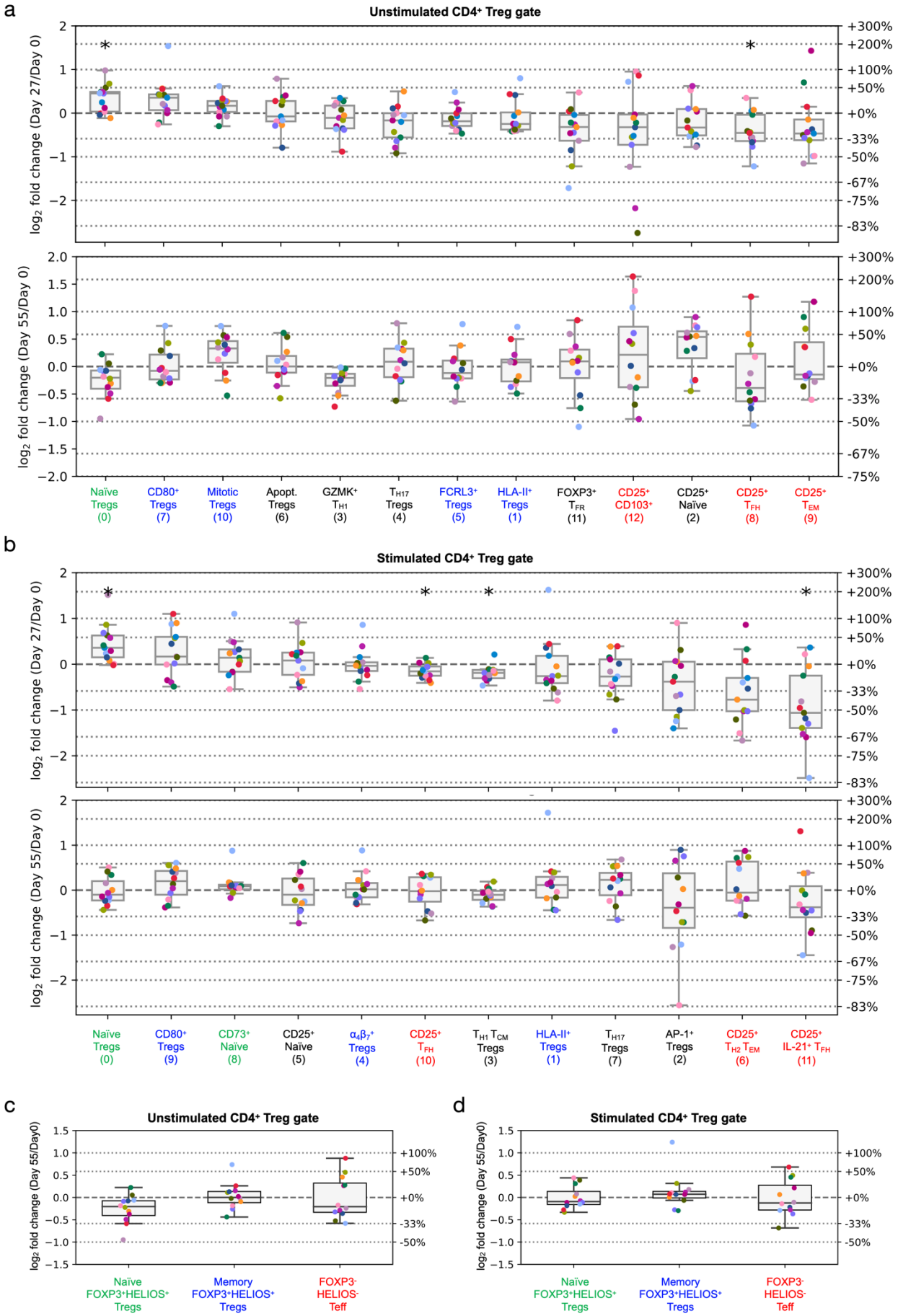
a
Unstimulated CD4+ Treg gate
log2 fold change (Day 27/Day 0)
log2 fold change (Day 55/Day 0)
+300%
+200%
+100%
+50%
+0%
-33%
-50%
-67%
-75%
-83%
Naïve Tregs (0)
CD80+ Tregs (7)
Mitotic Tregs (10)
Apopt. Tregs (6)
GZMK+ TH1 (3)
TH17 Tregs (4)
FCRL3+ Tregs (5)
HLA-II+ Tregs (1)
FOXP3+ TFR (11)
CD25+ CD103+ (12)
CD25+ Naïve (2)
CD25+ TFH (8)
CD25+ TEM (9)
b
Stimulated CD4+ Treg gate
Naïve Tregs (0)
CD80+ Tregs (9)
CD73+ Naïve (8)
CD25+ Naïve (5)
α4β7+ Tregs (4)
CD25+ TFH (10)
TH1 TCM Tregs (3)
HLA-II+ Tregs (1)
TH17 Tregs (7)
AP-1+ Tregs (2)
CD25+ TH2 TEM (6)
CD25+ IL-21+ TFH (11)
c
Unstimulated CD4+ Treg gate
Naïve FOXP3+HELIOS+ Tregs
Memory FOXP3+HELIOS+ Tregs
FOXP3- HELIOS- Teff
d
Stimulated CD4+ Treg gate
Naïve FOXP3+HELIOS+ Tregs
Memory FOXP3+HELIOS+ Tregs
FOXP3- HELIOS- Teff

1351 **Supplementary Figure 6. Differential abundance analysis reveals a transient increased frequency**
1352 **of FOXP3^{+}HELIOS^{+} Tregs following ld-IL2 treatment.**

1353 **a-b**, Relative frequency changes of all the identified unstimulated (**a**) or *in vitro* stimulated (**b**)
1354 CD127^{low}CD25^{hi} T cell clusters between Day 0 and Day 27 (top panels) or Day 55 (bottom panels).
1355 Clusters corresponding to: (i) naïve Tregs (defined as CD45RA^{+} FOXP3^{+}HELIOS^{+}), (ii) memory Tregs
1356 (defined as CD45RA^{-} FOXP3^{+}HELIOS^{+}), and (iii) CD25^{+} FOXP3^{-}HELIOS^{-}Teffs (defined as
1357 CD45RA^{-} FOXP3^{-}HELIOS^{-}) are annotated in green, blue and red, respectively. All other miscellaneous
1358 clusters not conforming to this definition are annotated in black. Asterisks denote statistically significant
1359 differences (two-sided Wilcoxon signed-rank test) in cell population frequencies between the two time
1360 points. **c-d**, Relative frequency changes of unstimulated (**c**) or *in vitro* stimulated (**d**) naïve
1361 FOXP3^{+}HELIOS^{+} Treg, memory FOXP3^{+}HELIOS^{+} Treg, and CD25^{+} FOXP3^{-}HELIOS^{-}Teff clusters in
1362 blood between Day 0 and Day 55. In **a-d**, each dot represents cells from a single participant. Dots with
1363 the same colour represent the same participant.

1364

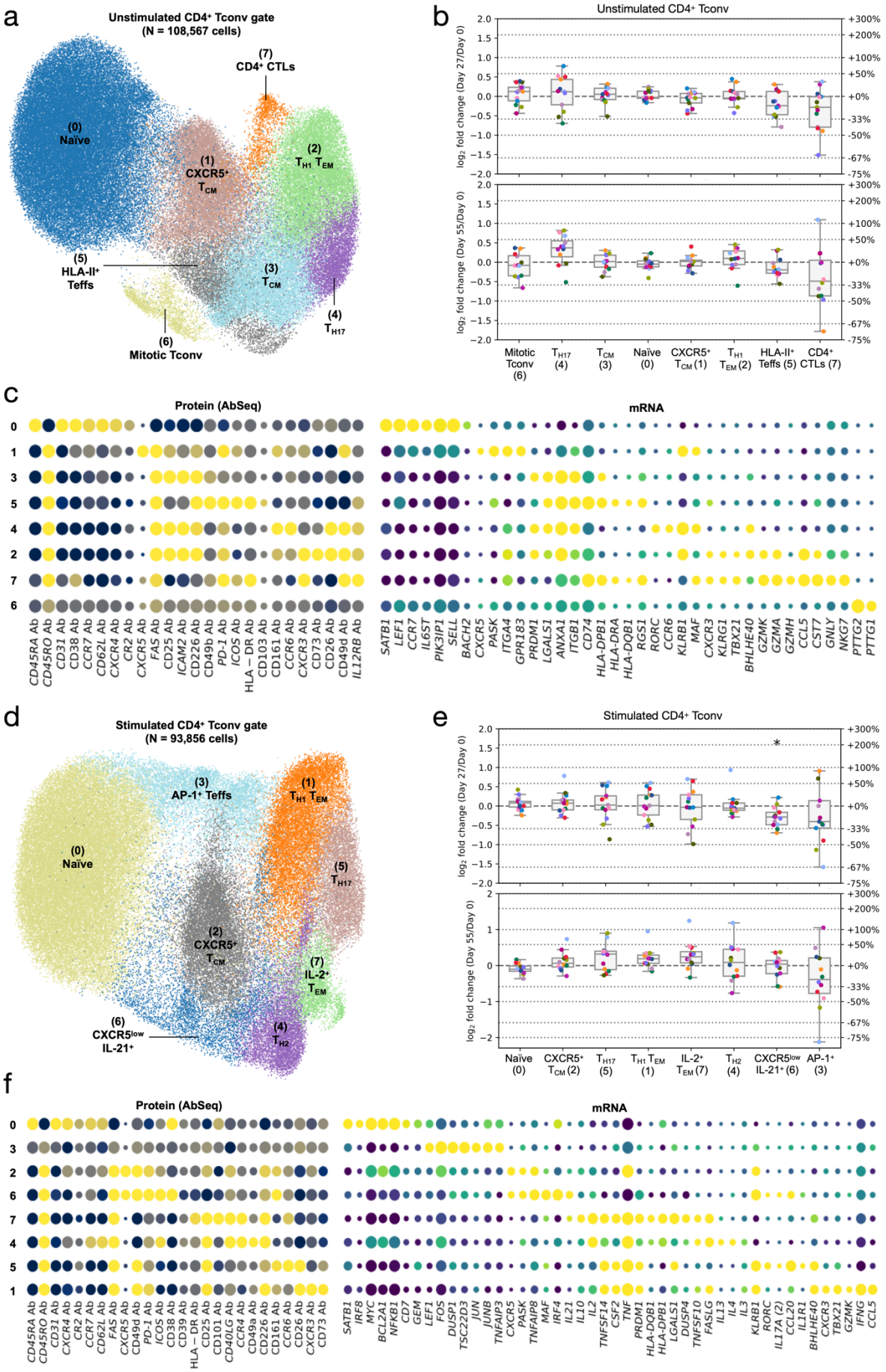
a
Unstimulated CD4+ Tconv gate
(N = 108,567 cells)
(0) Naïve
(1) CXCR5+ TCM
(2) TH1 TEM
(3) TCM
(4) TH17
(5) HLA-II+ Teffs
(6) Mitotic Tconv
(7) CD4+ CTLs
b
Unstimulated CD4+ Tconv
log2 fold change (Day 27/Day 0)
log2 fold change (Day 55/Day 0)
+300%
+200%
+100%
+50%
+0%
-33%
-50%
-67%
-75%
Mitotic Tconv (6)
TH17 (4)
TCM (3)
Naïve (0)
CXCR5+ TCM (1)
TH1 TEM (2)
HLA-II+ Teffs (5)
CD4+ CTLs (7)
c
Protein (AbSeq)
mRNA
CD45RA Ab
CD45RO Ab
CD31 Ab
CD38 Ab
CCR7 Ab
CD62L Ab
CXCR4 Ab
CR2 Ab
CXCR5 Ab
FAS Ab
CD25 Ab
ICAM2 Ab
CD226 Ab
CD49b Ab
PD-1 Ab
ICOS Ab
HLA – DR Ab
CD103 Ab
CD161 Ab
CCR6 Ab
CXCR3 Ab
CD73 Ab
CD26 Ab
CD49d Ab
IL12RB Ab
SATB1
LEF1
CCR7
IL6ST
PIK3IP1
SELL
BACH2
CXCR5
PASK
ITGA4
GPR183
PRDM1
LGALS1
ANXA1
ITGB1
CD74
HLA-DPB1
HLA-DRA
HLA-DQB1
RGS1
RORC
CCR6
KLRB1
MAF
CXCR3
KLRG1
TBX21
BHLHE40
GZMK
GZMA
GZMH
CCL5
CST7
GNLY
NKG7
PTTG2
PTTG1
d
Stimulated CD4+ Tconv gate
(N = 93,856 cells)
(0) Naïve
(1) TH1 TEM
(2) CXCR5+ TCM
(3) AP-1+ Teffs
(4) TH2
(5) TH17
(6) CXCR5low IL-21+
(7) IL-2+ TEM
e
Stimulated CD4+ Tconv
log2 fold change (Day 27/Day 0)
log2 fold change (Day 55/Day 0)
Naïve (0)
CXCR5+ TCM (2)
TH17 (5)
TH1 TEM (1)
IL-2+ TEM (7)
TH2 (4)
CXCR5low IL-21+ (6)
AP-1+ (3)
f
Protein (AbSeq)
mRNA
CD45RA Ab
CD45RO Ab
CD31 Ab
CXCR4 Ab
CR2 Ab
CCR7 Ab
CD62L Ab
FAS Ab
CXCR5 Ab
CD49d Ab
PD-1 Ab
ICOS Ab
CD38 Ab
CD39 Ab
HLA – DR Ab
CD25 Ab
CD101 Ab
CD40LG Ab
CCR4 Ab
CD49a Ab
CD226 Ab
CD161 Ab
CCR6 Ab
CD26 Ab
CXCR3 Ab
CD73 Ab
SATB1
IRF8
MYC
BCL2A1
NFKB1
CD7
GEM
LEF1
FOS
DUSP1
TSC22D3
JUN
JUNB
TNFAIP3
CXCR5
PASK
TNFAIP8
MAF
IRF4
IL21
IL10
IL2
TNFSF14
CSF2
TNF
PRDM1
HLA-DQB1
HLA-DPB1
LGALS1
DUSP4
TNFSF10
FASLG
IL13
IL4
IL3
KLRB1
RORC
IL17A (2)
CCL20
IL1R1
BHLHE40
CXCR3
TBX21
GZMK
IFNG
CCL5

1366 **Supplementary Figure 7. Analysis of circulating CD4^{+} CD25$^{-/low}$ conventional T cells**

1367 **a**, UMAP plot depicting the clustering of the 108,722 unstimulated CD4^{+} T cells sorted from the CD25^{-}
1368 $^{/low}$ Tconv gate profiled in this study. Clusters were manually annotated based on the expression of key
1369 differentially expressed mRNA and protein markers. **b**, Expression levels of selected differentially
1370 expressed markers delineating the functional subsets in the unstimulated CD4^{+} T cells sorted from the
1371 CD25$^{-/low}$ Tconv gate. The size of the dots represents the frequency of the marker in the respective cluster
1372 and the colour brightness represents the relative expression level. Protein markers (AbSeq) are shown
1373 on the left section of the plots and mRNA markers on the right section. **c,** Relative frequency changes of
1374 all identified unstimulated CD4^{+} CD25$^{-/low}$ Tconv clusters in blood at Day 27 (top panel) or Day 55
1375 (bottom panel) compared to the baseline pre-treatment (Day 0) levels. **d-f**, Plots corresponding to **a-c**,
1376 for the 93,856 *in vitro* stimulated CD4^{+} T cells sorted from the CD25$^{-/low}$ Tconv gate.
1377

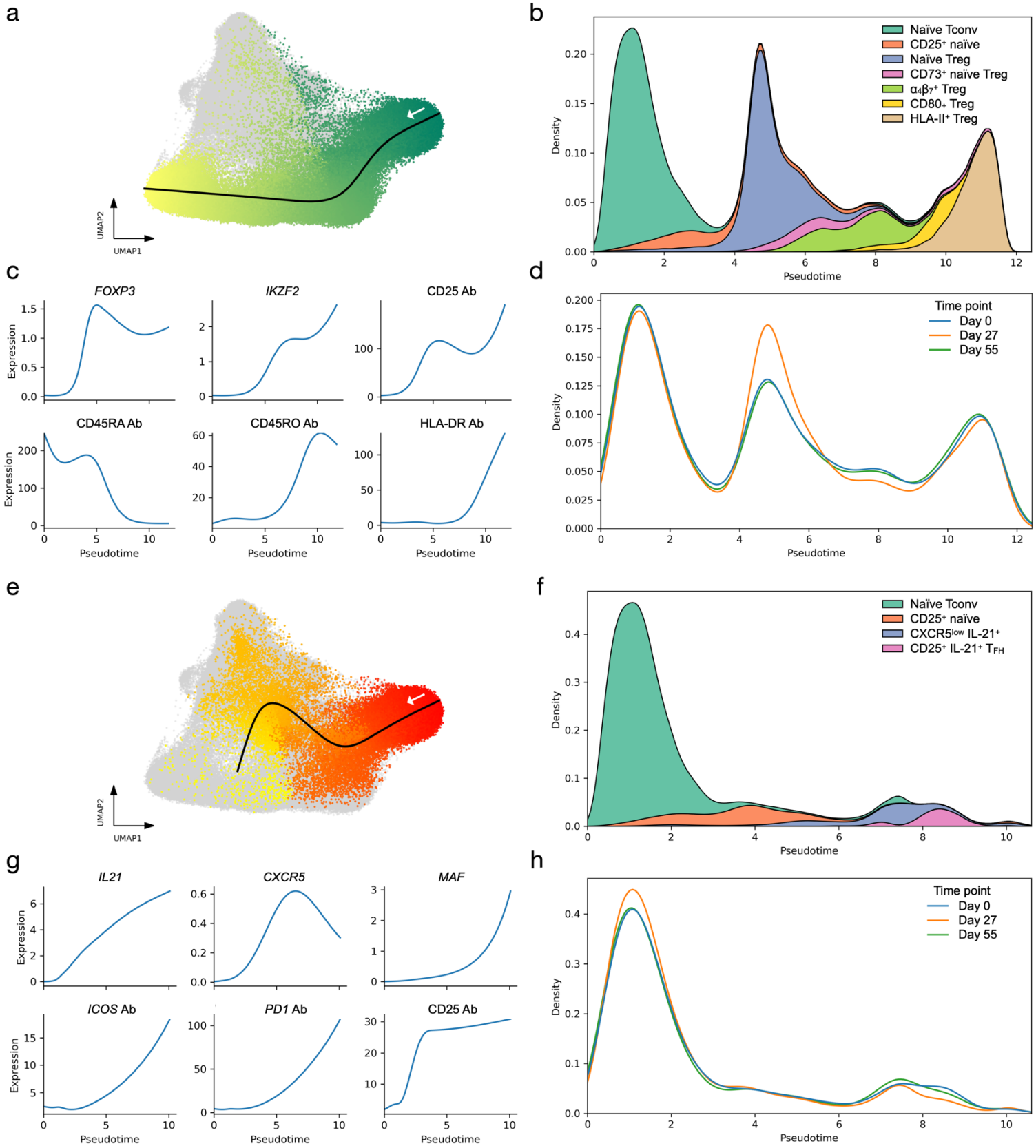
a
UMAP2
UMAP1
b
Naïve Tconv
CD25+ naïve
Naïve Treg
CD73+ naïve Treg
α4β7+ Treg
CD80+ Treg
HLA-II+ Treg
Density
Pseudotime
c
FOXP3
IKZF2
CD25 Ab
CD45RA Ab
CD45RO Ab
HLA-DR Ab
Expression
Pseudotime
d
Time point
Day 0
Day 27
Day 55
Density
Pseudotime
e
UMAP2
UMAP1
f
Naïve Tconv
CD25+ naïve
CXCR5low IL-21+
CD25+ IL-21+ TFH
Density
Pseudotime
g
IL21
CXCR5
MAF
ICOS Ab
PD1 Ab
CD25 Ab
Expression
Pseudotime
h
Time point
Day 0
Day 27
Day 55
Density
Pseudotime

1379

1380 **Supplementary Figure 8. Pseudo-time analysis reveals trajectories of Treg and T_{FH} differentiation**
1381 **in *in vitro* stimulated $CD4^+$ T cells.**

1382 **a**, UMAP plot depicting the Treg differentiation trajectory identified by Slingshot pseudo-time
1383 analysis. **b**, Pseudo-time distribution of cells associated with the Treg trajectory, stratified by cluster
1384 labels. **c**, Fitted expression curves of selected canonical Treg genes by pseudo-time. **d**, Pseudo-time
1385 distribution of cells associated with the Treg trajectory, stratified by time points. **e**, UMAP plot
1386 depicting the T_{FH} differentiation trajectory identified by Slingshot pseudo-time analysis. **f**, Pseudo-
1387 time distribution of cells associated with the T_{FH} trajectory, stratified by cluster labels. **g**, Fitted
1388 expression curves of selected canonical T_{FH} genes by pseudo-time. **h**, Pseudo-time distribution of
1389 cells associated with the T_{FH} trajectory, stratified by time points. Data from **a-h** were generated from
1390 in vitro stimulated $CD4^+$ T cells.
1391

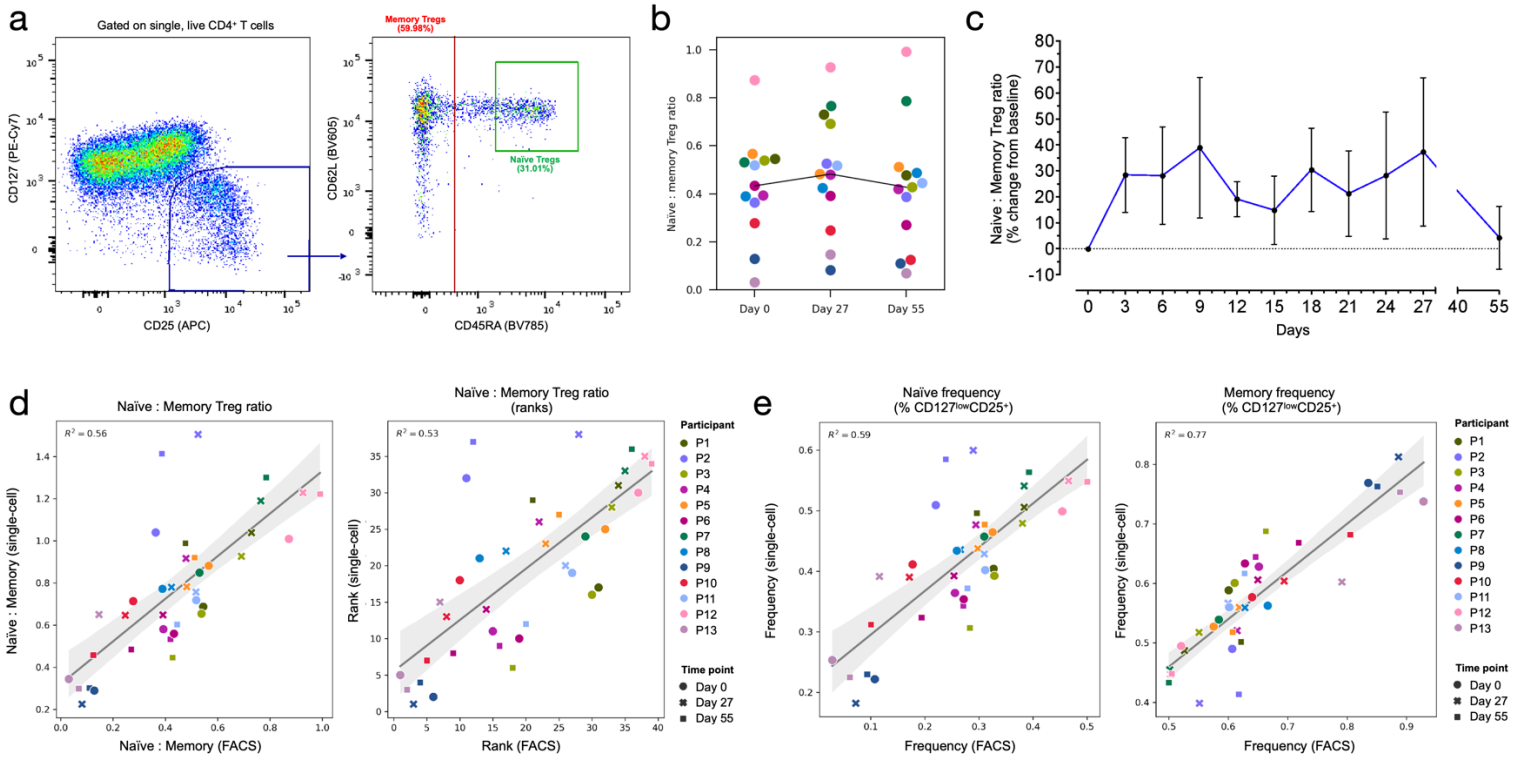

Supplementary Figure 9. Replication of the ratio of naïve:memory Tregs by FACS

a, Gating strategy for the delineation of the naïve ($CD45RA^{+}$) and memory ($CD45RA^{-}$) compartment by flow cytometry within cells sorted from the $CD4^{+}$ $CD127^{low}CD25^{hi}$ Treg gate. **b**, Ratio between naïve and memory cells within the $CD4^{+}$ $CD127^{low}CD25^{hi}$ Treg gate at the three assessed timepoints (Day 0, Day 27 and Day 55). The connecting line represents the median naïve:memory ratio in the 13 participants selected for single-cell analysis at each time point. **c**, Variation (depicted as the % change from baseline pre-treatment levels) in the naïve:memory ratio within the $CD4^{+}$ $CD127^{low}CD25^{hi}$ Treg gate assessed by flow cytometry. Data shown depict the average (±SEM) variation at each visit for the 13 participants selected for single-cell analysis. **d**, Correlation between the naïve:memory ratio within $CD4^{+}$ $CD127^{low}CD25^{hi}$ T cells (left panel), or the corresponding ranks (right panel), obtained from FACS data (x axis) and that estimated from single-cell sequencing data (y axis). **e**, Correlation between the frequency of naïve ($CD45RA^{+}$; left panel) and memory ($CD45RA^{-}$; right panel) cells within $CD127^{low}CD25^{hi}$ T cells obtained from FACS data (x axis) and that obtained from single-cell sequencing data (y axis). In **b**, **d** and **e**, each dot represents a sample, with colours and shapes representing participants and time points of origin, respectively. In **d-e**, linear regression lines are shown in black, and 95% confidence intervals of the regression estimate are shown in grey shades.

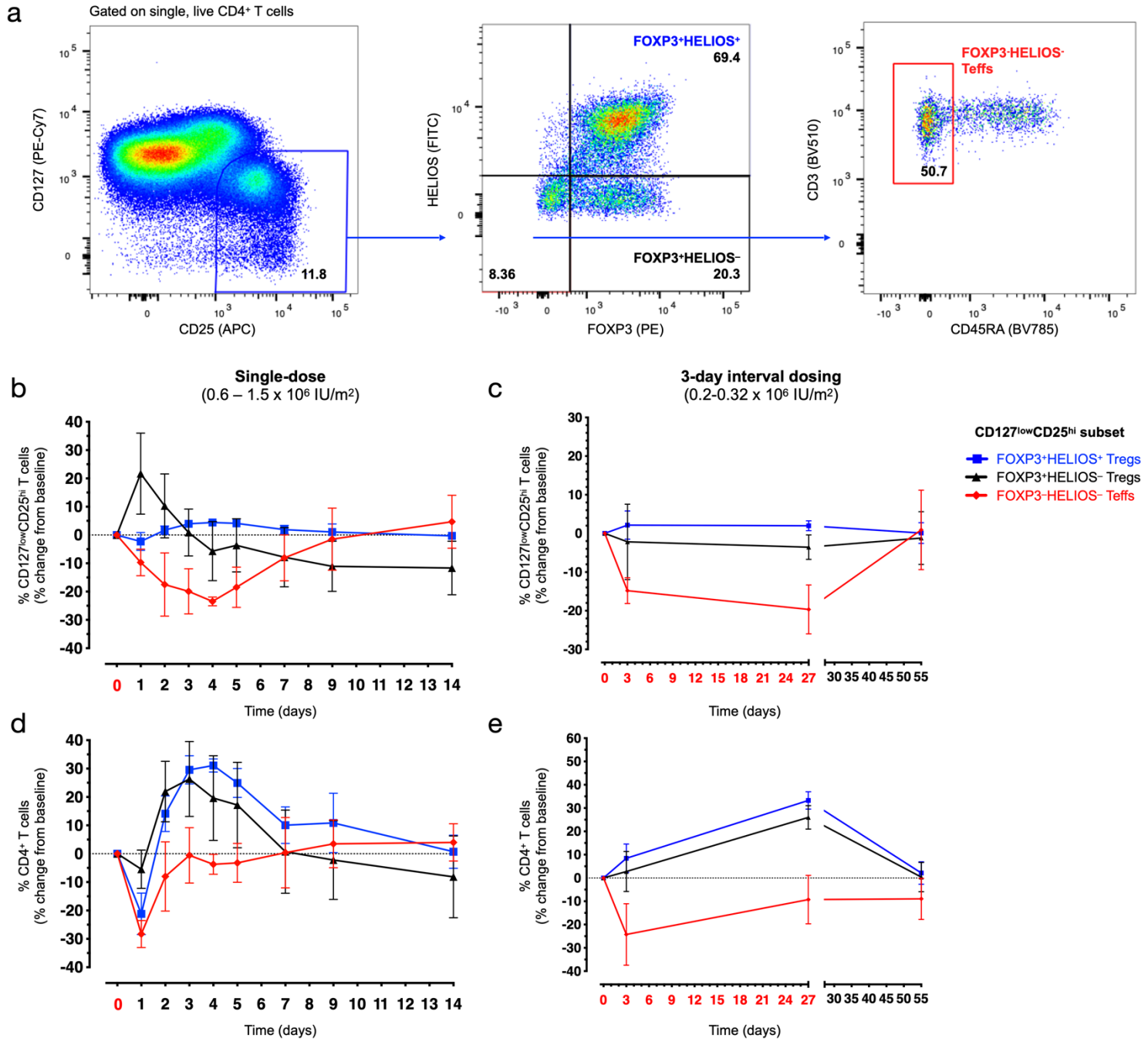

Supplementary Figure 10. Delineation of Treg subsets by FACS

a, Gating strategy for the delineation of the FOXP3^{+}HELIOS^{+} Treg, FOXP3^{+}HELIOS^{-} Treg and CD45RA^{-} FOXP3^{-}HELIOS^{-} Teff subsets by flow cytometry. **b-c** Variation (depicted as the % change from baseline pre-treatment levels) in the frequency of FOXP3^{+}HELIOS^{+} (blue), FOXP3^{+}HELIOS^{-} (black) and CD45RA^{-} FOXP3^{-}HELIOS^{-} (red) cells within the CD127^{low}CD25^{hi} gate in patients treated

1417 with a single dose (DILT1D; **b**) or with the 3-day interval dosing schedule (DILfrequency; **c**). Baseline
1418 levels (mean +/- SEM): (i) DILT1D: $FOXP3^{+}HELIOS^{+}$ = 71.5% +/- 1.47, $FOXP3^{+}HELIOS^{-}$ = 15.6%
1419 +/- 1.63 and $CD45RA^{-}$ $FOXP3^{-}HELIOS^{-}$ = 4.7% +/- 0.44; (ii) DILfrequency: $FOXP3^{+}HELIOS^{+}$ =
1420 66.9% +/- 2.0, $FOXP3^{+}HELIOS^{-}$ = 19.8% +/- 1.60 and $CD45RA^{-}$ $FOXP3^{-}HELIOS^{-}$ = 8.0% +/- 1.02.
1421 **d-e**, Variation (depicted as the % change from baseline pre-treatment levels) in the frequency of the
1422 $FOXP3^{+}HELIOS^{+}$ Treg, $FOXP3^{+}HELIOS^{-}$ Treg and $CD45RA^{-}$ $FOXP3^{-}HELIOS^{-}$ Teff subsets in
1423 patients treated with a single dose (**d**) or with the 3-day interval dosing schedule. Baseline levels (mean
1424 +/- SEM): (i) DILT1D: $FOXP3^{+}HELIOS^{+}$ = 5.0% +/- 0.54, $FOXP3^{+}HELIOS^{-}$ = 1.2% +/- 0.24 and
1425 $CD45RA^{-}$ $FOXP3^{-}HELIOS^{-}$ = 0.34% +/- 0.06; (ii) DILfrequency: $FOXP3^{+}HELIOS^{+}$ = 4.2% +/- 0.44,
1426 $FOXP3^{+}HELIOS^{-}$ = 1.3% +/- 0.22 and $CD45RA^{-}$ $FOXP3^{-}HELIOS^{-}$ = 0.49% +/- 0.05. (**e**). Data were
1427 generated by intracellular flow cytometry in 6 patients from the DILT1D (treated with doses ranging
1428 from 0.6-1.5 x 10^{6} IU/m^{2}) and 5 patients from the DILfrequency (treated with interval doses ranging
1429 from 0.2-0.32 x 10^{6} IU/m^{2}). IL-2 dosing days are depicted in red in the x axis.

1430

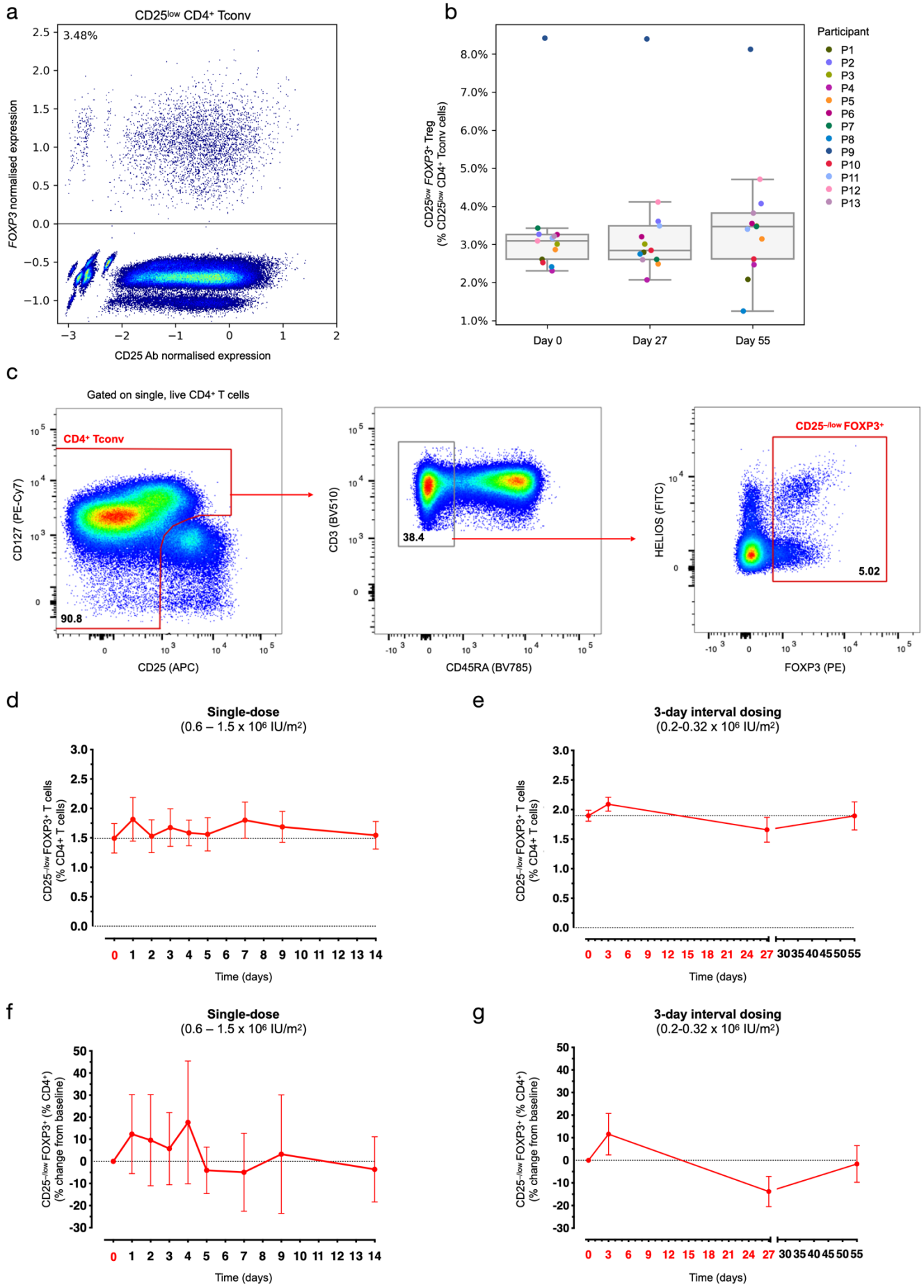
a
CD25low CD4+ Tconv
3.48%
FOXP3 normalised expression
CD25 Ab normalised expression
b
CD25low FOXP3+ Treg
(% CD25low CD4+ Tconv cells)
Day 0
Day 27
Day 55
Participant
P1
P2
P3
P4
P5
P6
P7
P8
P9
P10
P11
P12
P13
c
Gated on single, live CD4+ T cells
CD4+ Tconv
90.8
CD127 (PE-Cy7)
CD25 (APC)
38.4
CD3 (BV510)
CD45RA (BV785)
CD25-/low FOXP3+
5.02
HELIOS (FITC)
FOXP3 (PE)
d
Single-dose
(0.6 – 1.5 x 10⁶ IU/m²)
CD25-/low FOXP3+ T cells
(% CD4+ T cells)
Time (days)
e
3-day interval dosing
(0.2-0.32 x 10⁶ IU/m²)
CD25-/low FOXP3+ T cells
(% CD4+ T cells)
Time (days)
f
Single-dose
(0.6 – 1.5 x 10⁶ IU/m²)
CD25-/low FOXP3+ (% CD4+)
(% change from baseline)
Time (days)
g
3-day interval dosing
(0.2-0.32 x 10⁶ IU/m²)
CD25-/low FOXP3+ (% CD4+)
(% change from baseline)
Time (days)

1432 **Supplementary Figure 11. Interval low-dose IL-2 treatment does not affect the frequency of CD25^{-}**
1433 **$^{/low}$ FOXP3^{+} T cells**

1434 **a**, Identification of FOXP3^{+} within cells sorted from the CD25$^{-/low}$ Tconv gate. FOXP3^{+} cells were
1435 defined as cells with one or more counts of *FOXP3* RNA detected. Data was generated from the analysis
1436 of the 13 DILfrequency donors selected for the single-cell multiomics analysis. **b**, Box and whiskers plot
1437 depicts the frequency of FOXP3^{+} cells within the CD25$^{-/low}$ Tconv gate at Days 0, 27 and 55. Each dot
1438 represents a sample, with colours and shapes representing participants and time points of origin,
1439 respectively. **c**, Gating strategy for the delineation of CD25$^{-/low}$ FOXP3^{+} T cells by flow cytometry. **d-e**
1440 Frequency of CD25$^{-/low}$ FOXP3^{+} T cells in patients treated with a single dose (DILT1D; **d**) or with the
1441 3-day interval dosing schedule (DILfrequency; **e**). **f-g**, Variation (depicted as the % change from baseline
1442 pre-treatment levels) in the frequency of the CD25$^{-/low}$ FOXP3^{+}T cells in patients treated with a single
1443 dose (**f**) or with the 3-day interval dosing schedule (**g**). Data were generated by intracellular flow
1444 cytometry in six patients from the DILT1D (treated with doses ranging from 0.6-1.5 x 10^{6} IU/m^{2}) and
1445 patients from the DILfrequency (treated with interval doses ranging from 0.2-0.32 x 10^{6} IU/m^{2}). IL-2
1446 dosing days are depicted in red in the x axis.

1447

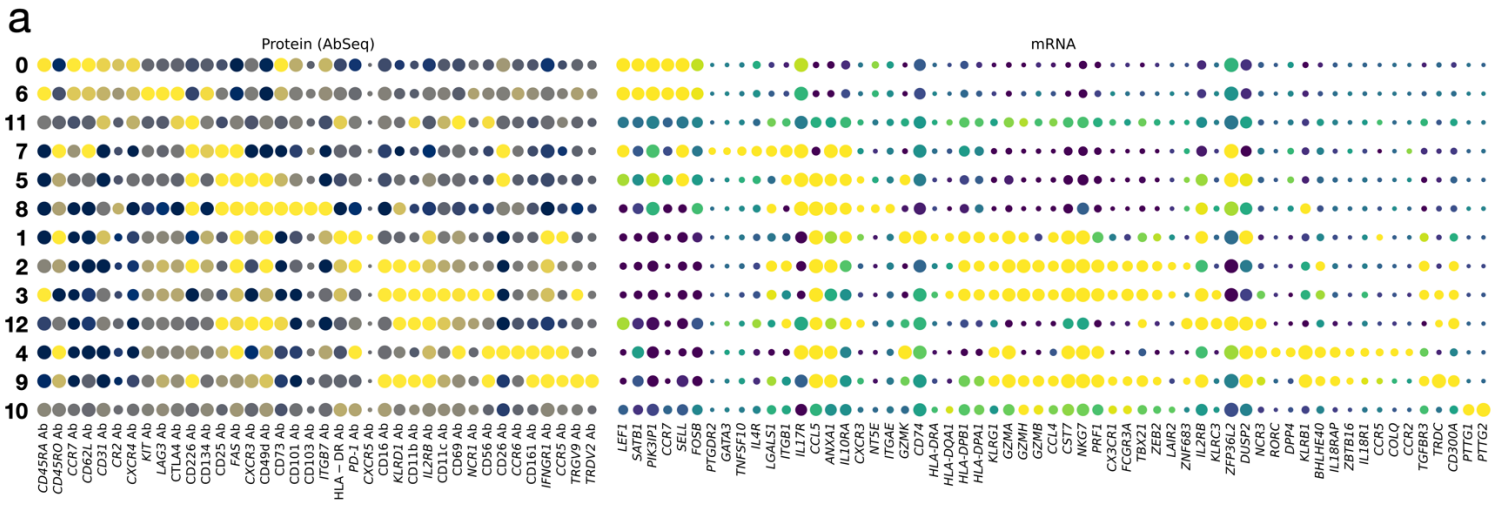
a
Protein (AbSeq)
mRNA
0
6
11
7
5
8
1
2
3
12
4
9
10
CD45RA Ab
CD45RO Ab
CCR7 Ab
CD62L Ab
CD31 Ab
CR2 Ab
CXCR4 Ab
KIT Ab
LAG3 Ab
CTLA4 Ab
CD226 Ab
CD134 Ab
CD25 Ab
FAS Ab
CXCR3 Ab
CD49d Ab
CD73 Ab
CD101 Ab
CD103 Ab
ITGB7 Ab
HLA – DR Ab
PD-1 Ab
CXCR5 Ab
CD16 Ab
KLRD1 Ab
CD11b Ab
IL2RB Ab
CD11c Ab
CD69 Ab
NCR1 Ab
CD56 Ab
CD26 Ab
CCR6 Ab
CD161 Ab
IFNGR1 Ab
CCR5 Ab
TRGV9 Ab
TRDV2 Ab
LEF1
SATB1
PIK3IP1
CCR7
SELL
FOSB
PTGDR2
GATA3
TNFSF10
IL4R
LGALS1
ITGB1
IL17R
CCL5
ANXA1
IL10RA
CXCR3
NT5E
ITGAE
GZMK
CD74
HLA-DRA
HLA-DQA1
HLA-DPB1
HLA-DPA1
KLRG1
GZMA
GZMH
GZMB
CCL4
CST7
NKG7
PRF1
CX3CR1
FCGR3A
TBX21
ZEB2
LAIR2
ZNF683
IL2RB
KLRC3
ZFP36L2
DUSP2
NCR3
RORC
DPP4
KLRB1
BHLHE40
IL18RAP
ZBTB16
IL18R1
CCR5
COLQ
CCR2
TGFBR3
TRDC
CD300A
PTTG1
PTTG2

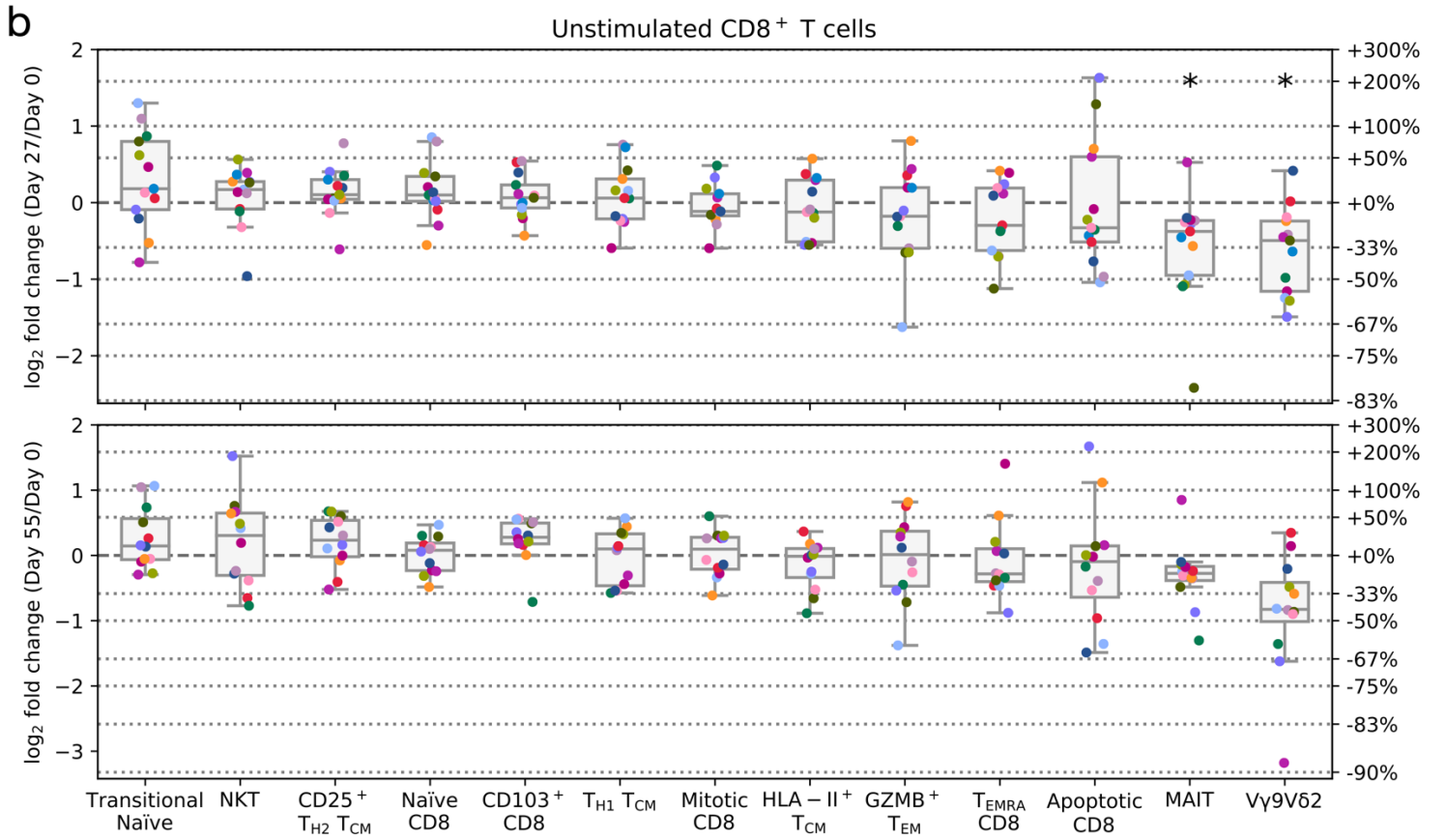
b
Unstimulated CD8+ T cells
log2 fold change (Day 27/Day 0)
log2 fold change (Day 55/Day 0)
+300%
+200%
+100%
+50%
+0%
-33%
-50%
-67%
-75%
-83%
-90%
Transitional Naïve
NKT
CD25+ TH2 TCM
Naïve CD8
CD103+ CD8
TH1 TCM
Mitotic CD8
HLA – II+ TCM
GZMB+ TEM
TEMRA CD8
Apoptotic CD8
MAIT
Vγ9Vδ2

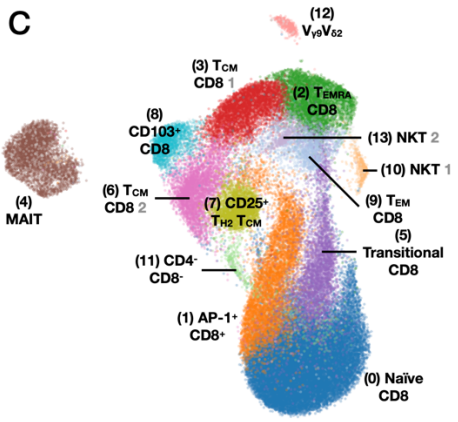
c
(12) Vγ9Vδ2
(3) TCM CD8 1
(2) TEMRA CD8
(8) CD103+ CD8
(13) NKT 2
(10) NKT 1
(4) MAIT
(6) TCM CD8 2
(7) CD25+ TH2 TCM
(9) TEM CD8
(5) Transitional CD8
(11) CD4- CD8-
(1) AP-1+ CD8+
(0) Naïve CD8

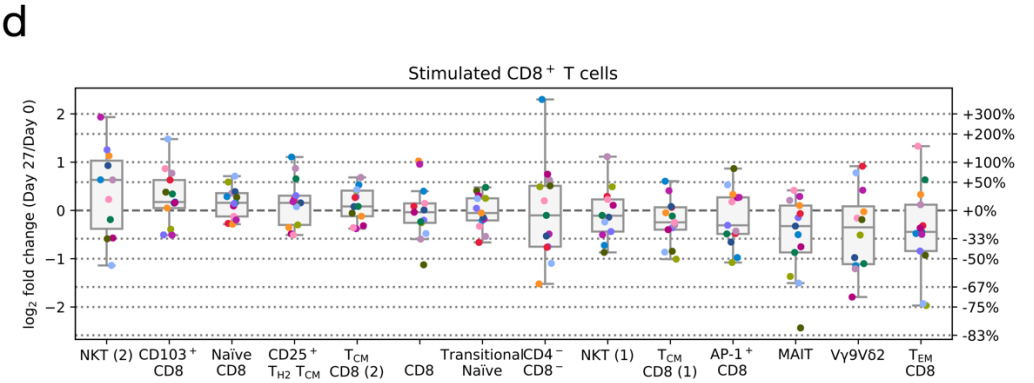
d
Stimulated CD8+ T cells
log2 fold change (Day 27/Day 0)
+300%
+200%
+100%
+50%
+0%
-33%
-50%
-67%
-75%
-83%
NKT (2)
CD103+ CD8
Naïve CD8
CD25+ TH2 TCM
TCM CD8 (2)
CD8
Transitional Naïve
CD4- CD8-
NKT (1)
TCM CD8 (1)
AP-1+ CD8
MAIT
Vγ9Vδ2
TEM CD8

1449

1450 **Supplementary Figure 12. Functional annotation of CD8$^+$ T cells.**

1451 **a**, Expression of selected differentially-expressed markers delineating the functional subsets identified
1452 from the 13 clustering of the 93,621 unstimulated CD8$^+$ T cells profiled in this study. The size of the
1453 dots represents the frequency of the marker in the respective cluster and the colour brightness represents
1454 the relative expression level. Protein markers (AbSeq) are shown on the left section of the plots and
1455 mRNA markers on the right section. **b,** Relative frequency changes of all identified CD8$^+$ T cell clusters
1456 on Day 27 (top panel) or Day 55 (bottom panel) compared to the baseline pre-treatment levels. **c**, UMAP
1457 plot depicting the clustering of *in vitro* stimulated CD8$^+$ T cells. Clusters were manually annotated based
1458 on the expression of key differentially expressed mRNA and protein markers. **d**, Relative frequency
1459 changes of the 14 identified stimulated CD8$^+$ T cell clusters at Day 27 compared to the baseline pre-
1460 treatment (Day 0) levels.

1461

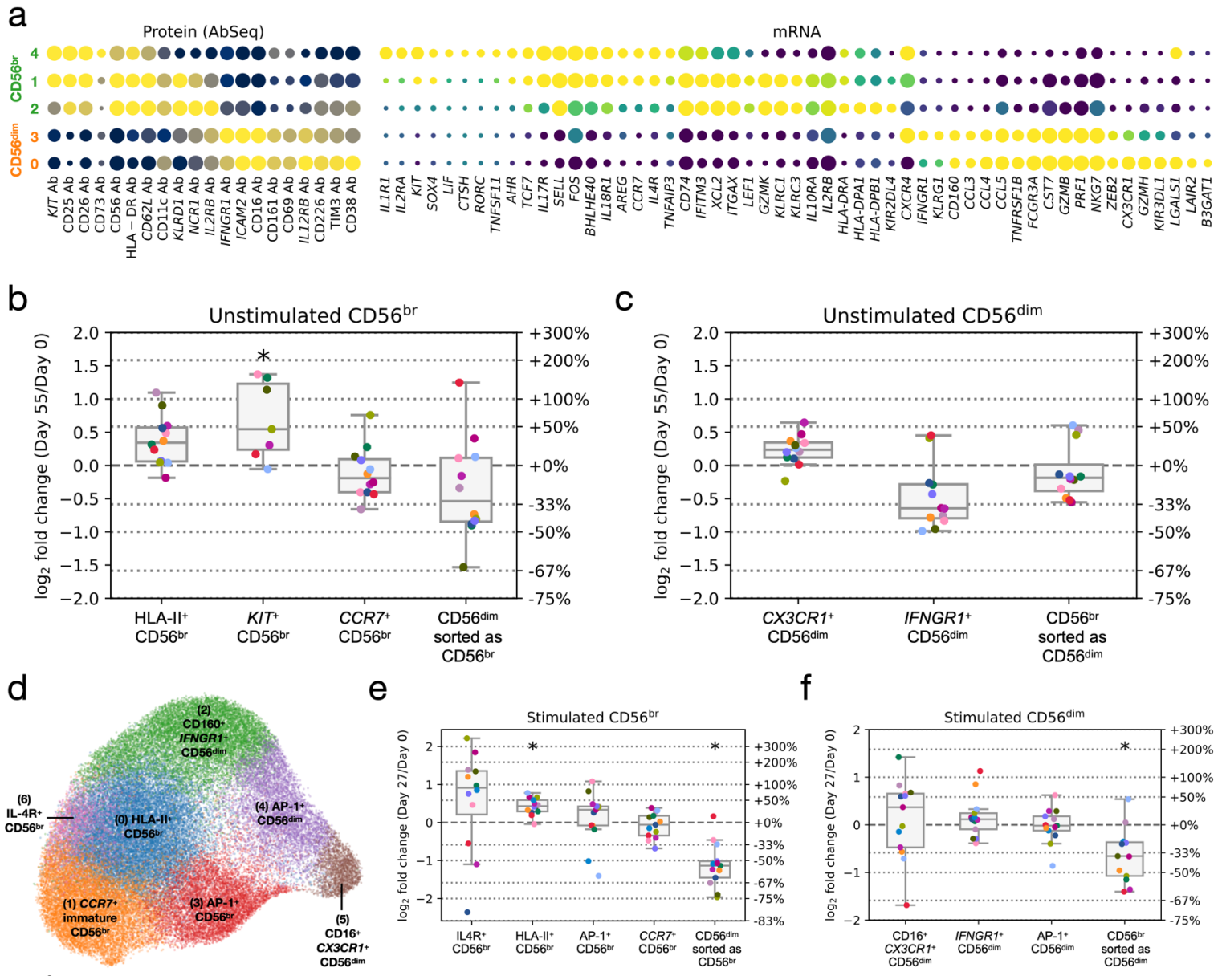

Supplementary Figure 13. Functional annotation of CD56$^+$ NK cells.

a, Expression of selected differentially-expressed markers delineating the five functional subsets identified from the clustering of the 99,169 unstimulated CD56$^+$ NK cells profiled in this study. The size of the dots represents the frequency of the marker in the respective cluster and the colour brightness represents the relative expression level. Protein markers (AbSeq) are shown on the left section of the plots and mRNA markers on the right section. The dotted red line separates the clusters corresponding to either CD56^{br} (top) and CD56^{dim} NK cells (bottom). **b-c**, Relative frequency changes of all identified unstimulated CD56^{br} (**b**) and CD56^{dim} (**c**) NK cell clusters on Day 55 compared to the baseline pre-treatment levels. **d**, UMAP plot depicts the clustering of *in vitro* stimulated CD56$^+$ NK cells. **e-f** Relative

1472 frequency changes of all identified clusters of cells sorted from either the $CD56^{br}$ (**e**) or $CD56^{dim}$ (**f**) NK
1473 cell gates following *in vitro* stimulation on Day 27 compared to the baseline pre-treatment (Day 0) levels.

1474

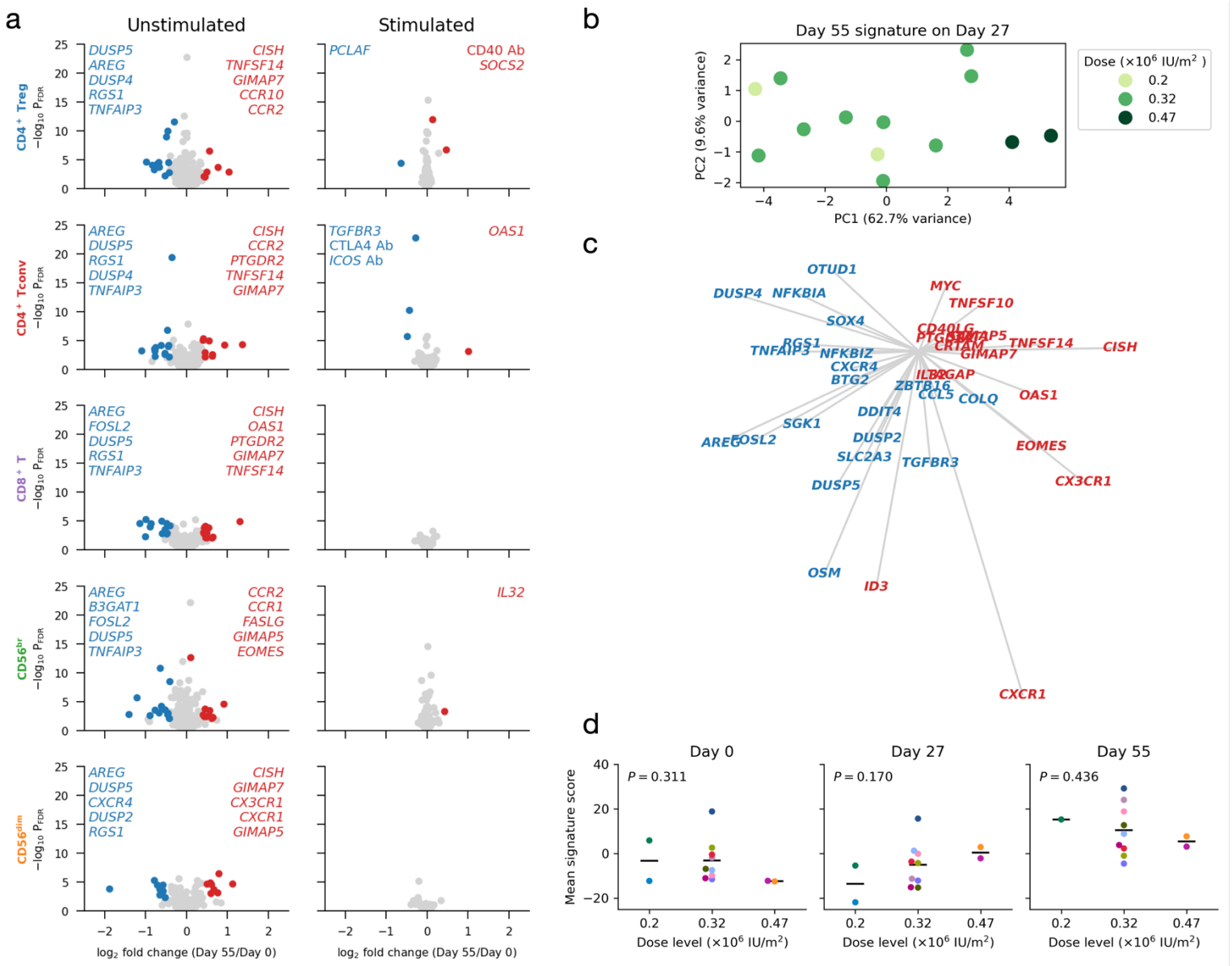

Supplementary Figure 14. Induction of the anti-inflammatory gene expression signature at Day 55 is IL-2 dose-dependent and is detected in all T and NK cell populations

a, Volcano plots depicting gene expression changes between Day 0 and Day 55 for the five assessed immune populations, for unstimulated (left panels) and stimulated (right panels) cells. Significantly differentially expressed genes are coloured in red (upregulated genes) or blue (downregulated genes). The top five up- and downregulated genes (as defined by fold change) are labelled on each panel. **b**, Principal component analysis (PCA) correlating gene expression changes with dose levels. PCA was performed on $\log_2$ fold-change values of Day 55 signature genes on Day 27 in $CD8^+$ T cells. Each dot represents a participant, with colours indicating IL-2 dose levels. Vectors representing the gene loading

1485 scores of PC1 and PC2 are shown on the right panel, with genes up- and downregulated on Day 55
1486 shown in red and blue, respectively. **c**, Day 55 signature scores by participant for each time point. Each
1487 participant is represented by a different colour. **d**, Day 55 signature scores plotted against IL-2 dose. The
1488 average value of the Day 55 signature score in the five cell types is shown for each participant.

1489

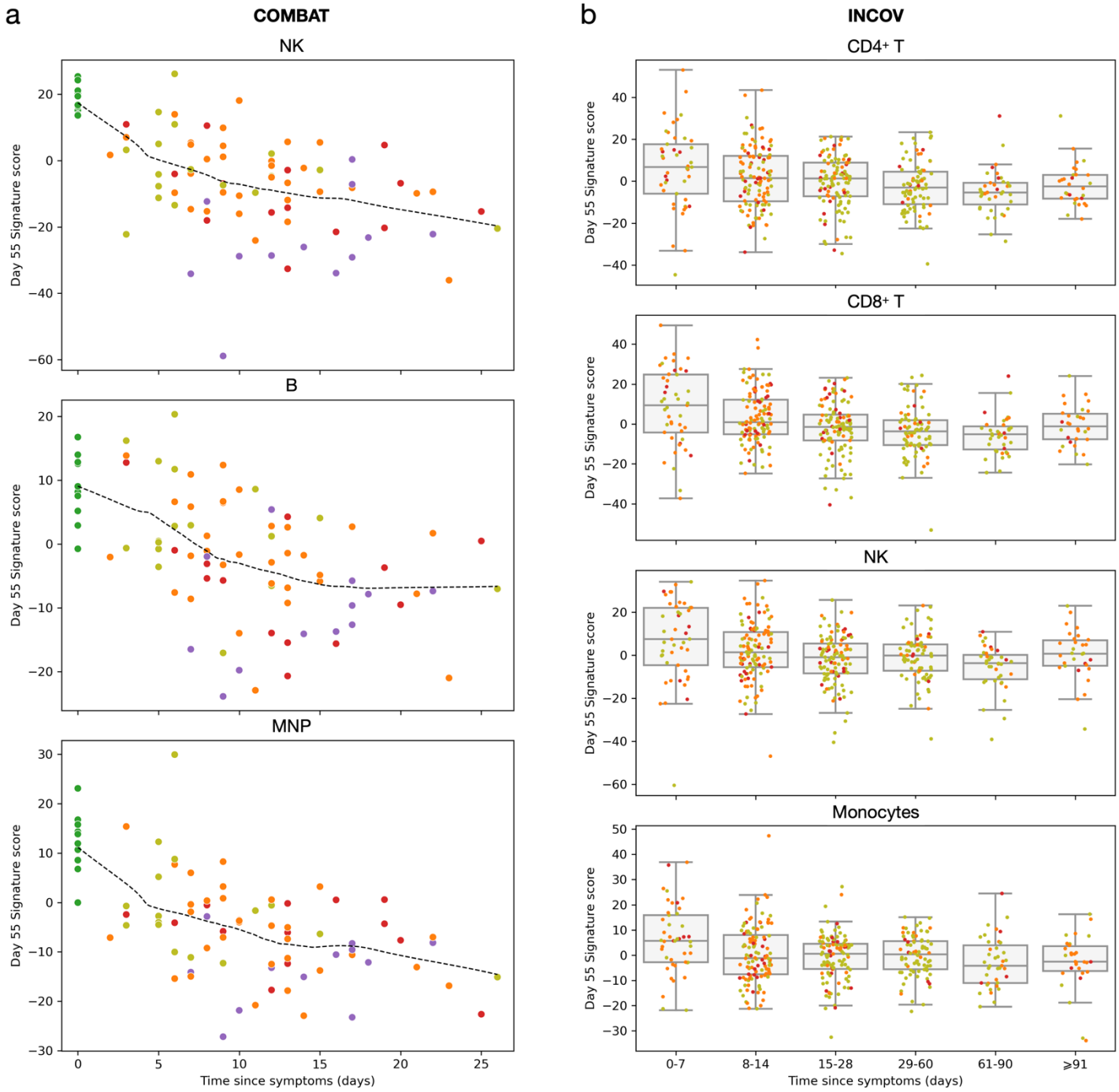

1491

1492 **Supplementary Figure 15. Expression of anti-inflammatory gene expression in COVID-19 patients**

1493 **a**, Day 55 signature scores plotted against the time since COVID-19 symptoms in the COMBAT cohort
1494 in NK cells, B cells and mononuclear phagocytes (MNP). **b**, Day 55 signature scores plotted against the
1495 time since COVID-19 symptoms in the INCOV cohort in $CD4^+$ T cells, $CD8^+$ T cells, NK cells and

1496 monocytes. In **a** and **b**, each dot represents a pseudo-bulk sample from a certain participant and time
1497 point. Up to three longitudinal samples may originate from the same participant. COVID-19 patients
1498 were stratified according to their maximum disease severity. Dashed black lines represent smooth curves
1499 fitted by locally weighted scatterplot smoothing (LOWESS).
1500

Supplementary Information

Supplementary Table 1. Baseline characteristics of study participants

Supplementary Table 2. Targeted mRNA, protein (AbSeq) and immunostaining panels used in this study

Supplementary Table 3. Characteristics of COMBAT study participants with single-cell data available

Supplementary Data 1. Summary of the cluster-specific RNA and AbSeq markers used for cell type annotation

Supplementary Data 2. Differential expression between Day 0 and Day 27 or Day 55 analysed using DESeq2